Current Trends in Deep Learning for Earth Observation: An Open-source Benchmark Arena for Image Classification

Ivica Dimitrovski[a,b], Ivan Kitanovski[a,b], Dragi Kocev[a,c], Nikola Simidjievski[a,c,d]

[a]*Bias Variance Labs, d.o.o., Ljubljana, Slovenia*
[b]*Faculty of Computer Science and Engineering, University Ss Cyril and Methodius, Skopje, N. Macedonia*
[c]*Department of Knowledge Technologies, Jožef Stefan Institute, Ljubljana, Slovenia*
[d]*Department of Computer Science and Technology, University of Cambridge, Cambridge,United Kingdom*
Correspondence to: [ivica,ivan,dragi,nikola]@bvlabs.ai

Abstract

We present *AiTLAS: Benchmark Arena* – an open-source benchmark framework for evaluating state-of-the-art deep learning approaches for image classification in Earth Observation (EO). To this end, we present a comprehensive comparative analysis of more than 400 models derived from nine different state-of-the-art architectures, and compare them to a variety of multi-class and multi-label classification tasks from 22 datasets with different sizes and properties. In addition to models trained entirely on these datasets, we also benchmark models trained in the context of transfer learning, leveraging pre-trained model variants, as it is typically performed in practice. All presented approaches are general and can be easily extended to many other remote sensing image classification tasks not considered in this study. To ensure reproducibility and facilitate better usability and further developments, *all of the experimental resources* including the trained models, model configurations and processing details of the datasets (with their corresponding splits used for training and evaluating the models) are *publicly available on the repository*: https://github.com/biasvariancelabs/aitlas-arena.

1 Introduction

Recent trends in machine learning (ML) have ushered in a new era of image-data analyses, repeatedly achieving great performance across a variety of computer-vision tasks in different domains [1, 2]. Deep learning (DL) approaches have been at the forefront of these efforts – leveraging novel, modular and scalable deep neural network (DNN) architectures able to process large amounts of data. The inherent capabilities of these approaches also extend to various areas of remote sensing, in particular Earth Observation (EO), employed for analyzing different types of large-scale satellite data [3]. Many of these contributions are instances of image-scene classification, such as land-use and/or land-cover (LULC) identification tasks, focusing on image-scene analyses, characterizations, and classifications of changes in the landscape, caused either by human activities or by the elements.

Historically, from the perspective of ML, many of these tasks have been addressed mostly through the paradigms of either pixel-level [4, 5] or object-level classification tasks [6]. The former refers to classification tasks focusing on each pixel in the image, associating it with the appropriate semantic label. Such approaches typically do not scale well on high-resolution images, but more importantly, many times struggle to capture more high-level patterns in the image that can span over many pixels [7]. The latter, object-level classification methods, focus on analyzing distinguishable and meaningful objects in the image (as a collection of pixels) rather than independent pixels. This, in general, allows for better scalability and performance, however, such approaches may struggle with images containing more diverse, and hardly-distinguishable objects, which prevail in most high-resolution remote-sensing data. Methods based on both pixel-level and object-level paradigms have shown decent performance and are still actively researched, mostly as instances of image segmentation and object detection tasks, respectively. More recently, however, methods based on a new paradigm of scene-level classification [8, 9] have shown significant performance improvements, focusing on learning semantically meaningful representations of more sophisticated patterns in an image by leveraging the capabilities of deep learning.

In this context, DL approaches have been successfully applied in various scenarios, by learning models from scratch or via transfer learning[10, 11], in a fully supervised or self-supervised setting [12, 13], exploiting the heterogeneity [14] and temporal properties [15] of the available data. As a result, this synergy of accurate DL approaches, on the one hand, and accessible high-resolution aerial/satellite imagery, on the other, has led to important contributions in various domains ranging from agriculture [16, 17, 18], ecology [19, 20], geology [21] and meteorology [22, 23, 11] to urban mapping/planning[24, 25, 26] and archaeology [27].

Nevertheless, most of these efforts typically focus on very narrow tasks, stemming from domain-specific and/or spatially-constrained datasets. As a result, models have been evaluated in different settings and under different conditions [28] – hardly reproducible and comparable. These persistent challenges, akin to a lack of standardized and consistent validation and evaluation of novel approaches, have also been identified by the community [29]. Citing the lack of available documentation on the design and evaluation of the employed machine learning approaches, the community highlights the urgent need for standardized benchmarks, that will not only enable proper and fair model-comparison across datasets and similar tasks, but will also facilitate faster progress in designing better and more accurate modeling approaches.

Motivated by this, in this work, we introduce *AiTLAS: Benchmark Arena* – an *open-source EO benchmark framework* for evaluating state-of-the-art DL approaches for EO image classification. To this end, we present extensive comparative analyzes of models derived from nine different state-of-the-art architectures, comparing them on a variety of multi-class and multi-label classification tasks from 22 datasets with different sizes and properties. We benchmark models trained from scratch as well as in the context of transfer learning, leveraging pre-trained model variants as it is typically performed in practice. While in this work we mostly focus on EO-image classification tasks, such as LULC, all of the presented approaches are general and easily extendable to other remote-sensing image classification tasks. More importantly, to ensure reproducibility, facilitate better usability and further exploitation of the results from our work, we provide *all of the experimental resources* - freely available on our repository[1]. The repository includes the complete study details, such as the trained models, model parameters, train/evaluation configurations, measured performance scores, as well as the details on all of the datasets and their prepossessed versions (with the appropriate train/validation/test splits) used for training and evaluating the models.

To our knowledge, we present a unique systematic review and evaluation of different state-of-the-art DL methods in the context of EO image classification across many classification problems – benchmarked in the same conditions and using the same hardware. Related efforts, while relevant, have mostly focused on evaluating approaches on particular datasets [8, 28, 30, 31]; evaluating different aspects of method-design [32, 14] relevant to remote-sensing classification tasks; or providing a more general overview of the common tasks at hand [33, 34]. In particular, Cheng et al. [8] introduce a dataset and surveys several ML representation-learning approaches, commonly used for remote-sensing classification tasks, comparing their performance when combined with traditional convolutional neural network (CNN) architectures. Xia et al. [31] also introduce a benchmark dataset for aerial-image classification, providing a comparison similar to [8] of representation-learning approaches combined with three deep networks. Another, more recent, study [28], discuses and compares more recent DL approaches and surveys several applications on three different datasets. In particular, the authors showcase the performance of the different methods for each dataset, as reported in the respective papers. The underlying, persistent, conclusions from these studies show that model performances are associated with a respective dataset and study design, presenting difficulties for fair and general model comparisons. This is expected, but in our work, we seek to remedy this issue, by training and evaluating all models under the same conditions.

In this context, our work is related to the one of Zhai et al. [32], which present a large-scale study on more recent representation-learning approaches, benchmarking different aspects of method design and model parameters. However, Zhai et al. [32] consider a rather wide scope of different datasets with only a few relevant to remote-sensing and LULC classification, thereof. Neumann et al. [14] present a large-scale study on five different benchmark datasets, however, they aim at investigating the effect of transfer learning on these tasks. More specifically, they evaluate different variants of the same model architecture, trained under different circumstances, rather than comparing different model architectures. Another related study by Stewart et al. [35] reports on comparison of different variants of ResNets on EO-image classification tasks from four datasets. More recently, and arguably most related to our work in

[1] https://github.com/biasvariancelabs/aitlas-arena

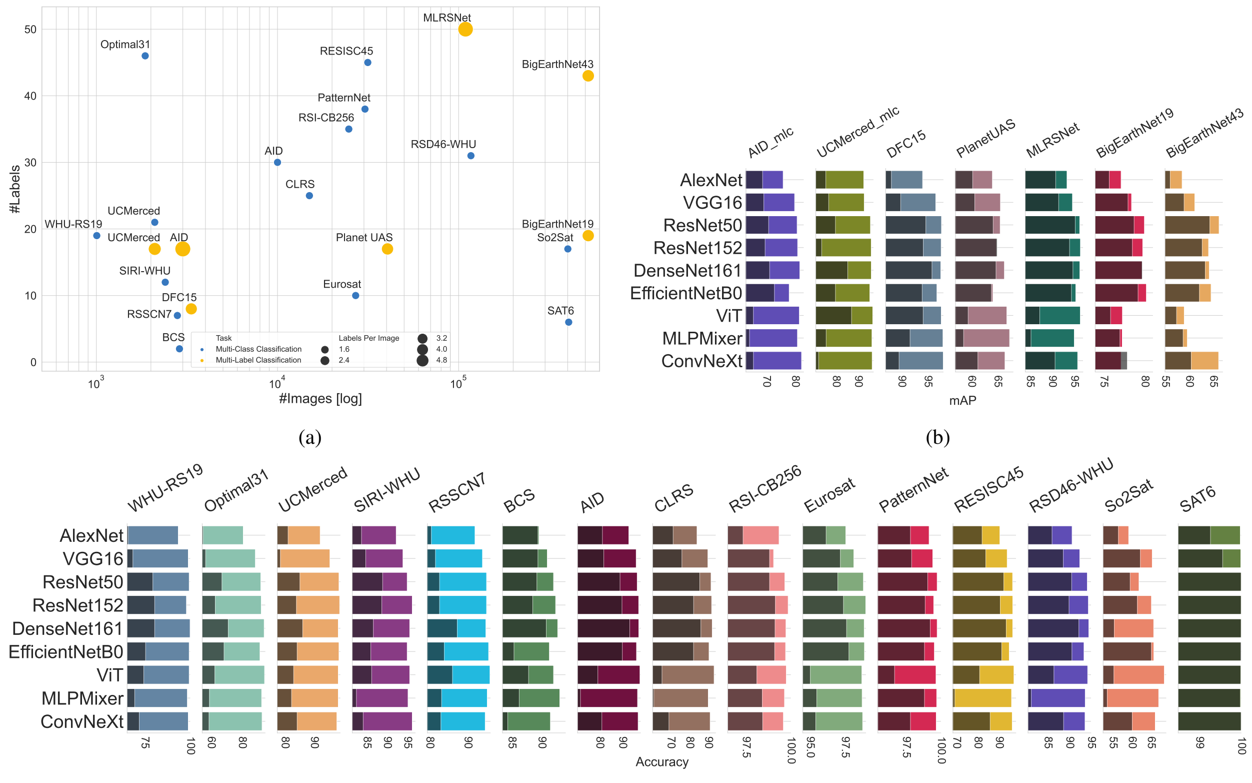

(a)

(b)

(c)

Figure 1: **Overview of the study**: We benchmarked more than 400 models from 9 different model architectures on tasks from **(a)** 22 datasets with different sizes and properties; comparing them on **(b)** multi-label and **(c)** multi-class classification tasks. We evaluate two versions of each model architecture: (i) trained from scratch (denoted with *darker shading*) and (ii) pre-trained on ImageNet-1K (denoted with *lighter shading*). Note the varying scales in (b) and (c), made purposely for better visibility. Detailed results are presented in Section 4 and Appendix C

terms of the number of evaluated models, Papoutsis et al. [30] present an extensive empirical evaluation of different state-of-the-art DL architectures suitable for EO-image classification tasks, specifically LULC tasks, focusing exclusively on the BigEarthNet [36] dataset. Namely, the authors benchmark different classes of model architectures across different criteria and introduce an efficient and well-performing model, specifically tailored for BigEarthNet.

In this work, we go beyond all the aforementioned studies, largely extending the scope under study in two directions: the number of model architectures (and model variants) being evaluated and datasets being considered. This results in evaluating more than 400 different models with varying architectures, designs, and learning paradigms across 22 datasets. We also provide essential study-design principles and model training details that will aid in more systematic and rigorous experiments in future work. The proposed *AiTLAS: Benchmark Arena* builds on the AiTLAS toolbox [37][2] – a recent open-source library for exploratory and predictive analysis of satellite imaginary pertaining to different remote-sensing tasks. AiTLAS implements a variety of methods and libraries for data handling, processing, and analysis, with PyTorch [38] as a backbone for constructing and learning DL models. By having all of the methods and datasets under the same umbrella, we provide the means for a fair, unbiased, and reproducible comparison of approaches across different criteria that include: overall model performance, data- and task-dependent model performance, model size, and learning efficiency as well as the effect of transfer learning via model pre-training.

The results, summarized in Figure 1, show that many of the current state-of-the-art architectures for vision tasks can lead to decent predictive performance when applied to EO image classification tasks. While training models from

[2] https://aitlas.bvlabs.ai

scratch, leads to satisfactory performance in some cases, fine-tuning pre-trained models on each dataset leads to the best performance. We observed this in (almost) all cases, regardless of dataset properties, type of the classification tasks, or the model architecture. We found more considerable performance gains on tasks from smaller datasets, which, as expected, benefited more from the pre-training process than models trained on larger datasets. In terms of model architectures, our experiments showed that the Vision Transformer [39] and DenseNet [40] models, were generally able to achieve the best performance, with the latter requiring twice the training time. Throughout the paper, we further evidence and discuss these findings.

In summary, we make several contributions in this paper. In particular, we:

- We introduce AiTLAS:Benchmark Arena, an open-source benchmark framework that allows standardized evaluation of machine learning models for Earth Observation (EO) applications;
- We provide study-design principles for training and evaluating state-of-the-art deep learning models on various supervised EO image classification tasks from 22 datasets with different size and properties;
- We implement and benchmark more than 400 models stemming from 9 state-of-the-art architectures, including models trained from scratch as well as their pre-trained variants;
- We provide an open-source access to all of the experimental details, including trained models, dataset details, train/evaluation configurations and detailed performance scores.

2 Data & models

2.1 Data description

With the ever-growing availability of remote sensing data, there has been a significant effort by many research groups into preparing, labeling, and providing proper datasets that will support the development and evaluation of sophisticated machine learning methods. While there are many such datasets, both proprietary and publicly available, in this work we focus on the latter. We select 22 such datasets, with varying sizes (number of images), varying image types, image sizes, and formats, and more importantly, related to different classification tasks.

Namely, we consider datasets related to both multi-class and multi-label classification tasks, mainly addressing LULC applications. The objective of *multi-class classification* tasks is to predict one (and only one) class (label) from a set of predefined classes for each image in a dataset. *Multi-label classification*, on the other hand, refers to predicting multiple labels from a predefined set of labels for each image in the dataset [41] (eg. an image can belong to more than one class simultaneously). In our experimental study, we consider 15 multi-class and 7 multi-label datasets.

Tables 1 and 2 summarize the properties of the considered multi-class (MCC) and multi-label (MLC) classification datasets, respectively. The number of images across datasets is quite diverse, ranging from datasets with $\sim 2K$ images to datasets with $\sim 500K$ images. This also extends towards the number of labels per images, ranging from 2 to 60. Figure 1a visualizes the datasets with respect to their size-properties, with x-axis denoting the number of images (on a log-scale) and y-axis denoting the number of labels (with marker-size denoting the number of labels per image) for each of the different datasets. Most of the datasets are comprised of Aerial RGB images (with only few comprised of satellite multi-spectral data) that are different in the spatial resolution, size and format. Finally, we note the datasets that include predefined splits (for training, validation and testing) given by the original authors, and provide the splits for the ones that are missing as further discussed in Section 3.1. More detailed description of each dataset are given in Appendix C.

2.2 Model architectures

Current trends in EO image classification leverage the capabilities of DL architectures for computer vision, learning data representations that very often lead to superior predictive performance. We recognize that there are many different approaches, stemming from different model architectures and model variants. These can differ in various ’finer’ details (e.g., number and width of layers, hyper-parameter values, and learning regimes), often developed for a particular task at hand. Rather than seeking a state-of-the-art performance for each individual EO problem/dataset, in

Table 1: Multi-class classification (MCC) datasets.

Name	Image type	#Images	Image size	Spatial resolution	#Labels	Predefined splits	Image format
UC Merced [9]	Aerial RGB	2100	256×256	0.3m	21	No	tif
WHU-RS19 [42]	Aerial RGB	1005	600×600	0.5m	19	No	jpg
AID [31]	Aerial RGB	10000	600×600	0.5m - 8m	30	No	jpg
Eurosat [43]	Sat. Multispectral	27000	64×64	10m	10	No	jpg/tif
PatternNet [44]	Aerial RGB	30400	256×256	0.06m - 4.69m	38	No	jpg
Resisc45 [45]	Aerial RGB	31500	256×256	0.2m - 30m	45	No	jpg
RSI-CB256 [46]	Aerial RGB	24747	256×256	0.3 - 3m	35	No	tif
RSSCN7 [47]	Aerial RGB	2800	400×400	n/a	7	No	jpg
SAT6 [48]	RGB + NIR	405000	28×28	1m	6	Yes	mat
Siri-Whu [49]	Aerial RGB	2400	200×200	2m	12	No	tif
CLRS [50]	Aerial RGB	15000	256×256	0.26m - 8.85m	25	No	tif
RSD46-WHU [51]	Aerial RGB	116893	256×256	0.5m - 2m	46	Yes	jpg
Optimal 31 [52]	Aerial RGB	1860	256×256	n/a	31	No	jpg
Brazilian Coffee Scenes (BSC) [53]	Aerial RGB	2876	64×64	10m	2	No	jpg
SO2Sat [54]	Sat. Multispectral	400673	32×32	10m	17	Yes	h5

Table 2: Multi-label classification (MLC) datasets.

Name	Image type	#Images	Image size	Spatial resolution	#Labels	#Labels per image	Predefined splits	Image format
UC Merced (MLC) [55]	Aerial RGB	2100	256×256	0.3m	17	3.3	No	tif
MLRSNet [56]	Aerial RGB	109161	256×256	0.1m - 10m	60	5.0	No	jpg
DFC15 [57]	Aerial RGB	3342	600×600	0.05m	8	2.8	Yes	png
BigEarthNet 19 [36]	Sat. Multispectral	519284	20×20 60x60 120x120	60m 20m 10m	19	2.9	Yes	tif, json
BigEarthNet 43 [58]	Sat. Multispectral	519284	20×20 60x60 120x120	60m 20m 10m	43	3.0	Yes	tif, json
AID (MLC)[59]	Aerial RGB	3000	600×600	0.5m - 8m	17	5.2	Yes	jpg
PlanetUAS [60]	Aerial RGB	40479	256×256	3m	17	2.9	No	jpg/tiff

this study, we are interested in providing a more general evaluation framework, and benchmarking models by analyzing their characteristics and unique properties through the lens of their predictive performance and learning efficiency across all datasets.

Therefore, our model-architecture (and parameter) choices are motivated by different architecture ’classes’, such as the traditional convolutional architectures as well as the more recent attentional and mlp-based architectures. This also renders models with different sizes, training/inference time, different abilities in a transfer-learning setting, etc. More specifically, we investigate several architectures which have been traditionally used for EO image classification tasks such as: AlexNet [61], VGG16 [62], ResNet [63] and DenseNet [40]. Moreover, we investigate more recent architectures which include EfficientNet [64], ConvNeXt [65], Vision Transformer [39] and MLPMixer [66], that have shown state-of-the-art performance in various vision tasks. In the following, we provide a brief overview of these architectures, highlighting their properties in Table 3.

Table 3: Summary of the representative model architectures considered in this study.

Model	Year	#Layers	#Parameters	Based on
AlexNet [61]	2012	8	$\sim$ 57.0M	[67]
VGG16 [62]	2014	16	$\sim$ 134.2M	[67]
ResNet50 [63]	2015	50	$\sim$ 23.5M	[67]
ResNet152 [63]	2015	152	$\sim$ 58.1M	[67]
DenseNet161 [40]	2017	161	$\sim$ 26.4M	[67]
EfficientNet B0 [64]	2019	237	$\sim$ 5.2M	[67] version: B0
Vision Transformer (ViT) [39]	2020	12	$\sim$ 86.5M	[68] version: b_16_224
MLPMixer [66]	2021	12	$\sim$ 59.8M	[68] version: b_16_224
ConvNeXt [65]	2022	174	$\sim$ 28M	[67] version: tiny

The first class of models we consider, rely on convolutional architectures, which, in recent years, have driven many of the advances in computer vision. The architecture of convolutional neural networks (CNN) consists of many (hidden) layers stacked together, designed to process (image) data in the form of multiple arrays. Most typically, CNNs consist of a series of convolutional layers, which apply convolution operation (passing the data through a kernel/filter), forwarding the output to the next layer. This serves as a mechanism for constructing feature maps, with former layers typically learning low-level features (such as edges and contours), subsequently increasing the complexity of the learned features with deeper layers in the network. Convolutional layers are typically followed by pooling operations, which serve as a downsampling mechanism, by aggregating the feature maps through local non-linear operations. In turn, these feature maps are fed to fully-connected layers, which perform the ML task at hand – in this case classification. All the layers in a network employ an activation function. In practice, the intermediate, hidden, layers employ a non-linear function such as rectified linear unit (ReLU) or Gaussian Error Linear Unit (GELU) as common choices. The choice of activation function in the final layer relates to the tasks at hand, typically a sigmoid function in the case of classification. CNN architectures can also include different normalization and/or dropout operators embedded among the different layers, which can further improve the performance of the network.

CNN architectures have been widely researched, with models applied in many contexts of remote sensing, and in particular EO image classification [11, 69, 70, 30]. This includes *AlexNet* [61], a pioneering architecture that introduced and successfully demonstrated the utility of the aforementioned blueprint of CNNs for computer vision tasks. Namely, even though the architecture of AlexNet has a modest depth (relative to more recent architectures) consisting of eight layers, it remains an efficient baseline approach for a variety of EO tasks [8, 10], leading to decent performance, especially when pre-trained with large image datasets [71]. We also consider the more sophisticated *VGG* [62], which employs a deeper architecture inspired by AlexNet. VGG has shown great performance in a variety of vision tasks, including EO-image classification problems [72, 73, 44]. There are two variants of VGG in practice, VGG16 and VGG19; both of which extend AlexNet mainly by increasing the depth of the network with 13 and 16 convolutional layers, respectively. In this study, we evaluate the performance of the former *VGG16*. VGGs employ kernels with smaller sizes than the ones typically used in AlexNet, demonstrating that stacking multiple smaller kernels are able better to extract more complex representations, than one larger filter. While, in general, increasing the network depth by adding convolutional layers helps for learning more complex and more informative representations, thereof, in practice this can lead to several issues such as the vanishing gradient problem [74], which impairs the network training.

The Residual neural networks (*ResNets*) [63, 75] tackle this issue explicitly, by employing skip connections between blocks, therefore enabling better backprop gradient flow; better training, and, in general, better predictive performance. ResNet architecture follows a typically CNN blueprint: Stacking residual blocks (typically same-size CNN layers) and convolutional blocks (typically introducing a bottleneck via different-size CNN layers) together, followed by fully-connected layers. By employing skip connections, the ResNet architecture allows stacking multiple layers in a block, therefore training models with much deeper architectures. Here we investigate two such variants with varying depths, *ResNet50* and *ResNet152*, with 50 and 152 layers, respectively. Since their inception, ResNets have been a very popular choice in practice. This also extends towards their utility for EO tasks, applied in the context of image classification and semantic segmentation [76, 77, 35, 30]. Dense Convolutional Networks (*DenseNets*) [40] are another well-performing architecture variant of ResNets, that has demonstrated state-of-the-art results on many classification tasks, including applications in the domain of remote sensing [78, 79, 80]. As the name suggests, DenseNets consist of dense blocks, where each layer is connected to every preceding layer, taking an additional (channel-wise) concatenated input of the feature maps learned in the former layers. This is different from the ResNets, which propagate (element-wise) aggregated feature maps through the network layers. The architecture of DenseNets encourages feature reuse throughout the network, leading to well-performing and more compact models (with fewer trainable parameters than a ResNet of equivalent size), albeit at the cost of increased memory during training.

EfficientNets [64] are a recent class of lightweight architecture that alleviate such common computational difficulties, typical when scaling deep architectures on larger and/or harder problems. Namely, rather than scaling the architecture in one aspect of increasing the depth (number of layers) [63], width (number of channels) [75] or (input image) resolution [81]; EfficientNets implement compound scaling, that uniformly scales the architecture along the three dimensions simultaneously. Compound scaling seeks an optimal balance between these 3 dimensions given the available resources and task at hand. In turn, such an approach leads to substantially smaller models (than CNN variants of equivalent performance), while retaining state-of-the-art predictive performance. In the context of EO tasks, (variants of) EfficentNets have been successfully applied in different settings [82, 83, 84, 80], and have also been thoroughly investigated in the context of multi-label image classification tasks from BigEartNet [30]. While there are eight variants of EfficientNets, differing in the size and complexity of the architectures, here we investigate the performance of the baseline *EfficientB0* architecture with 5.2M parameters, substantially lower than any of the other competing model architectures. Most recently, [65] introduce *ConvNeXt*, a novel class of convolutional architectures, that leverage various successful design decisions of many preceding architectures with a proven track record on vision tasks. Namely, ConvNeXt implement various techniques at different levels: from reconfiguring details like activation functions and normalization layers; redesigning more general architecture details that relate to residual and convolutional blocks; to modifications in the training strategies. This, in turn, leads to models with state-of-the-art performance, not only better than popular models from the same class of convolutional architectures but also better than the more recent attentional architectures, discussed next. While there are several variants of the ConvNeXt architecture that differ in their size, in this study we evaluate the performance of the smallest variant, namely *ConvNeXt_tiny*. Note that, to our knowledge, this is the first application of ConvNeXt on EO-image classification tasks.

We next take the notion of the recent success of the class of attentional network architectures and study the performance of *Vision Transformers* (ViT) [39] in the context of EO-image classification tasks. Namely, ViTs inspire by the popular NLP (natural language processing) Transformer architecture [85], leveraging an attention mechanism for vision tasks. Much like the original Transformer that seeks to learn implicit relationships in sequences of word-tokens via multi-head self-attention, ViTs focus on learning such relationships between image patches. Typically they employ a standard transformer encoder that takes a lower-dimensional (linear) representation of these image patches together with additional positional embedding from each, in turn, feeding the encoder output to a standard MLP head. ViTs have shown great performance on a variety of vision tasks, particularly when combined with pre-training from large datasets. This also includes several applications in remote sensing [86, 30, 87].

An attention mechanism, in the context of vision tasks, can be achieved differently (e.g., attending over channels and/or spatial information, etc.) and even employed with typically convolutional architectures[88, 89, 84]. One such alternative, that builds only on the classical MLP architecture, is the *MLPMixer* [66]. Namely, similar to a ViT, an MLPMixer operates on image patches; and contains two main components: A block of MLP layers for 'mixing' the spatial, patch-level, information on every channel; and a block of MLP layers for 'mixing' the channel-information of an image. This renders lightweight models, with performance on par with many much more sophisticated architectures, on a variety of vision problems, both more general as well as EO tasks [90, 30, 87]. We employ an MLPMixer with an input size of 224x224 and a patch resolution of 16×16 pixels.

From each of the nine highlighted architectures, we evaluate two model versions: trained entirely on a given dataset and fine-tuned models that have been pre-trained on a different image dataset. This results in comparing 18 models on each predictive task, which are available on our repository.

3 Experimental design

3.1 Training and evaluation protocol

To establish a unified evaluation framework and to support the reproducibility of the results, we generated train, validation, and test splits using 60%, 20%, and 20% fractions, respectively. All of the data splits were obtained using stratified sampling. This technique ensures that the distribution of the target variable(s) among the different splits remains the same [91]. We performed such stratification for all datasets, except the ones which include predefined splits provided by the original authors. More specifically, for the *BigEarthNet* and *SO2Sat* datasets, we use the train, validation and test splits as provided in [58, 36, 54]. Since *SAT6*, *RSD46-WHU*, *DFC15* and *AID* datasets consist only with predefined train and test splits, we further take 20% from the train part for validation. Finally, note that the PlanetUAS dataset was part of a competition, and as such, the test data is not publicly available. Therefore, from the original train data, we generated train, validation, and test splits using the 60%, 20%, and 20% fractions, respectively.

All the models are trained using the train splits, with parameters selection/search performed using the validation splits. Additionally, to overcome over-fitting, we perform early stopping on the validation split for each dataset, the best checkpoint/model found (with the lowest validation loss) is saved and then applied on the original test split to obtain the final assessment of the predictive performance. All the train/validation/test splits for each dataset are available in our repository.

Note that, during training we perform *data augmentation* for each dataset, by first resizing all the images to 256x256, followed by selecting a random crop of size 224x224. We then perform random horizontal and/or vertical flips. During evaluation/testing, we first resize the images to 256×256, followed by a central crop of size 224×224. We believe that this, in general, helps our models to generalize better on a given dataset. Also note that, in the study we are using only RGB images. In the case of the multispectral datasets (*Eurosat*, *SO2Sat* and *BigEarthNet*) we computed the images in the RGB color space by combining the red (B04), green (B03) and blue (B02) bands. For the *Brazilian Coffee Scenes* dataset we use images in green, red and near-infrared spectral bands, since these are most useful and representative for distinguishing vegetation areas as suggested by the authors.

Since we train models on 22 datasets, with a different number of classes, different training samples, and class-distributions (as shown in Tables 1 and 2), we perform a hyperparameters search for each model and each dataset, to account for these variations. Namely, we search over different values of learning rate: 0.01, 0.001, and 0.0001. We use *ReduceLROnPlateau* as a learning scheduler which reduces the learning rate when the loss has stopped improving. Models often benefit from reducing the learning rate by a factor once learning stagnates. This scheduler tracks the values of the loss measure, reducing the learning rate by a given factor when there is no improvement for a certain number of epochs (denoted as 'patience'). In our experiments, we track the value of the validation loss, with patience set to 5 and a reduction factor set to 0.1 (the new learning rate will be $lr * factor$). Additionally, we also apply early stop criteria if no improvements in the validation loss are observed over 10 epochs. Finally, we use fixed values for some of the hyperparameters such as batch size which was set to 128. For optimization, we use *RAdam optimizer* [92] without weight decay. RAdam is a variant of the standard Adam [93], which employs a mechanism that rectifies the variance from the adaptive learning rate. This, in turn, allows for an automated warm-up, tailored to the particular dataset at hand.

For each model architecture, we train two variants: (i) models trained entirely on a given dataset and (2) fine-tuned models previously trained on a different (and larger) image dataset. The former, which we refer to as models "trained from scratch", refer to models trained only on the dataset at hand and initialized with random weights in the training procedure. The latter leverages transfer learning via model pre-training. In the next section, we provide further details on how we use and fine-tune these pre-trained models. All models were trained on NVIDIA A100-PCIe GPUs with 40 GB of memory running CUDA version 11.5. We used the AiTLAS toolbox [3] to configure and run the experiments. All configuration files for each experiment are also available in our repository along with the trained models. We believe this provides a standardized evaluation framework for EO image classification tasks.

3.2 Transfer learning strategy

In this study, we take the notion of *transfer learning* as a strategy that can lead to performance improvements of vision models on image classification tasks [32], in particular in EO domains [94]. In our problem setting, transfer learning allows downstream, task-specific, models to leverage learned representations from model architectures that have been pre-trained on much larger image datasets. This, in turn, often leads to (fine-tuned) models with much better generalization power using fewer training data (and training iterations), which is especially useful for tasks that stem from smaller datasets. Often, in the case of DL models for image classification, there are two strategies for

[3] https://github.com/biasvariancelabs/aitlas

performing transfer learning that is being used: (1) fine-tuning the model weights only for the last, classifier layer or (2) fine-tuning the model weights of all layers in the network. The former approach, retains the values of all but the last layer's weights of the model from the pre-training, keeping them 'frozen' during fine-tuning. The latter, on the other hand, allows the weights to change throughout the entire network during fine-tuning.

In our experiments, we implement the latter approach and fine-tune each network entirely for each specific dataset. Note that, the choice of the pre-training dataset, and its relation to the domain of the downstream task, may also influence the predictive performance of the fine-tuned model [14]. However, since here we are interested in a more general evaluation that takes into account 22 different datasets, we take a standard approach, using pre-trained model architectures on the ImageNet-1K [61] dataset (version V1). More specifically, we use implementations from the PyTorch vision catalog [67] for most models, except ViT and MLPMixer for which we base the implementations on [68]. In turn, we fine-tune the entire parameter set. In practice, this can lead to better generalization and higher accuracy [95, 96], thereof.

3.3 Evaluation measures

Assessing the performance of machine learning models is a non-trivial task, specific to the learning task at hand and dependent on the general objectives of the model being learned. Different evaluation measures capture different aspects of the models' behavior and their predictive power on novel examples, not used for training. Since the goal of this study analyzing the predictive performance of different DL models across different datasets on multi-class and multi-label classification tasks – we examine the experimental work through the lens of evaluation measures most suitable for these two tasks.

More specifically, for multi-class classification tasks, we report the following measures: Accuracy, Macro Precision, Weighted Precision, Macro Recall, Weighted Recall, Macro F1 score, and Weighted F1 score. Note that, since for these tasks the micro-averaged measures such as F1 score, Micro Precision, and Micro Recall have values equal to accuracy, we do not report them. Note that, for image classification tasks is customary to report *top-n accuracy* (typically n is set to 1 or 5) [61], where the score is computed based on the correct label being among the n most probable labels outputted by the model. In this paper, we report *top-1 accuracy*, denoted as 'Accuracy' unless stated otherwise. For multi-label classification tasks, we report Micro Precision, Macro Precision, Weighted Precision, Micro Recall, Macro Recall, Weighted Recall, Micro F1 score, Macro F1 score, Weighted F1 score, and mean average precision (mAP). Since all measures, but mAP, require setting a threshold on the predictions, we choose a threshold value of 0.5 for all models and settings. Further details and definitions of the evaluation measures used in the study are given in Appendix A. We also provide additional performance details in terms of confusion matrices of each experiment, allowing for a more detailed (per class/label) analysis of model performance (reported in Appendix C).

4 Results

We present the results of a large-scale study in which we compare different DL models for multi-class (MCC) and multi-label classification (MLC) tasks from 22 datasets. To this end, we evaluate models from 9 architectures: AlexNet, VGG16, ResNet50, ResNet152, DenseNet162, EfficientNetB0, ConvNeXt, Vision Transformer (ViT), and MLPMixer. For each model architecture, we evaluate two variants: (i) models trained from scratch and (2) fine-tuned models previously trained on the ImageNet-1K dataset. In the reminder, we outline and discuss:

1. The performance of models trained from scratch with respect to the two types of tasks
2. The benefits of pre-training models of different architectures, and their effect in view of the dataset properties
3. The 'performance vs. cost of model training' trade-off between the considered modeling approaches

Detailed results of each experiment, with additional performance measures, are presented in Appendices B and C

4.1 Training models from scratch

We begin by analyzing the performance of models trained from scratch, i.e., models initialized with random weights during training. Tables 4 and 5 present these results for the MCC and MLC tasks, respectively. Table 4 reports the accuracy (%) of the models learned from scratch for the 15 MCC datasets. It also reports the rank of the models, estimated based on their performance and averaged over the 15 datasets. In general, the results show

Table 4: Accuracy (%) of models trained from scratch on multi-class classification datasets. Bold indicates best performing model for a given dataset. We report the *average rank* of a model (lower is better), ranked based on the performance and averaged across the 15 datasets.

Dataset \Model	AlexNet	VGG16	ResNet50	ResNet152	DenseNet161	EfficientNetB0	ViT	MLPMixer	ConvNeXt
WHU-RS19	66.169	68.657	79.602	80.597	**80.597**	75.622	74.627	69.652	72.139
Optimal31	55.108	56.720	67.204	62.903	**71.237**	68.548	62.634	59.140	58.871
UC merced	81.190	78.571	85.238	84.048	**86.190**	84.286	83.095	82.381	84.286
SIRI-WHU	83.750	84.792	**88.958**	88.750	86.667	86.042	86.250	82.500	84.167
RSSCN7	80.536	81.607	82.679	82.679	**87.321**	83.929	86.071	83.214	83.036
BCS	89.410	89.410	89.236	88.542	**90.799**	85.417	87.847	86.285	84.375
AID	81.350	81.950	89.050	89.900	**93.300**	90.050	79.350	71.750	81.100
CLRS	71.400	76.067	85.567	82.300	**86.167**	82.267	65.467	61.133	69.167
RSI-CB256	97.354	98.828	98.828	**99.152**	99.131	99.111	98.121	98.424	98.444
Eurosat	96.167	97.185	97	97.407	97.630	**97.796**	95.037	95.500	95.426
PatternNet	97.829	97.911	99.063	98.882	**99.243**	98.832	96.694	98.832	97.829
RESISC45	82.159	83.889	92.333	90.683	**93.460**	91.365	81.016	69.413	85.937
RSD46-WHU	86.032	88.625	90.549	89.944	92.211	90.612	86.466	81.253	88.693
So2Sat	56.511	62.271	59.587	61.477	55.428	**65.173**	55.333	53.580	60.154
SAT6	99.272	99.564	**100**	99.998	99.995	99.998	99.985	99.984	99.998
Avg. Rank	7.27	5.8	3.13	3.27	**1.93**	3.13	6.60	7.33	5.87

that convolutional architectures, especially the DenseNet, the EfficientNet, and the two ResNets, consistently perform well. This is even more evident for datasets such as PatternNet, RSI-CB256, and SAT6, where the DenseNet (and the other top-ranked models) lead to near-perfect results (accuracy greater than 99%). More specifically, DenseNet is the best performing model in more than half of the tasks (9 out of 15) and achieves accuracy greater than 90% in 8 of the tasks. For smaller datasets, such as WHU-RS19, Optimal31, UC Merced, SIRI-WHU, RSSCN7 and CLRS, these performances are generally much lower. However, the most challenging task is *So2SAT*, where EfficientNetB0 achieves the highest accuracy of 65.17%, while many of the models trail behind with performance of 55-60%. While these results are consistent with previous findings [35], this is a clear sign of over-fitting, influenced by the quality and size of the images in the dataset. The ViT, MLPMixer, and the latest ConvNeXt models are ranked in the bottom 4 (only better than AlexNet). Their performance is lower, but still practically competitive with the leading DenseNet for many datasets.

The general conclusions outlined above also apply to MLC tasks. Table 5 reports on the mean average precision (%) of the models learned from scratch across the 7 MLC datasets. The DenseNets rank the best (they provide the best result for 2 out of 7 tasks). However, unlike the MCC tasks, the performance difference to other convolutional models (i.e., the two ResNets and the EfficientNetB0) is much smaller. Moreover, models were only able to achieve high performance (above 90%) on two tasks, *DFC15* and *MLRSNet*, with DenseNet and ResnNet50 achieving the best results. However, this is an expected result, as MLC tasks are generally more challenging than MCC tasks. This can be attributed to two things in particular: First, in many cases, the semantic labels can be very similar, which makes many of the models to struggle. Second, MLC datasets tend to have a greater class/label imbalance, in contrast to the more uniform class distribution in MCC datasets. In this context, the most challenging MLC tasks overall are *PlanetUAS* and *BigEarthNet43*, where the best performing models (the two ResNets) achieve mAP od 64.96% and 64.34%

Table 5: Mean average precision (mAP %) of models trained from scratch on multi-label classification datasets. Bold indicates best performing model for a given dataset. We report the *average rank* of a model (lower is better), ranked based on the performance and averaged across the 7 datasets.

Dataset \Model	AlexNet	VGG16	ResNet50	ResNet152	DenseNet161	EfficientNetB0	ViT	MLPMixer	ConvNeXt
AID	68.780	69.206	70.867	69.646	71.218	**72.889**	65.581	64.235	65.595
UC Merced	75.516	76.797	79.867	73.657	85.414	79.874	**87.142**	75.677	72.271
DFC15	88.099	89.871	94.675	94.188	**95.848**	93.973	94.164	91.663	89.564
Planet UAS	60.282	60.682	64.192	**64.956**	64.738	63.868	59.414	58.550	61.277
MLRSNet	90.850	91.524	**95.259**	93.982	94.745	94.395	87.250	85.281	90.710
BigEarthNet 19	75.711	77.989	78.726	78.519	**79.725**	79.211	75.871	77.005	77.909
BigEarthNet 43	56.082	58.969	**64.343**	62.736	63.390	62.173	57.410	58.772	60.472
Avg. Rank	7.57	5.57	2.43	3.86	**1.71**	3.14	6.43	7.57	6.71

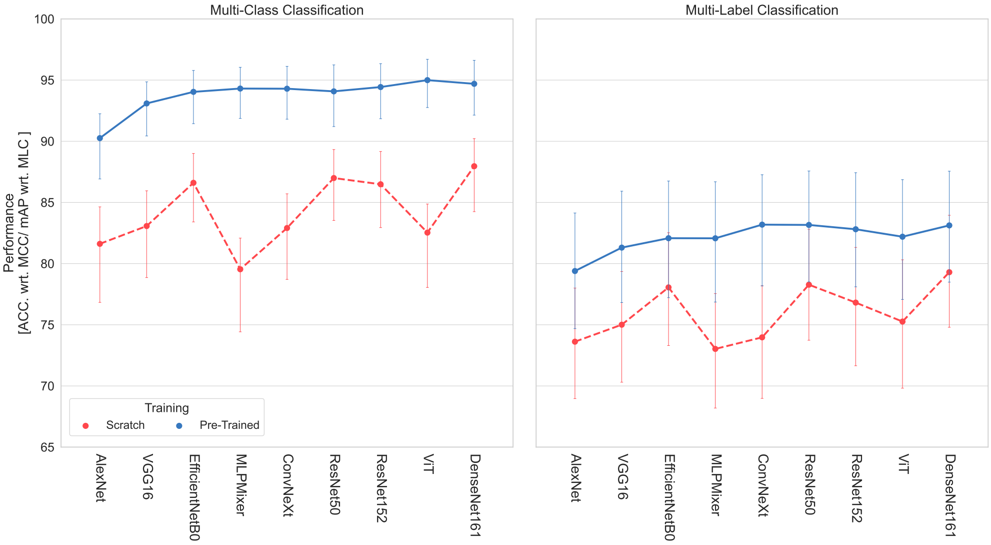

Figure 2: **Comparison of average performance improvement** of models from the 9 different architectures when **(red)** trained from scratch and **(blue)** employing pre-trained models across **(left)** MCC and **(right)** MLC datasets. Error bars indicate confidence interval of 68%. Models are ordered (worst to best) based on the average performance-rank of the pre-trained variants across all of the 22 datasets. Model pre-training leads to substantial performance improvements.

, respectively. Finally, similar to the previous MCC analysis, ViT, MLPMixer, and ConvNeXt remain only better ranked than AlexNet. Nevertheless, their performance on these MLC tasks is much more competitive, for instance, in the case of ViT, which is the best model on the *UC Merced* task.

4.2 The benefits of using pre-trained models

While training models from scratch leads to decent performance (in general), in practice, leveraging pre-trained models can lead to significant performance improvements on image classification tasks [32], and in particular on tasks in EO domains [94].

This is also the general conclusion from our analysis. When using models that were first pre-trained on ImageNet-1K and then fine-tuned on the specific datasets, we found that: *Pre-trained models lead to substantial performance improvements compared to models trained from scratch.* Figure 2 illustrates this performance-improvement trend for different models across the 22 MCC and MLC tasks. We find that pre-training significantly improves the performance of all the evaluated models. Notably, we observe that ViT models benefit the most from pre-training, followed by MLPMixer and ConvNeXt models. This is a significant improvement over the models trained from scratch. These results, especially for the case of ViT, are consistent with previously reported findings [39, 30].

Tables 6 and 7 present the detailed results of these analyses for MCC and MLC tasks, respectively. Similarly to the analyses in the previous section, we report model accuracy (%) in the case of MCC tasks and mean average precision (%) in the case of MLC tasks. We also report the rank of the models, averaged over the respective datasets. Considering MCC tasks (Table 6), the models achieve very good performance (accuracy over 90%) on 14 (out of 15) tasks, with (almost) perfect results in five of those. Notably, we observed significant performance improvements, compared to model-counterparts trained from scratch, on smaller datasets (such as *WHU-RS19, Optimal31, UC Merced, SIRI-WHU, RSSCN7, and CLRS*), reaffirming the utility of transfer learning from large datasets in the context of EO image classification tasks. In terms of model architectures, DenseNet ranks at the top among the model architectures. However, in contrast to our previous analysis of models trained from scratch, here the ranking is not the clearest indicator of overall performance: In many cases, the performance of ViTs is practically identical to DenseNets, achieving best performance in 6 out of 15 cases. This is further highlighted for the case of the challenging *So2SAT* task, where the ViT model leads to an accuracy of 68.55%, in contrast to DenseNet with an accuracy of 65.75%. In this specific case, we observed that over-fitting remains an issue, even for pre-trained models. Our inspection of the train/vali-

Table 6: Accuracy (%) of models pre-trained on ImageNet-1K on multi-class classification datasets. Bold indicates best performing model for a given dataset. We report the *average rank* of a model (lower is better), ranked based on the performance and averaged across the 15 datasets.

Dataset\Model	AlexNet	VGG16	ResNet50	ResNet152	DenseNet161	EfficientNetB0	ViT	MLPMixer	ConvNeXt
WHU-RS19	93.532	99.005	99.502	98.010	**100**	99.502	99.502	98.507	99.005
Optimal31	80.914	88.710	92.204	92.473	94.355	91.667	**94.624**	92.742	93.011
UC merced	92.143	95.476	98.571	**98.810**	98.333	98.571	98.333	98.333	97.857
SIRI-WHU	92.292	93.958	95	**96.250**	95.625	95	95.625	95.208	96.250
RSSCN7	91.964	93.929	95	95	94.821	95.536	**95.893**	95.179	94.643
BCS	89.583	90.972	92.014	92.361	92.708	91.319	92.014	**93.056**	91.493
AID	92.900	96.100	96.550	97.200	97.250	96.250	**97.750**	96.700	96.950
CLRS	84.100	89.900	91.567	91.900	92.200	90.500	**93.200**	90.100	91.100
RSI-CB256	99.354	99.051	99.677	**99.859**	99.737	99.717	99.758	99.657	99.596
Eurosat	97.574	98.148	98.833	**99.000**	98.889	98.907	98.722	98.741	98.778
PatternNet	99.161	99.424	**99.737**	99.490	**99.737**	99.539	99.655	99.704	99.671
RESISC45	90.492	93.905	96.460	96.54	96.508	94.873	**97.079**	95.952	96.270
RSD46-WHU	90.646	92.422	94.158	94.404	**94.507**	93.387	94.238	93.673	93.627
So2Sat	59.203	65.375	61.903	65.169	65.756	65.801	**68.551**	67.066	66.169
SAT6	99.980	99.993	**100**	**100**	**100**	99.988	99.998	99.995	99.999
Avg. Rank	8.93	7.67	4.07	3.27	**2.60**	5.13	2.73	4.67	4.80

Table 7: Mean average precision (mAP %) of models pre-trained on ImageNet-1K on multi-label classification datasets. Bold indicates best performing model for a given dataset. We report the *average rank* of a model (lower is better), ranked based on the performance and averaged across the 7 datasets.

Dataset \Model	AlexNet	VGG16	ResNet50	ResNet152	DenseNet161	EfficientNetB0	ViT	MLPMixer	ConvNeXt
AID	75.906	79.893	80.758	80.942	81.708	78.002	81.539	80.879	**82.298**
UC Merced	92.638	92.848	95.665	96.010	96.056	95.384	**96.699**	96.34	96.431
DFC15	94.057	96.566	97.662	97.600	97.529	96.787	97.617	97.941	**97.994**
Planet UAS	64.048	65.584	65.528	64.825	66.339	64.157	66.804	**67.330**	66.447
MLRSNet	93.399	94.633	96.272	**96.432**	96.306	95.391	96.410	95.049	95.807
BigEarthNet 19	77.147	78.418	79.983	79.776	79.686	**80.221**	77.310	77.288	77.147
BigEarthNet 43	58.554	61.205	**66.256**	64.066	64.229	64.589	58.997	59.648	66.166
Avg. Rank	8.86	6.71	4.00	4.29	3.86	5.71	3.71	4.57	**3.14**

dation loss trends showed that, with training errors decreasing, validation errors increased almost instantly (after 1-2 epochs) regardless of the model at hand. This fortunately is not the case for the remaining tasks, where we observed a decent performance overall. The models, especially the top-half ranked, achieved stable and mostly comparable performance.

The benefits of pre-training models extend also to MLC tasks (Table 7), although, the performance gains, compared to model counterparts trained from scratch, are not as large as for MCC tasks. In particular, we found that pre-training can lead to small improvements (1%-2%) on challenging tasks such as *PlanetUAS* and *BigEarthNet43* (mAP of 67.33% and 66.26% achieved by Resnet50 and EfficientNetB0, respectively); to more considerable improvements (up to 10%) in some cases such as *AID* and *UCMerced* (mAP of 82.29% and 96.7% obtained by ConvNeXt and ViT, respectively). We also found that the ConvNeXt models benefited the most from pre-training - they ranked the best overall and achieved best performance on 2 (out of the 7) tasks. They are followed by ViT and DenseNet, which perform comparably on most tasks.

4.3 *The 'performance vs. training cost' trade-off*

Having established the baseline performance of our evaluated models and demonstrated the clear benefits of using pre-trained models, we focus here on another line of comparison - the cost of model training. Recall from Section 2.2, and in particular Table 3, that we study model architectures that differ significantly in the number of learnable parameters. Typically, larger models require, not only more computing resources, but also much more training time than smaller models. In our experimental setup, we train all models on the same computing infrastructure, under the same conditions, and with the same training/evaluation setup (in terms of hyperparameters and data partitioning). Therefore we can directly analyze the 'performance vs. training cost' (in terms of total training time) trade-off, for each model variant from the 9 different architectures (either pre-trained or trained from scratch), across the 22 datasets. This way,

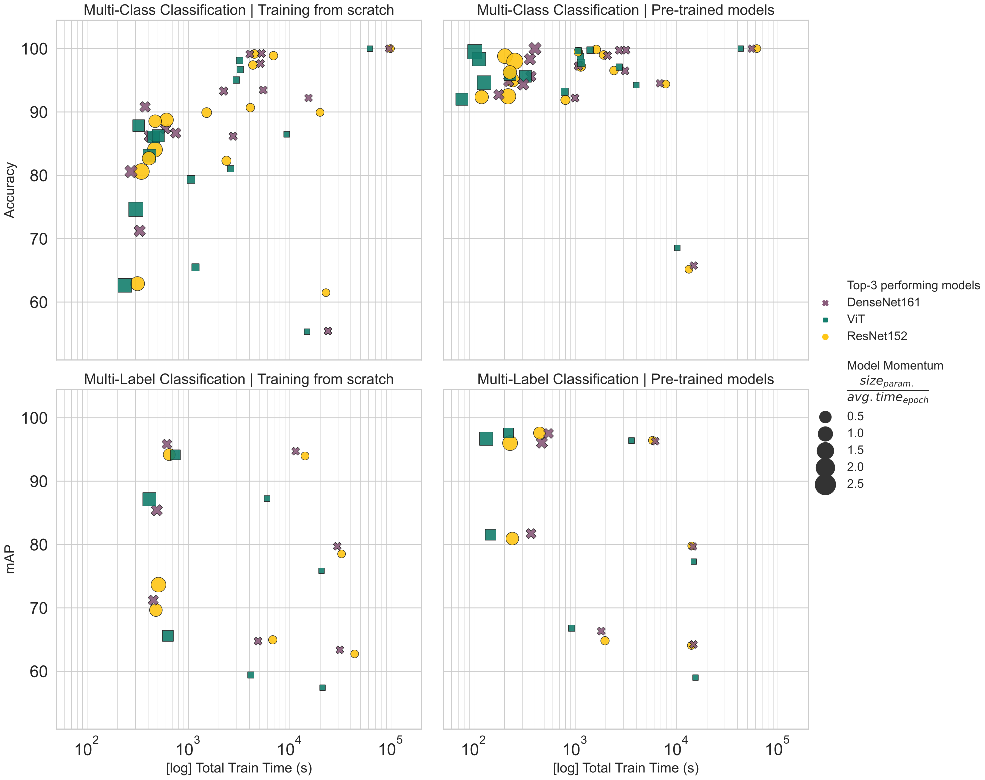

Figure 3: **Performance vs. total training time** comparison of the top-3 overall ranked model architectures, **(left)** when trained from scratch and **(right)** when employing pre-trained models on (**top**) MCC and **(bottom)** MLC tasks. Performance is reported as accuracy (%) and mean average precision (mAP %) for MCC and MLC tasks, respectively. Note that log scale of the total training time (seconds). The models are denoted with different colors and markers, with the size of the marker denoting *model momentum*: The Ratio between the model size (in terms of number of parameters) and average time per training epoch taken by the model. Generally, ViTs are faster to train than DenseNet and ResNet152, archiving comparable performance esp. with pre-trained model variants.

we can explicitly measure the benefits of each model and make further modeling decisions based on the performance of the models and the ’cost’ of training them.

Figure 3 illustrates the trade-off for the top-3 performing model architectures, overall: DenseNet, ViT, and ResNet152. More specifically, it shows all trained models of these 3 architectures, including pre-trained and trained from scratch variants, applied on MCC and MLC tasks. While the performance analyzes showed many similarities between these models, in terms of training times, the difference between them is much more obvious. In general, ViT requires less training time than both DenseNets and ResNet152, even though DenseNets have near a quarter of the number of parameters of ViT. This difference is even more pronounced for pre-trained models. Here, ViT models usually lead to comparable/better predictive performance than DenseNet models, requiring (in some cases) up to half the training time.

We can further analyze these training-time trends for each model and dataset, as presented in Figure 4. In particular, Figure 4(a,b) illustrates the total training times of each pre-trained model as a fraction of the cumulative training time of all models (per dataset). This confirms that, in many cases, ViT models can be trained almost twice as fast as models from the other top-performing architectures, such as DenseNet and ResNet152. The training cost of ViT models is similar to that of EfficientNetB0, ConvNeXt, and MLPMixer, which are efficient ’by design’, but perform worse on these tasks. Figure 4(c,d) shows further details about the training times, but in terms of the average training time per epoch. On average, epochs when fine-tuning pre-trained models last a bit less than epochs when training models from scratch. However, in terms of total time, using pre-trained models almost halves the training time as compared

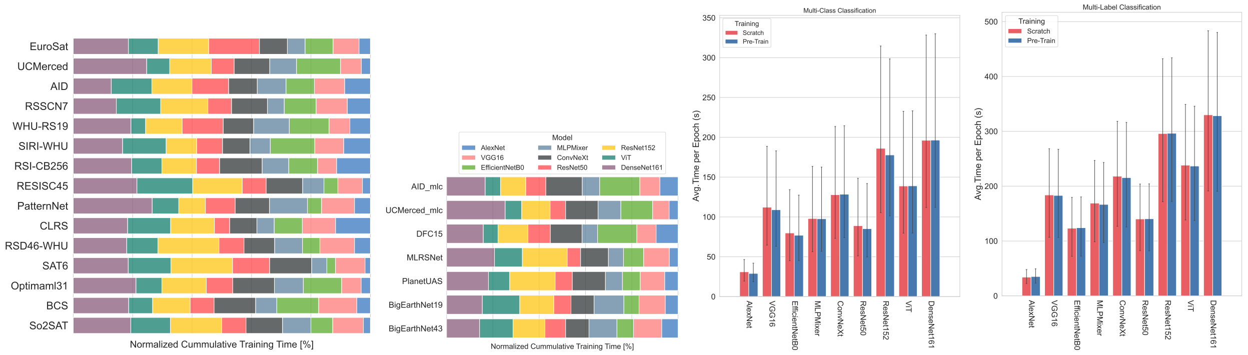

(a) MCC tasks (total time)

(b) MLC tasks (total time)

(c) MCC tasks (avg.time/epoch)

(d) MLC tasks (avg. time/epoch)

Figure 4: **Total training time** of pre-trained models for each of the **(a)** MCC and **(b)** MLC datasts. The training time of each model architecture (denoted with different colors) is depicted as a fraction (%) of the cumulative training time for each dataset. Furthermore, (c) and (d) illustrate the average time per epoch of each model variant on **(c)** MCC and **(d)** MLC tasks, comparing the **(red)** pre-trained model variants (from (a) and (b)) to their counterparts **(blue)** trained from scratch.

to training them from scratch (see Appendix B). This, in general, is an expected behavior, which nevertheless can help designing and planning DL pipelines for similar EO applications. Note, however, that we do not take into account the time needed to pre-train each model, which will certainly increase the total training times significantly.

5 Conclusions

We present a systematic review and evaluation of several modern DL architectures applied in the context of Earth Observation. More specifically, we introduce *AiTLAS: Benchmark Arena* – an *open-source EO benchmark framework* and demonstrate its utility with a comprehensive comparative analysis of models from nine different state-of-the-art DL architectures, comparing them to a variety of multi-class and multi-label image classification tasks from 22 datasets. We compare models trained from scratch as well as pre-trained models under the same conditions and with the same hardware. We evaluate more than 400 different models with different architectures and learning paradigms across tasks from 22 datasets with different sizes and properties. To our knowledge, the evaluation of these different setups (in terms of machine learning tasks, model setups, model architectures, and datasets) makes this the largest and most comprehensive empirical studies of deep learning methods applied to EO datasets to date. All of the important details about the study design as well as the results and trained models are freely available. This will contribute to more systematic and rigorous experiments in future work and, more importantly, will enable better usability and faster development of novel approaches. We believe that both this study and the associated repository can serve as a starting point and a guiding design principle for evaluating and documenting machine learning approaches in the different domains of EO. More importantly, we hope that with further involvement from the community, AiTLAS: Benchmark Arena can become a reference point for further studies in this highly active research area.

More broadly, we believe that this work, along with the resources developed, will have a strong impact on the AI and EO research communities. First, such ready-to-use resources containing trained models, clear experimental designs, and detailed results will facilitate better adoption of sophisticated modeling approaches in the EO community - bringing the EO and AI communities closer together. Second, it demonstrates the FAIRification process of AI4EO resources, i.e., making resources adhere to the FAIR principles (Findable, Accessible, Interoperable, and Reusable [97]). Finally, it contributes to the 'Green AI' initiative by saving additional computational overhead. Since all experimental details, especially the trained models, are publicly available – other experts and researchers can compare, reproduce, and reuse these resources - reducing the need to repeatedly run unnecessary experiments.

Reproducibility

All the necessary details, in terms of the trained models, model parameters and implementations as well as details on all of the used datasets and their prepossessed versions are available at https://github.com/biasvariancelabs/aitlas-arena. All the models were trained/fine-tuned on NVIDIA A100-PCIE-40GB GPUs, running CUDA Version 11.5 (www.nvidia.com/en-gb/data-center/a100/). Note that, we do not host the datasets. To obtain them, please refer to each of the respective studies (referenced in Tables 1 and 2) or follow the links provided in our repository. The study was performed using the AiTLAS Toolbox [37], a library for exploratory and predictive analysis of satellite imaginary pertaining to different remote-sensing tasks, available at https://aitlas.bvlabs.ai.

Acknowledgements

We acknowledge the support of the European Space Agency ESA through the activity AiTLAS - AI4EO rapid prototyping environment. We thank Sofija Dimitrovska for her thoughtful feedback.

References

[1] A. Khan, A. Sohail, U. Zahoora, A. S. Qureshi, A survey of the recent architectures of deep convolutional neural networks, Artificial Intelligence Review 53 (2020) 5455–5516.

[2] S. Khan, M. Naseer, M. Hayat, S. W. Zamir, F. S. Khan, M. Shah, Transformers in vision: A survey, ACM Comput. Surv. (2021). doi:10.1145/3505244.

[3] J. E. Ball, D. T. Anderson, C. S. Chan Sr., Comprehensive survey of deep learning in remote sensing: theories, tools, and challenges for the community, Journal of Applied Remote Sensing 11 (2017) 1 – 54.

[4] D. Tuia, F. Ratle, F. Pacifici, M. F. Kanevski, W. J. Emery, Active learning methods for remote sensing image classification, IEEE Transactions on Geoscience and Remote Sensing 47 (2009) 2218–2232. doi:10.1109/TGRS.2008.2010404.

[5] M. Li, S. Zang, B. Zhang, S. Li, C. Wu, A review of remote sensing image classification techniques: the role of spatio-contextual information, European Journal of Remote Sensing 47 (2014) 389–411. doi:10.5721/EuJRS20144723.

[6] T. Blaschke, Object based image analysis for remote sensing, Isprs Journal of Photogrammetry and Remote Sensing 65 (2010) 2–16.

[7] T. Blaschke, J. Strobl, What's wrong with pixels? some recent developments interfacing remote sensing and gis, 2001.

[8] G. Cheng, J. Han, X. Lu, Remote sensing image scene classification: Benchmark and state of the art, Proceedings of the IEEE 105 (2017) 1865–1883. doi:10.1109/JPROC.2017.2675998.

[9] Y. Yang, S. Newsam, Bag-of-visual-words and spatial extensions for land-use classification, in: Proceedings of the 18th SIGSPATIAL International Conference on Advances in Geographic Information Systems, Association for Computing Machinery, 2010, p. 270–279.

[10] D. Marmanis, M. Datcu, T. Esch, U. Stilla, Deep learning earth observation classification using imagenet pretrained networks, IEEE Geoscience and Remote Sensing Letters 13 (2016) 105–109. doi:10.1109/LGRS.2015.2499239.

[11] H. Chen, V. Chandrasekar, H. Tan, R. Cifelli, Rainfall estimation from ground radar and trmm precipitation radar using hybrid deep neural networks, Geophysical Research Letters 46 (2019) 10669–10678. doi:https://doi.org/10.1029/2019GL084771.

[12] J. Castillo-Navarro, B. Le Saux, A. Boulch, S. Lefèvre, Energy-based models in earth observation: From generation to semisupervised learning, IEEE Transactions on Geoscience and Remote Sensing 60 (2022) 1–11. doi:10.1109/TGRS.2021.3126428.

[13] Y. Wang, C. M. Albrecht, N. A. A. Braham, L. Mou, X. X. Zhu, Self-supervised learning in remote sensing: A review (2022). doi:10.48550/ARXIV.2206.13188.

[14] M. Neumann, A. S. Pinto, X. Zhai, N. Houlsby, Training general representations for remote sensing using in-domain knowledge, in: IGARSS 2020 - 2020 IEEE International Geoscience and Remote Sensing Symposium, 2020, pp. 6730–6733. doi:10.1109/IGARSS39084.2020.9324501.

[15] D. Ienco, R. Gaetano, C. Dupaquier, P. Maurel, Land cover classification via multitemporal spatial data by deep recurrent neural networks, IEEE Geoscience and Remote Sensing Letters 14 (2017) 1685–1689. doi:10.1109/LGRS.2017.2728698.

[16] A. Chlingaryan, S. Sukkarieh, B. Whelan, Machine learning approaches for crop yield prediction and nitrogen status estimation in precision agriculture: A review, Computers and Electronics in Agriculture 151 (2018) 61–69. doi:https://doi.org/10.1016/j.compag.2018.05.012.

[17] Crop yield forecasting on the canadian prairies by remotely sensed vegetation indices and machine learning methods, Agricultural and Forest Meteorology 218-219 (2016) 74–84. doi:https://doi.org/10.1016/j.agrformet.2015.11.003.

[18] J. Xu, J. Yang, X. Xiong, H. Li, J. Huang, K. Ting, Y. Ying, T. Lin, Towards interpreting multi-temporal deep learning models in crop mapping, Remote Sensing of Environment 264 (2021) 112599. doi:https://doi.org/10.1016/j.rse.2021.112599.

[19] B. Ayhan, C. Kwan, B. Budavari, L. Kwan, Y. Lu, D. Perez, J. Li, D. Skarlatos, M. Vlachos, Vegetation detection using deep learning and conventional methods, Remote Sensing 12 (2020). doi:10.3390/rs12152502.

[20] Y.-H. Jo, D.-W. Kim, H. Kim, Chlorophyll concentration derived from microwave remote sensing measurements using artificial neural network algorithm, Journal of Marine Science and Technology 26 (2018). doi:10.6119/JMST.2018.02_(1).0004.

[21] H. Shirmard, E. Farahbakhsh, R. D. Müller, R. Chandra, A review of machine learning in processing remote sensing data for mineral exploration, Remote Sensing of Environment 268 (2022) 112750. doi:https://doi.org/10.1016/j.rse.2021.112750.

[22] X. Zhang, Q. Zhang, G. Zhang, Z. Nie, Z. Gui, H. Que, A novel hybrid data-driven model for daily land surface temperature forecasting using long short-term memory neural network based on ensemble empirical mode decomposition, International Journal of Environmental Research and Public Health 15 (2018).

[23] M. Sadeghi, A. A. Asanjan, M. Faridzad, P. Nguyen, K. Hsu, S. Sorooshian, D. Braithwaite, Persiann-cnn: Precipitation estimation from remotely sensed information using artificial neural networks–convolutional neural networks, Journal of Hydrometeorology 20 (2019) 2273 – 2289. doi:10.1175/JHM-D-19-0110.1.

[24] N. Longbotham, C. Chaapel, L. Bleiler, C. Padwick, W. J. Emery, F. Pacifici, Very high resolution multiangle urban classification analysis, IEEE Transactions on Geoscience and Remote Sensing 50 (2012) 1155–1170. doi:10.1109/TGRS.2011.2165548.

[25] Z. Lv, T. Liu, J. A. Benediktsson, N. Falco, Land cover change detection techniques: Very-high-resolution optical images: A review, IEEE Geoscience and Remote Sensing Magazine 10 (2022) 44–63. doi:10.1109/MGRS.2021.3088865.

[26] B. Huang, B. Zhao, Y. Song, Urban land-use mapping using a deep convolutional neural network with high spatial resolution multispectral remote sensing imagery, Remote Sensing of Environment 214 (2018) 73–86. doi:https://doi.org/10.1016/j.rse.2018.04.050.

[27] M. Somrak, S. Dzeroski, Z. Kokalj, Learning to classify structures in als-derived visualizations of ancient maya settlements with CNN, Remote. Sens. 12 (2020) 2215. doi:10.3390/rs12142215.

[28] G. Cheng, X. Xie, J. Han, L. Guo, G.-S. Xia, Remote sensing image scene classification meets deep learning: Challenges, methods, benchmarks, and opportunities, IEEE Journal of Selected Topics in Applied Earth Observations and Remote Sensing 13 (2020) 3735–3756. doi:10.1109/JSTARS.2020.3005403.

[29] R. Schneider, M. Bonavita, A. Geer, R. Arcucci, P. Dueben, C. Vitolo, B. Le Saux, B. Demir, P.-P. Mathieu, Esa-ecmwf report on recent progress and research directions in machine learning for earth system observation and prediction, npj Climate and Atmospheric Science 5 (2022) 51. doi:10.1038/s41612-022-00269-z.

[30] I. Papoutsis, N.-I. Bountos, A. Zavras, D. Michail, C. Tryfonopoulos, Efficient deep learning models for land cover image classification, arXiv:2111.09451 (2022).

[31] G.-S. Xia, J. Hu, F. Hu, B. Shi, X. Bai, Y. Zhong, L. Zhang, X. Lu, AID: A benchmark data set for performance evaluation of aerial scene classification, IEEE Transactions on Geoscience and Remote Sensing 55 (2017) 3965–3981.

[32] X. Zhai, J. Puigcerver, A. Kolesnikov, P. Ruyssen, C. Riquelme, M. Lucic, J. Djolonga, A. S. Pinto, M. Neumann, A. Dosovitskiy, L. Beyer, O. Bachem, M. Tschannen, M. Michalski, O. Bousquet, S. Gelly, N. Houlsby, A large-scale study of representation learning with the visual task adaptation benchmark, arXiv:1910.04867 (2019).

[33] L. Zhang, L. Zhang, B. Du, Deep learning for remote sensing data: A technical tutorial on the state of the art, IEEE Geoscience and Remote Sensing Magazine 4 (2016) 22–40. doi:10.1109/MGRS.2016.2540798.

[34] X. X. Zhu, D. Tuia, L. Mou, G.-S. Xia, L. Zhang, F. Xu, F. Fraundorfer, Deep learning in remote sensing: A comprehensive review and list of resources, IEEE Geoscience and Remote Sensing Magazine 5 (2017) 8–36. doi:10.1109/MGRS.2017.2762307.

[35] A. J. Stewart, C. Robinson, I. A. Corley, A. Ortiz, J. M. L. Ferres, A. Banerjee, Torchgeo: deep learning with geospatial data, CoRR abs/2111.08872 (2021). arXiv:2111.08872.

[36] G. Sumbul, A. de Wall, T. Kreuziger, F. Marcelino, H. Costa, P. Benevides, M. Caetano, B. Demir, V. Markl, BigEarthNet-MM: A large-scale, multimodal, multilabel benchmark archive for remote sensing image classification and retrieval [software and data sets], IEEE Geoscience and Remote Sensing Magazine 9 (2021) 174–180.

[37] I. Dimitrovski, I. Kitanovski, P. Panov, N. Simidjievski, D. Kocev, Aitlas: Artificial intelligence toolbox for earth observation, CoRR abs/2201.08789 (2022). arXiv:2201.08789.

[38] A. Paszke, S. Gross, F. Massa, A. Lerer, J. Bradbury, G. Chanan, T. Killeen, Z. Lin, N. Gimelshein, L. Antiga, A. Desmaison, A. Kopf, E. Yang, Z. DeVito, M. Raison, A. Tejani, S. Chilamkurthy, B. Steiner, L. Fang, J. Bai, S. Chintala, Pytorch: An imperative style, high-performance deep learning library, in: Advances in Neural Information Processing Systems 32, Curran Associates, Inc., 2019, pp. 8024–8035.

[39] A. Dosovitskiy, L. Beyer, A. Kolesnikov, D. Weissenborn, X. Zhai, T. Unterthiner, M. Dehghani, M. Minderer, G. Heigold, S. Gelly, et al., An image is worth 16x16 words: Transformers for image recognition at scale, arXiv preprint arXiv:2010.11929 (2020).

[40] G. Huang, Z. Liu, L. Van Der Maaten, K. Q. Weinberger, Densely connected convolutional networks, in: Proceedings of the IEEE conference on computer vision and pattern recognition, 2017, pp. 4700–4708.

[41] G. Tsoumakas, I. Katakis, Multi-label classification: An overview, International Journal of Data Warehousing and Mining 3 (2009) 1–13.

[42] G.-S. Xia, W. Yang, J. Delon, Y. Gousseau, H. Sun, H. Maître, Structural high-resolution satellite image indexing, International Archives of the Photogrammetry, Remote Sensing and Spatial Information Sciences - ISPRS Archives 38 (2010).

[43] P. Helber, B. Bischke, A. Dengel, D. Borth, Eurosat: A novel dataset and deep learning benchmark for land use and land cover classification, IEEE Journal of Selected Topics in Applied Earth Observations and Remote Sensing (2019).

[44] W. Zhou, S. Newsam, C. Li, Z. Shao, Patternnet: A benchmark dataset for performance evaluation of remote sensing image retrieval, ISPRS journal of photogrammetry and remote sensing 145 (2018) 197–209.

[45] G. Cheng, J. Han, X. Lu, Remote sensing image scene classification: Benchmark and state of the art, Proceedings of the IEEE 105 (2017) 1865–1883.

[46] H. Li, X. Dou, C. Tao, Z. Wu, J. Chen, J. Peng, M. Deng, L. Zhao, Rsi-cb: A large-scale remote sensing image classification benchmark using crowdsourced data, Sensors 20 (2020) 1594. doi:doi.org/10.3390/s20061594.

[47] Q. Zou, L. Ni, T. Zhang, Q. Wang, Deep learning based feature selection for remote sensing scene classification, IEEE Geoscience and Remote Sensing Letters 12 (2015) 2321–2325. doi:10.1109/LGRS.2015.2475299.

[48] S. Basu, S. Ganguly, S. Mukhopadhyay, R. DiBiano, M. Karki, R. Nemani, Deepsat: A learning framework for satellite imagery, in: Proceedings of the 23rd SIGSPATIAL International Conference on Advances in Geographic Information Systems, SIGSPATIAL '15, Association for Computing Machinery, 2015.

[49] Q. Zhu, Y. Zhong, B. Zhao, G.-S. Xia, L. Zhang, Bag-of-visual-words scene classifier with local and global features for high spatial resolution remote sensing imagery, IEEE Geoscience and Remote Sensing Letters 13 (2016) 747–751.

[50] H. Li, H. Jiang, X. Gu, J. Peng, W. Li, L. Hong, C. Tao, Clrs: Continual learning benchmark for remote sensing image scene classification, Sensors 20 (2020).

[51] Y. Long, Y. Gong, Z. Xiao, Q. Liu, Accurate object localization in remote sensing images based on convolutional neural networks, IEEE Transactions on Geoscience and Remote Sensing 55 (2017) 2486–2498.

[52] Q. Wang, S. Liu, J. Chanussot, X. Li, Scene classification with recurrent attention of vhr remote sensing images, IEEE Transactions on Geoscience and Remote Sensing 57 (2019) 1155–1167.

[53] O. A. Penatti, K. Nogueira, J. A. Dos Santos, Do deep features generalize from everyday objects to remote sensing and aerial scenes domains?, in: Proceedings of the IEEE conference on computer vision and pattern recognition workshops, 2015, pp. 44–51.

[54] X. X. Zhu, J. Hu, C. Qiu, Y. Shi, J. Kang, L. Mou, H. Bagheri, M. Haberle, Y. Hua, R. Huang, L. Hughes, H. Li, Y. Sun, G. Zhang, S. Han, M. Schmitt, Y. Wang, So2sat lcz42: A benchmark data set for the classification of global local climate zones [software and data sets], IEEE Geoscience and Remote Sensing Magazine 8 (2020) 76–89.

[55] B. Chaudhuri, B. Demir, S. Chaudhuri, L. Bruzzone, Multilabel remote sensing image retrieval using a semisupervised graph-theoretic method, IEEE Transactions on Geoscience and Remote Sensing 56 (2018) 1144–1158.

[56] X. Qi, P. Zhu, Y. Wang, L. Zhang, J. Peng, M. Wu, J. Chen, X. Zhao, N. Zang, P. T. Mathiopoulos, Mlrsnet: A multi-label high spatial resolution remote sensing dataset for semantic scene understanding, ISPRS Journal of Photogrammetry and Remote Sensing 169 (2020) 337–350.

[57] Y. Hua, L. Mou, X. X. Zhu, Recurrently exploring class-wise attention in a hybrid convolutional and bidirectional LSTM network for multi-label aerial image classification, ISPRS Journal of Photogrammetry and Remote Sensing 149 (2019) 188–199.

[58] G. Sumbul, M. Charfuelan, B. Demir, V. Markl, Bigearthnet: A large-scale benchmark archive for remote sensing image understanding, IGARSS 2019 - 2019 IEEE International Geoscience and Remote Sensing Symposium (2019) 5901–5904.

[59] Y. Hua, L. Mou, X. X. Zhu, Relation network for multilabel aerial image classification, IEEE Transactions on Geoscience and Remote Sensing 58 (2020) 4558–4572.

[60] Kaggle, Planet: Understanding the amazon from space, 2022. URL: https://www.kaggle.com/competitions/planet-understanding-the-amazon-from-space, last accessed 21 May 2022.

[61] A. Krizhevsky, I. Sutskever, G. E. Hinton, Imagenet classification with deep convolutional neural networks, Advances in neural information processing systems 25 (2012) 1097–1105.

[62] K. Simonyan, A. Zisserman, Very deep convolutional networks for large-scale image recognition, arXiv preprint arXiv:1409.1556 (2014).

[63] K. He, X. Zhang, S. Ren, J. Sun, Deep residual learning for image recognition, in: Proceedings of the IEEE conference on computer vision and pattern recognition, 2016, pp. 770–778.

[64] M. Tan, Q. Le, Efficientnet: Rethinking model scaling for convolutional neural networks, in: International conference on machine learning, PMLR, 2019, pp. 6105–6114.

[65] Z. Liu, H. Mao, C.-Y. Wu, C. Feichtenhofer, T. Darrell, S. Xie, A convnet for the 2020s, arXiv preprint arXiv:2201.03545 (2022).

[66] I. O. Tolstikhin, N. Houlsby, A. Kolesnikov, L. Beyer, X. Zhai, T. Unterthiner, J. Yung, A. Steiner, D. Keysers, J. Uszkoreit, et al., Mlp-mixer: An all-mlp architecture for vision, Advances in Neural Information Processing Systems 34 (2021).

[67] S. Marcel, Y. Rodriguez, Torchvision the machine-vision package of torch, in: Proceedings of the 18th ACM international conference on Multimedia, 2010, pp. 1485–1488.

[68] R. Wightman, Pytorch image models, https://github.com/rwightman/pytorch-image-models, 2019. doi:10.5281/zenodo.4414861.

[69] Q. Weng, Z. Mao, J. Lin, W. Guo, Land-use classification via extreme learning classifier based on deep convolutional features, IEEE Geoscience and Remote Sensing Letters 14 (2017) 704–708. doi:10.1109/LGRS.2017.2672643.

[70] M. Castelluccio, G. Poggi, C. Sansone, L. Verdoliva, Land use classification in remote sensing images by convolutional neural networks (2015). doi:10.48550/ARXIV.1508.00092.

[71] X. Han, Y. Zhong, L. Cao, L. Zhang, Pre-trained alexnet architecture with pyramid pooling and supervision for high spatial resolution remote sensing image scene classification, Remote Sensing 9 (2017). doi:10.3390/rs9080848.

[72] J. Kang, M. Körner, Y. Wang, H. Taubenböck, X. X. Zhu, Building instance classification using street view images, ISPRS journal of photogrammetry and remote sensing 145 (2018) 44–59.

[73] F. Hu, G.-S. Xia, J. Hu, L. Zhang, Transferring deep convolutional neural networks for the scene classification of high-resolution remote sensing imagery, Remote Sensing 7 (2015) 14680–14707. doi:10.3390/rs71114680.

[74] I. Goodfellow, Y. Bengio, A. Courville, Deep Learning, MIT Press, 2016. http://www.deeplearningbook.org.

[75] S. Zagoruyko, N. Komodakis, Wide residual networks (2016). doi:10.48550/ARXIV.1605.07146.

[76] G. Cheng, J. Han, X. Lu, Remote sensing image scene classification: Benchmark and state of the art, Proceedings of the IEEE 105 (2017) 1865–1883.

[77] N. Audebert, B. Le Saux, S. Lefèvre, Beyond rgb: Very high resolution urban remote sensing with multimodal deep networks, ISPRS Journal of Photogrammetry and Remote Sensing 140 (2018) 20–32.

[78] J. Zhang, C. Lu, X. Li, H.-J. Kim, J. Wang, A full convolutional network based on densenet for remote sensing scene classification, Mathematical Biosciences and Engineering 16 (2019) 3345–3367. doi:10.3934/mbe.2019167.

[79] W. Tong, W. Chen, W. Han, X. Li, L. Wang, Channel-attention-based densenet network for remote sensing image scene classification, IEEE Journal of Selected Topics in Applied Earth Observations and Remote Sensing 13 (2020) 4121–4132. doi:10.1109/JSTARS.2020.3009352.

[80] F. Chen, J. Y. Tsou, Drsnet: Novel architecture for small patch and low-resolution remote sensing image scene classification, International Journal of Applied Earth Observation and Geoinformation 104 (2021) 102577. doi:https://doi.org/10.1016/j.jag.2021.102577.

[81] T.-Y. Lin, P. Dollár, R. Girshick, K. He, B. Hariharan, S. Belongie, Feature pyramid networks for object detection, in: 2017 IEEE Conference on Computer Vision and Pattern Recognition (CVPR), 2017, pp. 936–944. doi:10.1109/CVPR.2017.106.

[82] S. Liu, C. He, H. Bai, Y. Zhang, J. Cheng, Light-weight attention semantic segmentation network for high-resolution remote sensing images, in: IGARSS 2020-2020 IEEE International Geoscience and Remote Sensing Symposium, IEEE, 2020, pp. 2595–2598.

[83] Z. Tian, W. Wang, B. Tian, R. Zhan, J. Zhang, Resolution-aware network with attention mechanisms for remote sensing object detection., ISPRS Annals of Photogrammetry, Remote Sensing & Spatial Information Sciences 5 (2020).

[84] H. Alhichri, A. S. Alswayed, Y. Bazi, N. Ammour, N. A. Alajlan, Classification of remote sensing images using efficientnet-b3 cnn model with attention, IEEE Access 9 (2021) 14078–14094. doi:10.1109/ACCESS.2021.3051085.

[85] J. Devlin, M.-W. Chang, K. Lee, K. Toutanova, Bert: Pre-training of deep bidirectional transformers for language understanding, arXiv preprint arXiv:1810.04805 (2018).

[86] Y. Bazi, L. Bashmal, M. M. A. Rahhal, R. A. Dayil, N. A. Ajlan, Vision transformers for remote sensing image classification, Remote Sensing 13 (2021). doi:10.3390/rs13030516.

[87] N. Gong, C. Zhang, H. Zhou, K. Zhang, Z. Wu, X. Zhang, Classification of hyperspectral images via improved cycle-mlp, IET Computer Vision 16 (2022) 468–478. doi:https://doi.org/10.1049/cvi2.12104.

[88] S. Liu, C. He, H. Bai, Y. Zhang, J. Cheng, Light-weight attention semantic segmentation network for high-resolution remote sensing images, in: IGARSS 2020 - 2020 IEEE International Geoscience and Remote Sensing Symposium, 2020, pp. 2595–2598. doi:10.1109/IGARSS39084.2020.9324723.

[89] Z. Xu, W. Zhang, T. Zhang, Z. Yang, J. Li, Efficient transformer for remote sensing image segmentation, Remote Sensing 13 (2021). doi:10.3390/rs13183585.

[90] Z. Meng, F. Zhao, M. Liang, Ss-mlp: A novel spectral-spatial mlp architecture for hyperspectral image classification, Remote Sensing 13 (2021). doi:10.3390/rs13204060.

[91] K. Sechidis, G. Tsoumakas, I. Vlahavas, On the stratification of multi-label data, in: Proceedings of the 2011 European Conference on Machine Learning and Knowledge Discovery in Databases - Volume Part III, Springer-Verlag, 2011, p. 145–158.

[92] L. Liu, H. Jiang, P. He, W. Chen, X. Liu, J. Gao, J. Han, On the variance of the adaptive learning rate and beyond, in: Proceedings of the Eighth International Conference on Learning Representations (ICLR 2020), 2020.

[93] D. P. Kingma, J. Ba, Adam: A method for stochastic optimization, arXiv preprint arXiv:1412.6980 (2014).

[94] V. Risojevic, V. Stojnic, do we still need imagenet pre-training in remote sensing scene classification? (????).

[95] J. Yosinski, J. Clune, Y. Bengio, H. Lipson, How transferable are features in deep neural networks?, in: Proceedings of the 27th International Conference on Neural Information Processing Systems - Volume 2, 2014, p. 3320–3328.

[96] S. Kornblith, J. Shlens, Q. V. Le, Do better imagenet models transfer better?, in: 2019 IEEE/CVF Conference on Computer Vision and Pattern Recognition (CVPR), 2019, pp. 2656–2666.

[97] M. D. Wilkinson, M. Dumontier, I. J. Aalbersberg, G. Appleton, M. Axton, A. Baak, N. Blomberg, J.-W. Boiten, L. B. da Silva Santos, P. E. Bourne, et al., The FAIR guiding principles for scientific data management and stewardship, Scientific Data 3 (2016) 1–9.

Appendix

Table of Contents

A Evaluation metrics

The predictive performance of machine learning models is typically assessed using different evaluation measures that capture different aspects of the models' behavior. Selecting the proper evaluation measures requires knowledge of the task and problem at hand. In order to have an unbiased and fair view of the performance, one needs to consider the models' performance along several measures and then compare their performance. In this study, we assess the performance of the models using a variety of different measures available for the machine learning tasks studied here: multi-class and multi-label classification.

Multi-class classification refers to the task where a sample can be assigned to exactly one class/label selected from a predefined set of possible classes/labels. Here, we overview several evaluation measures used for this task. Most widely used evaluation measure is *accuracy* due to its intuitive interpretation and straightforward calculation. It denotes the percentage of correctly labeled samples. *Precision* and *Recall* are defined for binary tasks (two classes, often called positive and negative class) by default. To extend the binary measures to multi-class classification tasks, we adopt the One-vs-Rest (One-vs-All) approach which converts a multi-class task into a series of binary tasks for each class/label in the target. Within this approach the sample from given class/label is treated as positive, and the samples from all the other classes/labels are treated as negative.

To calculate most of the evaluation measures, we need to define the following concepts: True Positives (TP), True Negatives (TN), False Positives (FP) and False Negatives (FN). These concepts combined together form the confusion matrix for the performance of a given model over a given dataset. The TP, TN, FP and FN are defined as follows:

- TP: the label is positive and the prediction is also positive
- TN: the label is negative and the prediction is also negative
- FP: the label is negative but the prediction is positive
- FN: the label is positive but the prediction is negative

Precision is then calculated as the fraction of correctly predicted positive observations from the total predicted positive observations:

$$Precision = \frac{TP}{TP + FP}$$

*Recall*is calculated as the fraction of correctly predicted positive observations from the available positive observations:

$$Recall = \frac{TP}{TP + FN}$$

F1 score is also a common evaluation measure used in machine learning tasks, basically it combines precision and recall through a weighted average. Therefore, this score takes both false positives and false negatives into account and is very useful, especially if we have an imbalanced class/label distribution. The F1 score can be calculated as:

$$F1 = 2 \cdot \frac{Precision \cdot Recall}{Precision + Recall}$$

These evaluation measures can then be aggregated across the multiple classes using three strategies:

- *Macro averaging*: calculate the evaluation measures for each class/label separately and then average the individual values,
- *Micro averaging*: calculate the class wise confusion matrices and then aggregate the confusion matrices into a single one (i.e., add together the TP, FP, FN and FP values for each class). The aggregated confusion matrix is then used to calculate the values for the different evaluation measures, and
- *Weighted averaging*: based on macro averaging but using the frequency of the class/label as a weight in the average calculation.

Using these aggregation strategies, we then obtain macro-averaged, micro-averaged and weighted-averaged precision, recall and F1 score. Note that micro F1 score, micro precision and micro recall yield the same values as accuracy for the multi-class classification task. Taking into account this, for the multi-class classification tasks we report the following evaluation measures: Accuracy, Macro Precision, Weighted Precision, Macro Recall, Weighted Recall, Macro F1 score and Weighted F1 score.

Multi-label classification refers to the task where a sample can be assigned to multiple class/label from a predefined set of possible classes/labels. To transform the multi-label classification task to binary classification and apply the same metrics previously defined, we adopt the binary relevance method [41] that considers each label as an independent binary problem. In our case, in each node from the output layer, we use the sigmoid activation function to obtain a probability of the input image being labeled with each of the classes/labels. In order to use these probabilities to predict the classes/labels of the image, we need to define a threshold value. The model predicts that the image contains the classes/labels with probabilities that exceed the given threshold. The threshold value controls the rate of false positives versus false negatives. Increasing the threshold reduces the number of false positives, whereas decreasing the threshold reduces the number of false negatives. In our experiments, we use threshold value of 0.5. Taking into account this transformation, we can apply the formulas from above to calculate the same evaluation measures for multi-label classification tasks. While these evaluation measures are threshold dependent, we additionally use the the *mean average precision* (mAP) - a threshold independent evaluation measure widely used in image classification tasks. mAP is calculated as the mean over the average precision values of the individual labels. Average precision summarizes a precision-recall curve as the weighted mean of the precision values obtained at each threshold, with the increase in recall from the previous threshold used as the weight:

$$AP = \sum_{n}(R_n - R_{n-1})P_n$$

Where P_n and R_n are the precision and recall at the n-th threshold. It is a useful metric to compare how well models are ordering the predictions, without considering any specific decision threshold.

For the multi-label classification task, we report the following evaluation measures: Micro Precision, Macro Precision, Weighted Precision, Micro Recall, Macro Recall, Weighted Recall, Micro F1 score, Macro F1 score, Weighted F1 score and mean average precision (mAP). All measures but mAP, require setting a threshold on the predictions. Here, we set the threshold value at 0.5 for all the models and settings.

For both tasks, we provide the means to perform even more detailed analysis of the performance by reporting the confusion matrices as a performance summary of the models. The confusion matrices provide detailed per class/label view of the models' performance.

B Training Time Details

Table B.8: Multi-class classification tasks.

		AlexNet		VGG16		ResNet50		RestNet152		DenseNet161		EfficientNetB0		ViT		MLPMixer		ConvNeXt	
		Pt.	Sc.	Pt.	Sc.	Pt.	Sc.	Pt.	Sc.	Pt.	Sc.	Pt.	Sc.	Pt.	Sc.	Pt.	Sc.	Pt.	Sc.
Eurosat	Avg time/epoch (sec.)	8.88	8.02	33.69	33.62	26.56	26.45	56	56.21	61.12	62.5	23.47	24.19	43.19	44.22	30.41	31.45	40.38	40.03
	Total training time (sec.)	426	802	977	2622	1912	2619	1904	4328	2078	5125	1056	2032	1123	2963	669	2327	1050	2642
	Best epoch	38	95	19	63	62	84	24	62	24	67	35	69	16	52	12	59	16	51
UCMerced	Avg time/epoch (sec.)	1.29	1.3	3.16	4.66	2.85	2.54	5.05	5.02	5.41	5.46	2.46	2.53	4	4.44	3.1	3.06	3.68	3.75
	Total training time (sec.)	44	126	101	466	111	178	202	467	357	415	214	253	112	413	130	269	173	375
	Best epoch	24	82	22	85	29	55	30	78	56	61	77	93	18	78	32	73	37	92
AID	Avg time/epoch (sec.)	21.32	19.46	21.35	19.65	20.29	19.66	22.2	22.25	24.36	24.48	20	19.33	20.45	19.63	19.78	19.06	23.06	19.15
	Total training time (sec.)	725	1927	854	1356	1035	1514	1132	1513	1072	2228	800	1121	1145	1060	811	953	807	1915
	Best epoch	24	84	30	54	41	62	41	53	34	76	30	43	46	39	31	35	25	96
RSSCN7	Avg time/epoch (sec.)	3.19	6.97	4.68	6.74	3.9	3.76	7.09	6.9	7.59	8.5	3.79	3.65	5.54	5.52	4.3	4.08	5.23	5.43
	Total training time (sec.)	118	697	159	526	121	316	241	407	220	595	163	365	227	453	86	408	183	543
	Best epoch	27	85	24	63	21	69	24	44	19	55	33	93	31	67	10	100	25	87
WHU-RS19	Avg time/epoch (sec.)	2.78	2.53	3	4.79	2.85	3.85	4.02	4.29	4.04	4.04	2.76	2.78	3.4	3.44	2.84	3.86	3.2	3.03
	Total training time (sec.)	142	223	144	479	285	300	253	343	400	271	276	189	102	303	247	386	211	303
	Best epoch	41	73	38	96	96	63	53	65	89	52	100	53	20	73	77	89	56	90
SIRI-WHU	Avg time/epoch (sec.)	4.28	3.54	4.98	7.32	4.66	3.81	6.65	6.54	7.3	7.49	4.57	3.61	5.37	5.08	4.55	3.92	5.64	11.99
	Total training time (sec.)	197	326	214	732	191	305	226	608	365	749	329	238	322	503	150	392	203	1007
	Best epoch	36	77	33	93	31	65	24	78	40	94	62	51	50	84	23	98	26	69
RSI-CB256	Avg time/epoch (sec.)	34.84	34.99	34.04	34.9	33.69	36.39	51.9	51.86	56.6	56.75	33.5	26.5	41.18	41.08	35.29	29	40.35	36.93
	Total training time (sec.)	1568	2414	885	2757	1078	3166	1609	4472	2717	4029	1340	2123	1400	3204	1235	2900	1977	2622
	Best epoch	35	54	16	64	22	72	21	72	38	56	30	71	24	63	25	86	39	56
RESISC45	Avg time/epoch (sec.)	12.03	10.91	39.87	38.37	30.61	31.31	65.11	64.83	72.05	71.22	27.12	27.66	51.19	50.21	35.62	35.69	46.79	46.51
	Total training time (sec.)	385	633	1196	2993	1163	1941	2409	4084	3098	5484	678	2102	2713	2611	1033	1285	1778	2279
	Best epoch	22	43	20	63	28	47	27	48	33	62	15	61	43	37	19	21	28	34
PatternNet	Avg time/epoch (sec.)	15.17	13.75	37.74	37.47	29.1	35.65	62.94	69.05	68.87	71.08	25.86	27.54	48.5	49.05	33.8	34.54	45.93	45.06
	Total training time (sec.)	637	1141	1321	2061	1193	3030	1070	6905	3168	5260	569	2286	1067	3237	1521	2038	1378	4326
	Best epoch	32	68	25	40	31	70	7	88	36	59	12	68	12	51	35	44	20	81
CLRS	Avg time/epoch (sec.)	20.48	20.35	20.23	19.33	18.6	19.43	31.96	32.05	35.46	35.81	19.73	20.71	25.32	24.96	19.75	17.98	23.62	23.09
	Total training time (sec.)	635	2035	607	1450	279	1788	799	2373	993	2757	513	1512	785	1173	316	809	496	2309
	Best epoch	21	92	20	60	15	77	15	60	18	62	16	58	21	32	6	30	11	96
RSD46-WHU	Avg time/epoch (sec.)	58.03	58.84	158.32	162.89	123.27	127.53	269.45	272.7	297.7	301.16	111.55	113.93	210.37	211.93	148.25	148.42	196.2	194.93
	Total training time (sec.)	2031	3707	4433	8796	3205	8672	7814	19907	6847	15318	2231	6446	3997	9325	3558	4149	3924	11891
	Best epoch	25	48	18	39	16	53	19	58	13	36	10	40	9	29	14	12	10	46
SAT6	Avg time/epoch (sec.)	92.48	107.26	550.04	579.1	410.33	457.04	872.87	987.21	970.39	956.03	363	420.37	692.5	687.12	476.34	479.37	630.78	627.69
	Total training time (sec.)	5364	10726	29702	57910	37340	45704	61974	98721	55312	95603	8712	42037	42935	61841	15243	47937	42262	62769
	Best epoch	48	98	44	98	81	99	61	94	47	85	14	95	52	75	22	95	57	97
Optimaml31	Avg time/epoch (sec.)	1.1	1.23	2.97	4.81	2.58	2.6	4.62	5.92	5.02	5.16	2.25	2.36	3.71	3.79	2.82	3.26	3.5	3.59
	Total training time (sec.)	45	101	95	409	129	161	217	314	306	330	187	156	126	235	141	326	203	330
	Best epoch	31	67	22	70	40	47	37	38	51	49	73	51	24	47	40	98	48	77
BCS	Avg time/epoch (sec.)	1.48	1.53	4.17	5.95	3.45	4.55	6.61	7.95	7.33	7.31	3.17	3.26	5.07	5.55	3.94	4.47	5.08	5.09
	Total training time (sec.)	43	115	121	440	76	296	119	469	176	373	133	326	76	322	67	201	132	509
	Best epoch	19	60	19	59	12	50	8	44	14	36	32	98	5	43	7	30	16	95
So2Sat	Avg time/epoch (sec.)	158.09	174.74	716.09	723.72	565.55	558.79	1200.64	1198.37	1324.09	1325.67	510.45	499.21	925.09	926.5	643.91	651.31	853.91	851.06
	Total training time (sec.)	1790	3320	7877	13027	6221	10617	13207	22769	14784	23862	5615	11981	10176	14824	7278	10421	9393	15319
	Best epoch	1	4	1	3	1	4	1	4	1	3	1	9	1	1	1	1	1	3

Table B.9: Multi-Label classification tasks.

		AlexNet		VGG16		ResNet50		ResNet152		DenseNet161		EfficientNetB0		ConvNeXt		ViT		MLPMixer	
		Pt.	Sc.	Pt.	Sc.	Pt.	Sc.	Pt.	Sc.	Pt.	Sc.	Pt.	Sc.	Pt.	Sc.	Pt.	Sc.	Pt.	Sc.
AID	Avg time/epoch (sec.)	5.55	5.82	6.33	6.28	5.94	5.74	7.97	8.08	8.71	8.47	6.15	5.94	6.63	6.4	6.95	6.82	6.35	6.41
	Total training time (sec.)	172	524	190	490	190	379	239	477	366	449	381	398	345	576	146	627	165	506
	Best epoch	21	75	20	63	22	51	20	44	32	38	52	52	42	75	11	77	16	64
UCMerced	Avg time/epoch (sec.)	1.31	1.03	3.3	3.24	2.76	2.76	5.04	5.06	5.64	5.6	2.54	2.23	3.92	3.81	4.13	4.12	3.25	3.11
	Total training time (sec.)	71	103	132	324	124	276	227	506	468	487	254	252	259	381	132	412	182	311
	Best epoch	44	91	30	99	35	99	35	86	73	72	98	99	56	100	22	95	46	99
DFC15	Avg time/epoch (sec.)	7.74	7.83	8.94	8.5	8.49	8.92	9.45	9.66	9.54	9.89	8.33	8.47	8.72	8.8	8.76	8.85	8.18	8.31
	Total training time (sec.)	325	783	286	799	331	464	444	647	544	613	583	686	471	880	219	743	229	831
	Best epoch	32	99	22	79	29	37	37	52	47	47	60	66	44	91	15	69	18	100
MLRSNet	Avg time/epoch (sec.)	34.09	34.92	132.2	132.22	101.67	102.26	214.11	214.47	237.35	237.96	86.8	89.34	155.65	159.35	170.9	170.71	121.38	123.2
	Total training time (sec.)	1125	2549	3306	7272	1726	6238	5781	14155	6171	11422	2604	8934	3580	5896	3589	5975	1942	3080
	Best epoch	23	58	15	40	16	46	17	51	16	33	20	87	13	22	11	20	6	10
PlanetUAS	Avg time/epoch (sec.)	17.45	18.65	50.38	50.68	37	37.57	81.83	80.86	90.4	90.11	33.52	33.47	59.63	59.35	65.71	65.52	45.94	45.93
	Total training time (sec.)	576	1865	1058	2889	740	2592	1964	6792	1808	4866	771	2711	1431	5935	920	4128	735	2572
	Best epoch	23	87	11	42	10	54	14	69	10	39	13	66	14	90	4	48	6	41
BigEarthNet 19	Avg time/epoch (sec.)	90.43	84.18	537.9	544.28	413.24	409.87	874.56	878	976.93	982.63	366.35	364.13	631.67	645.51	698.5	709.86	488.68	500.77
	Total training time (sec.)	5245	5051	10758	15784	7025	18854	13993	32486	14654	29479	6228	11288	9475	26466	15367	20586	12217	15524
	Best epoch	48	45	10	14	7	31	6	22	5	15	7	16	5	26	12	14	15	16
BigEarthNet 43	Avg time/epoch (sec.)	89.85	86.78	542.3	542.24	414.18	413.89	881.69	875.2	969.67	975.34	365.4	359.16	642.81	643.66	702	702.53	492.84	495.88
	Total training time (sec.)	7188	5120	12473	18436	9112	26489	14107	43760	14545	31211	7308	11493	10285	24459	14742	21076	12321	15868
	Best epoch	70	44	13	19	12	49	6	35	5	17	10	17	6	23	11	15	15	17

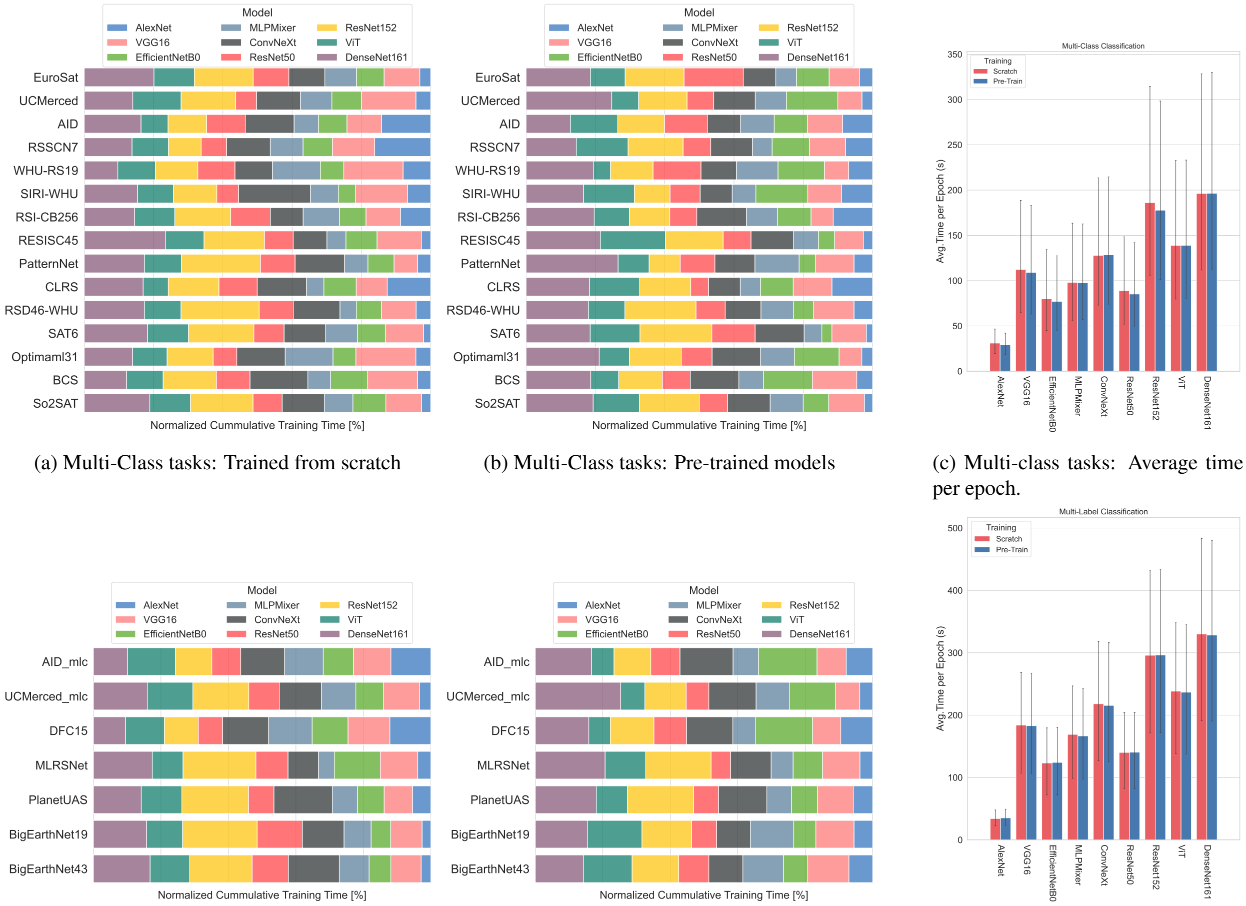

(a) Multi-Class tasks: Trained from scratch

(b) Multi-Class tasks: Pre-trained models

(c) Multi-class tasks: Average time per epoch.

(d) Multi-Label tasks: Trained from scratch

(e) Multi-Label tasks: Pre-trained models

(f) Multi-label tasks: Average time per epoch.

Figure B.5: **Total training time** of models trained from scratch and pre-trained models for each of the **(a,b)** MCC and **(d,e)** MLC datasts. The training time of each model architecture (denoted with different colors) is depicted as a fraction (%) of the cumulative training time for each dataset. Furthermore, (c) and (f) illustrate the average time per epoch of each model variant on **(c)** MCC and **(f)** MLC tasks, comparing the **(red)** pre-trained model variants (from (a) and (b)) to their counterparts **(blue)** trained from scratch.

C Detailed data descriptions & extended results

C.1 UC Merced

The UC Merced dataset [9] consists of 2100 images divided into 21 land-use scene classes. Each class has 100 RGB aerial image which are 256x256 pixels and have a spatial resolution of 0.3m per pixel. The images were manually extracted from large images from the United States Geological Survey (USGS) National Map of the following US regions: Birmingham, Boston, Buffalo, Columbus, Dallas, Harrisburg, Houston, Jacksonville, Las Vegas, Los Angeles, Miami, Napa, New York, Reno, San Diego, Santa Barbara, Seattle, Tampa, Tucson, and Ventura. Samples from the datasets can be seen on Figure C.6.

The 21 classes are: agricultural, airplane, baseball diamond, beach, buildings, chaparral, dense residential, forest, freeway, golf course, harbor, intersection, medium density residential, mobile home park, overpass, parking lot, river, runway, sparse residential, storage tanks, and tennis courts. The authors have not set predefined train-test splits, so we have made such for our study (Figure C.7).

The detailed results for all pre-trained models are shown on Table C.10 and for all the models learned from scratch are presented on Table C.11. The best performing model is the pre-trained ResNet152. The results on a class level are show on Table C.12 along with a confusion matrix on Figure C.8.

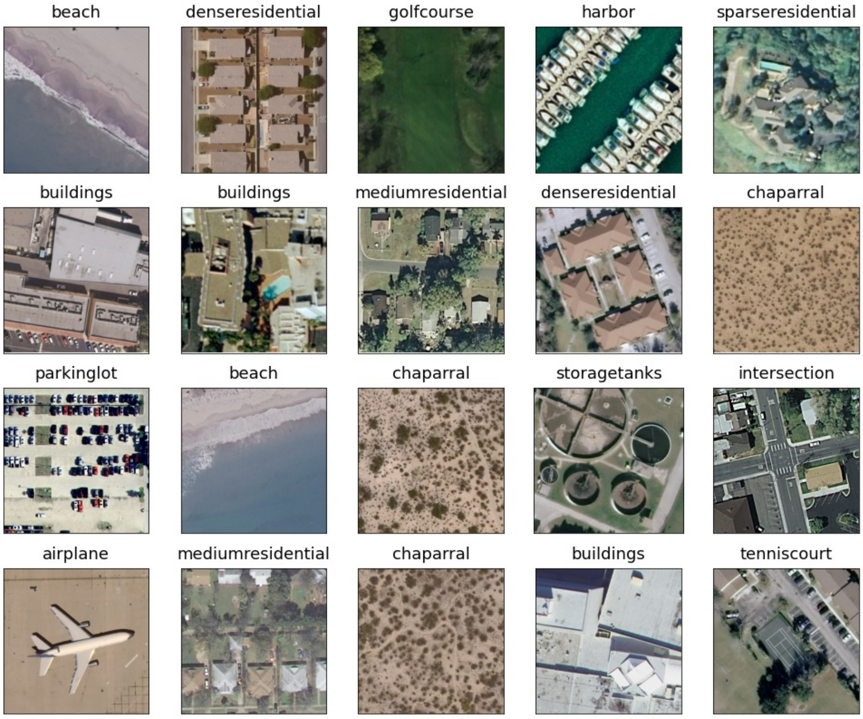

Figure C.6: Example images with labels from the UC Merced dataset.

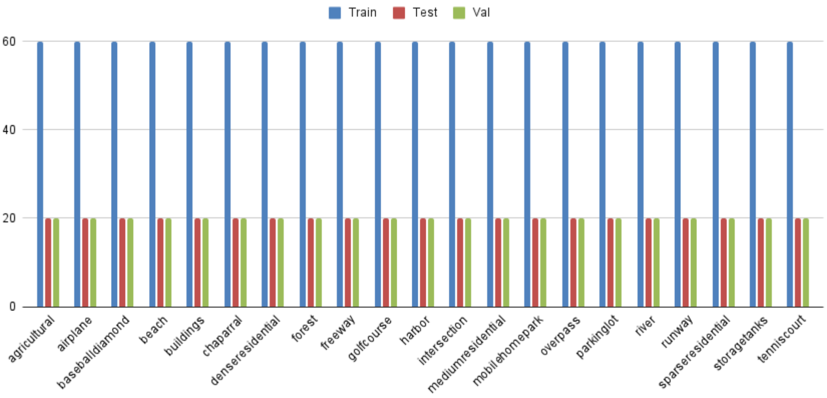

Figure C.7: Class distribution for the UC Merced dataset.

Table C.10: Detailed results for pre-trained models on UCMerced

Model \Metric	Accuracy	Macro Precision	Weighted Precision	Macro Recall	Weighted Recall	Macro F1 score	Weighted F1 score	Avg. time / epoch (sec.)	Total time (sec.)	Best epoch
AlexNet	92.14	92.24	92.24	92.14	92.14	92.03	92.03	1.29	44	24
VGG16	95.48	95.64	95.64	95.48	95.48	95.48	95.48	3.16	101	22
ResNet50	98.57	98.64	98.64	98.57	98.57	98.59	98.59	2.85	111	29
RestNet152	**98.81**	98.86	98.86	98.81	98.81	98.80	98.80	5.05	202	30
DenseNet161	98.33	98.40	98.40	98.33	98.33	98.34	98.34	5.41	357	56
EfficientNetB0	98.57	98.61	98.61	98.57	98.57	98.57	98.57	2.46	214	77
ConvNeXt	97.86	97.99	97.99	97.86	97.86	97.87	97.87	3.68	173	37
Vision Transformer	98.33	98.44	98.44	98.33	98.33	98.36	98.36	4.00	112	18
MLP Mixer	98.33	98.40	98.40	98.33	98.33	98.34	98.34	3.10	130	32

Table C.11: Detailed results for models trained from scratch on the UC Merced dataset.

Model \Metric	Accuracy	Macro Precision	Weighted Precision	Macro Recall	Weighted Recall	Macro F1 score	Weighted F1 score	Avg. time / epoch (sec.)	Total time (sec.)	Best epoch
AlexNet	81.19	81.30	81.30	81.19	81.19	80.87	80.87	1.30	126	82
VGG16	78.57	78.96	78.96	78.57	78.57	78.30	78.30	4.66	466	85
ResNet50	85.24	85.20	85.20	85.24	85.24	84.75	84.75	2.54	178	55
RestNet152	84.05	84.02	84.02	84.05	84.05	83.68	83.68	5.02	467	78
DenseNet161	**86.19**	86.42	86.42	86.19	86.19	85.75	85.75	5.46	415	61
EfficientNetB0	84.29	85.27	85.27	84.29	84.29	84.16	84.16	2.53	253	93
ConvNeXt	84.29	84.51	84.51	84.29	84.29	84.14	84.14	3.75	375	92
Vision Transformer	83.10	83.64	83.64	83.10	83.10	82.76	82.76	4.44	413	78
MLP Mixer	82.38	82.12	82.12	82.38	82.38	82.01	82.01	3.06	269	73

Table C.12: Per class results for the pre-trained ResNet152 model on the UC Merced dataset.

Label	Precision	Recall	F1 score
agricultural	100.00	100.00	100.00
airplane	100.00	100.00	100.00
baseballdiamond	100.00	100.00	100.00
beach	100.00	100.00	100.00
buildings	94.74	90.00	92.31
chaparral	100.00	100.00	100.00
denseresidential	90.91	100.00	95.24
forest	100.00	100.00	100.00
freeway	100.00	100.00	100.00
golfcourse	100.00	100.00	100.00
harbor	100.00	100.00	100.00
intersection	100.00	100.00	100.00
mediumresidential	100.00	90.00	94.74
mobilehomepark	100.00	95.00	97.44
overpass	100.00	100.00	100.00
parkinglot	100.00	100.00	100.00
river	100.00	100.00	100.00
runway	100.00	100.00	100.00
sparseresidential	95.24	100.00	97.56
storagetanks	95.24	100.00	97.56
tenniscourt	100.00	100.00	100.00

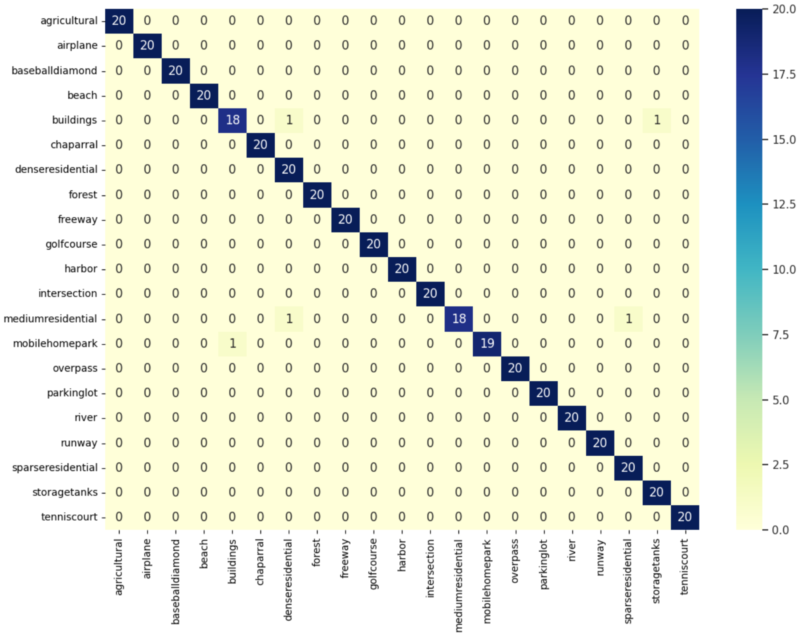

	agricultural	airplane	baseballdiamond	beach	buildings	chaparral	denseresidential	forest	freeway	golfcourse	harbor	intersection	mediumresidential	mobilehomepark	overpass	parkinglot	river	runway	sparseresidential	storagetanks	tenniscourt
agricultural	20	0	0	0	0	0	0	0	0	0	0	0	0	0	0	0	0	0	0	0	0
airplane	0	20	0	0	0	0	0	0	0	0	0	0	0	0	0	0	0	0	0	0	0
baseballdiamond	0	0	20	0	0	0	0	0	0	0	0	0	0	0	0	0	0	0	0	0	0
beach	0	0	0	20	0	0	0	0	0	0	0	0	0	0	0	0	0	0	0	0	0
buildings	0	0	0	0	18	0	1	0	0	0	0	0	0	0	0	0	0	0	0	1	0
chaparral	0	0	0	0	0	20	0	0	0	0	0	0	0	0	0	0	0	0	0	0	0
denseresidential	0	0	0	0	0	0	20	0	0	0	0	0	0	0	0	0	0	0	0	0	0
forest	0	0	0	0	0	0	0	20	0	0	0	0	0	0	0	0	0	0	0	0	0
freeway	0	0	0	0	0	0	0	0	20	0	0	0	0	0	0	0	0	0	0	0	0
golfcourse	0	0	0	0	0	0	0	0	0	20	0	0	0	0	0	0	0	0	0	0	0
harbor	0	0	0	0	0	0	0	0	0	0	20	0	0	0	0	0	0	0	0	0	0
intersection	0	0	0	0	0	0	0	0	0	0	0	20	0	0	0	0	0	0	0	0	0
mediumresidential	0	0	0	0	0	0	1	0	0	0	0	0	18	0	0	0	0	0	1	0	0
mobilehomepark	0	0	0	0	1	0	0	0	0	0	0	0	0	19	0	0	0	0	0	0	0
overpass	0	0	0	0	0	0	0	0	0	0	0	0	0	0	20	0	0	0	0	0	0
parkinglot	0	0	0	0	0	0	0	0	0	0	0	0	0	0	0	20	0	0	0	0	0
river	0	0	0	0	0	0	0	0	0	0	0	0	0	0	0	0	20	0	0	0	0
runway	0	0	0	0	0	0	0	0	0	0	0	0	0	0	0	0	0	20	0	0	0
sparseresidential	0	0	0	0	0	0	0	0	0	0	0	0	0	0	0	0	0	0	20	0	0
storagetanks	0	0	0	0	0	0	0	0	0	0	0	0	0	0	0	0	0	0	0	20	0
tenniscourt	0	0	0	0	0	0	0	0	0	0	0	0	0	0	0	0	0	0	0	0	20

Figure C.8: Confusion matrix for the pre-trained ResNet152 model on the UC Merced dataset.

C.2 WHU-RS19

WHU-RS19 is a set of satellite images exported from Google Earth, which provides high-resolution satellite images up to 0.5m and red, green and blue spectral bands [42]. It contains 19 classes of meaningful scenes in high-resolution satellite imagery, including: airport, beach, bridge, commercial area, desert, farmland, football field, forest, industrial area, meadow, mountain, park, parking lot, pond, port, railway station, residential area, river, and viaduct. For each class, there are about 50 samples with a total of 1005 images in the entire dataset. The data does not come with predefined train and test splits, so per standard we have made splits (Figure C.10).

The size of images is 600x600 pixel. The image samples of the same class are collected from different regions in satellite images of different resolutions and then might have different scales, orientations and illuminations. This makes the dataset challenging, however, the number of images is relatively small compared to the other datasets. Sample images from the dataset are shown in Figure C.9.

Detailed results for all pre-trained models are shown on Table C.13 and for all the models learned from scratch are presented on Table C.14. The best performing model is the pre-trained DenseNet161. The results on a class level are show on Table C.15 along with a confusion matrix on Figure C.11.

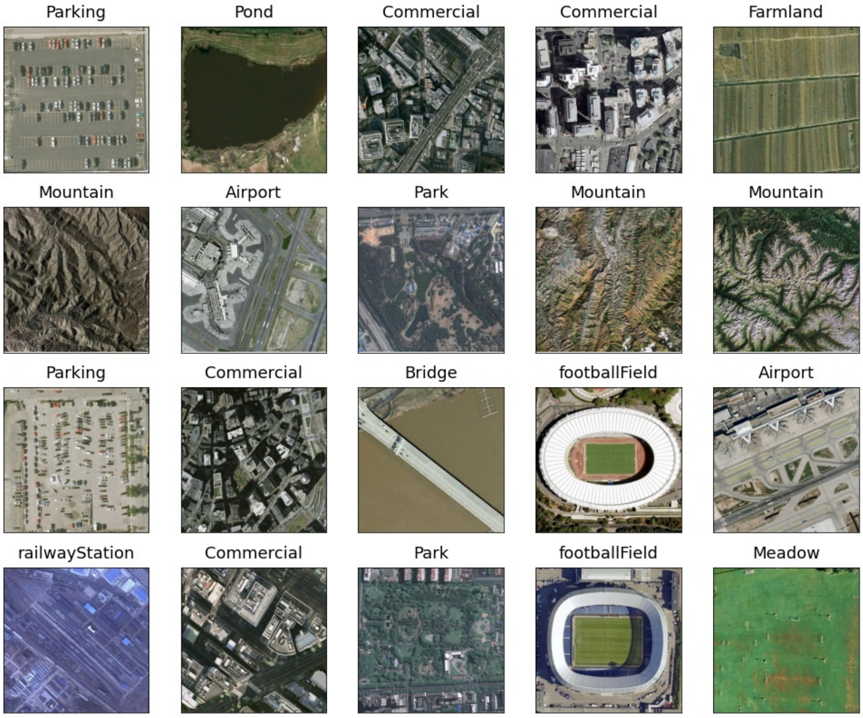

Figure C.9: Example images with labels from the WHU-RS19 dataset.

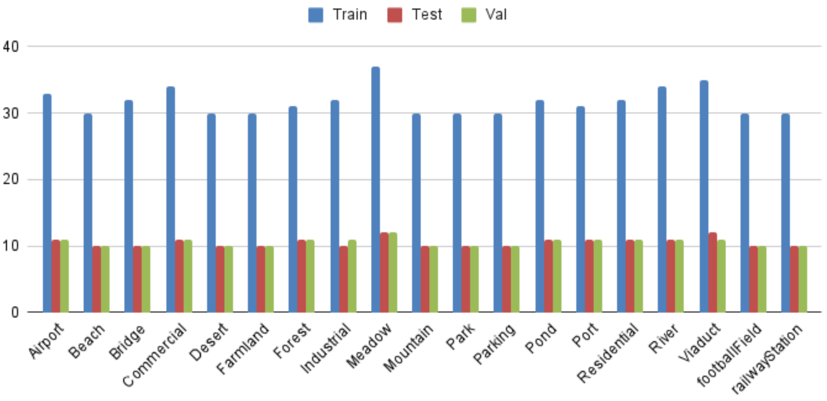

Figure C.10: Class distribution for the WHU-RS19 dataset.

Table C.13: Detailed results for pre-trained models the WHU-RS19 dataset.

Model \Metric	Accuracy	Macro Precision	Weighted Precision	Macro Recall	Weighted Recall	Macro F1 score	Weighted F1 score	Avg. time / epoch (sec.)	Total time (sec.)	Best epoch
AlexNet	93.53	94.44	94.30	93.63	93.53	93.73	93.59	2.78	142	41
VGG16	99.00	99.08	99.09	99.04	99.00	99.01	99.00	3.00	144	38
ResNet50	99.50	99.56	99.54	99.52	99.50	99.52	99.50	2.85	285	96
RestNet152	98.01	98.21	98.22	97.99	98.01	98.01	98.03	4.02	253	53
DenseNet161	**100.00**	100.00	100.00	100.00	100.00	100.00	100.00	4.04	400	89
EfficientNetB0	99.50	99.56	99.54	99.47	99.50	99.49	99.50	2.76	276	100
ConvNeXt	99.00	99.04	99.05	99.00	99.00	98.99	99.00	3.20	211	56
Vision Transformer	99.50	99.56	99.54	99.52	99.50	99.52	99.50	3.40	102	20
MLP Mixer	98.51	98.64	98.64	98.47	98.51	98.49	98.50	2.84	247	77

Table C.14: Detailed results for models trained from scratch the WHU-RS19 dataset.

Model \Metric	Accuracy	Macro Precision	Weighted Precision	Macro Recall	Weighted Recall	Macro F1 score	Weighted F1 score	Avg. time / epoch (sec.)	Total time (sec.)	Best epoch
AlexNet	66.17	67.93	67.68	66.28	66.17	66.53	66.36	2.53	223	73
VGG16	68.66	70.53	70.25	68.69	68.66	69.02	68.87	4.79	479	96
ResNet50	79.60	82.28	81.91	79.75	79.60	79.88	79.67	3.85	300	63
RestNet152	80.60	82.62	82.27	80.63	80.60	81.08	80.91	4.29	343	65
DenseNet161	**80.60**	82.75	82.44	80.59	80.60	80.75	80.60	4.04	271	52
EfficientNetB0	75.62	77.50	77.00	76.08	75.62	76.02	75.54	2.78	189	53
ConvNeXt	72.14	73.09	72.63	72.41	72.14	72.36	71.99	3.03	303	90
Vision Transformer	74.63	75.96	75.69	74.89	74.63	75.05	74.78	3.44	303	73
MLP Mixer	69.65	70.70	70.51	69.91	69.65	69.10	68.83	3.86	386	89

Table C.15: Per class results for the pre-trained DenseNet161 model on the WHU-RS19 dataset.

Label	Precision	Recall	F1 score
Airport	100.00	100.00	100.00
Beach	100.00	100.00	100.00
Bridge	100.00	100.00	100.00
Commercial	100.00	100.00	100.00
Desert	100.00	100.00	100.00
Farmland	100.00	100.00	100.00
footballField	100.00	100.00	100.00
Forest	100.00	100.00	100.00
Industrial	100.00	100.00	100.00
Meadow	100.00	100.00	100.00
Mountain	100.00	100.00	100.00
Park	100.00	100.00	100.00
Parking	100.00	100.00	100.00
Pond	100.00	100.00	100.00
Port	100.00	100.00	100.00
railwayStation	100.00	100.00	100.00
Residential	100.00	100.00	100.00
River	100.00	100.00	100.00
Viaduct	100.00	100.00	100.00

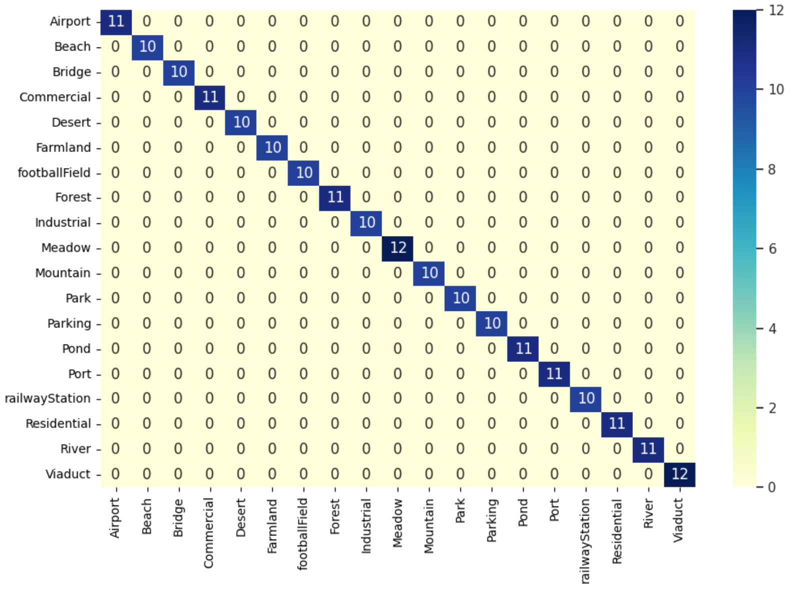

	Airport	Beach	Bridge	Commercial	Desert	Farmland	footballField	Forest	Industrial	Meadow	Mountain	Park	Parking	Pond	Port	railwayStation	Residential	River	Viaduct
Airport	11	0	0	0	0	0	0	0	0	0	0	0	0	0	0	0	0	0	0
Beach	0	10	0	0	0	0	0	0	0	0	0	0	0	0	0	0	0	0	0
Bridge	0	0	10	0	0	0	0	0	0	0	0	0	0	0	0	0	0	0	0
Commercial	0	0	0	11	0	0	0	0	0	0	0	0	0	0	0	0	0	0	0
Desert	0	0	0	0	10	0	0	0	0	0	0	0	0	0	0	0	0	0	0
Farmland	0	0	0	0	0	10	0	0	0	0	0	0	0	0	0	0	0	0	0
footballField	0	0	0	0	0	0	10	0	0	0	0	0	0	0	0	0	0	0	0
Forest	0	0	0	0	0	0	0	11	0	0	0	0	0	0	0	0	0	0	0
Industrial	0	0	0	0	0	0	0	0	10	0	0	0	0	0	0	0	0	0	0
Meadow	0	0	0	0	0	0	0	0	0	12	0	0	0	0	0	0	0	0	0
Mountain	0	0	0	0	0	0	0	0	0	0	10	0	0	0	0	0	0	0	0
Park	0	0	0	0	0	0	0	0	0	0	0	10	0	0	0	0	0	0	0
Parking	0	0	0	0	0	0	0	0	0	0	0	0	10	0	0	0	0	0	0
Pond	0	0	0	0	0	0	0	0	0	0	0	0	0	11	0	0	0	0	0
Port	0	0	0	0	0	0	0	0	0	0	0	0	0	0	11	0	0	0	0
railwayStation	0	0	0	0	0	0	0	0	0	0	0	0	0	0	0	10	0	0	0
Residential	0	0	0	0	0	0	0	0	0	0	0	0	0	0	0	0	11	0	0
River	0	0	0	0	0	0	0	0	0	0	0	0	0	0	0	0	0	11	0
Viaduct	0	0	0	0	0	0	0	0	0	0	0	0	0	0	0	0	0	0	12

Figure C.11: Confusion matrix for the pre-trained DenseNet161 model on the WHU-RS19 dataset.

C.3 AID

Aerial Image Dataset (AID) is a large-scale aerial image dataset generated by collecting sample images from Google Earth imagery. The goal of AID is to advance the state-of-the-art in scene classification of remote sensing images. For creating AID, more than ten thousands aerial scene images have been collected and annotated. It consists of 10000 RGB images with 600x600 pixels resolution (Figure C.12). The dataset is made up of the following 30 classes (aerial scene types): airport, bare land, baseball field, beach, bridge, center, church, commercial, dense residential, desert, farmland, forest, industrial, meadow, medium residential, mountain, park, parking, playground, pond, port, railway station, resort, river, school, sparse residential, square, stadium, storage tanks and viaduct.

All the images were labeled by the specialists in the field of remote sensing image interpretation. All samples from each class are chosen from different countries and regions around the world, but mainly in China, USA, England, France, Italy, Japan, Germany etc. They are extracted at different time and seasons under different image conditions. Although, all images have a 600x600 pixels resolution, their spatial resolution varies from 8 to 0.5 meters.

The dataset has no predefined train-test splits, so for properly conducting the study we have made train, test and validation splits. The distribution of the splits is presented on Figure C.13. Detailed results for all pre-trained models are shown on Table C.16 and for all the models learned from scratch are presented on Table C.17. The best performing model is the pre-trained ViT model. The results on a class level are show on Table C.18 along with a confusion matrix on Figure C.14.

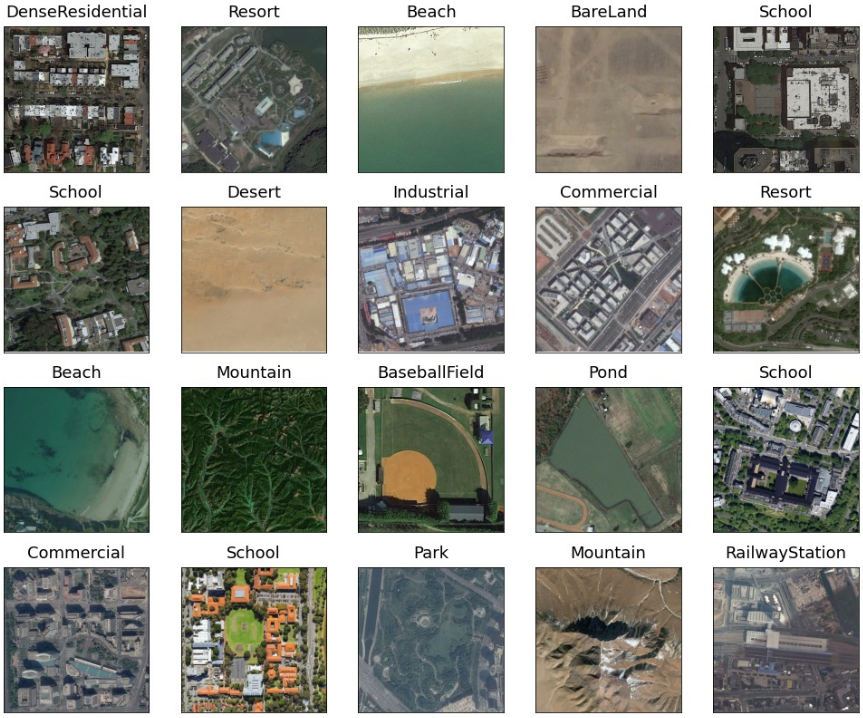

Figure C.12: Example images with labels from the AID dataset.

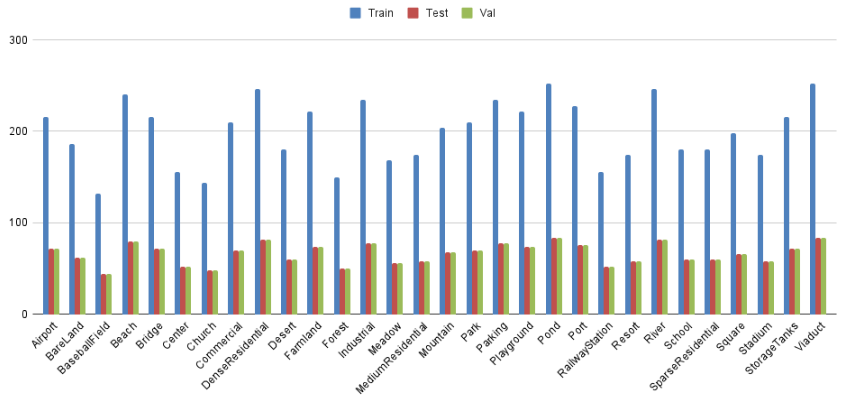

Figure C.13: Class distribution for the AID dataset.

Table C.16: Detailed results for pre-trained models on the AID dataset.

Model \Metric	Accuracy	Macro Precision	Weighted Precision	Macro Recall	Weighted Recall	Macro F1 score	Weighted F1 score	Avg. time / epoch (sec.)	Total time (sec.)	Best epoch
AlexNet	92.90	92.90	92.94	92.65	92.90	92.72	92.87	21.32	725	24
VGG16	96.10	95.95	96.11	95.91	96.10	95.90	96.08	21.35	854	30
ResNet50	96.55	96.48	96.56	96.26	96.55	96.30	96.50	20.29	1035	41
RestNet152	97.20	97.14	97.24	97.07	97.20	97.08	97.19	22.20	1132	41
DenseNet161	97.25	97.25	97.30	97.10	97.25	97.12	97.23	24.36	1072	34
EfficientNetB0	96.25	96.24	96.26	96.15	96.25	96.16	96.23	20.00	800	30
ConvNeXt	96.95	96.95	96.97	96.81	96.95	96.85	96.93	23.06	807	25
Vision Transformer	**97.75**	97.56	97.76	97.53	97.75	97.52	97.73	20.45	1145	46
MLP Mixer	96.70	96.58	96.74	96.52	96.70	96.51	96.69	19.78	811	31

Table C.17: Detailed results for models trained from scratch on the AID dataset.

Model \Metric	Accuracy	Macro Precision	Weighted Precision	Macro Recall	Weighted Recall	Macro F1 score	Weighted F1 score	Avg. time / epoch (sec.)	Total time (sec.)	Best epoch
AlexNet	81.35	81.23	81.32	81.14	81.35	81.07	81.23	19.46	1927	84
VGG16	81.95	81.80	82.04	81.52	81.95	81.50	81.84	19.65	1356	54
ResNet50	89.05	89.09	89.23	88.82	89.05	88.85	89.04	19.66	1514	62
RestNet152	89.90	90.08	90.09	89.60	89.90	89.73	89.88	22.25	1513	53
DenseNet161	**93.30**	93.32	93.42	93.13	93.30	93.17	93.30	24.48	2228	76
EfficientNetB0	90.05	90.19	90.32	89.88	90.05	89.92	90.08	19.33	1121	43
ConvNeXt	81.10	81.51	81.18	80.87	81.10	81.03	80.98	19.15	1915	96
Vision Transformer	79.35	79.27	79.27	79.51	79.35	79.30	79.21	19.63	1060	39
MLP Mixer	71.75	72.02	71.87	72.01	71.75	71.73	71.52	19.06	953	35

Table C.18: Per class results for the pre-trained Vision Transformer on the AID dataset.

Label	Precision	Recall	F1 score
Airport	98.61	98.61	98.61
BareLand	98.41	100.00	99.20
BaseballField	97.78	100.00	98.88
Beach	100.00	100.00	100.00
Bridge	100.00	100.00	100.00
Center	87.72	96.15	91.74
Church	93.48	89.58	91.49
Commercial	95.71	95.71	95.71
DenseResidential	98.80	100.00	99.39
Desert	100.00	100.00	100.00
Farmland	100.00	100.00	100.00
Forest	100.00	100.00	100.00
Industrial	94.94	96.15	95.54
Meadow	100.00	100.00	100.00
MediumResidential	98.28	98.28	98.28
Mountain	100.00	100.00	100.00
Park	94.44	97.14	95.77
Parking	100.00	100.00	100.00
Playground	98.63	97.30	97.96
Pond	98.81	98.81	98.81
Port	97.44	100.00	98.70
RailwayStation	96.23	98.08	97.14
Resort	94.12	82.76	88.07
River	98.80	100.00	99.39
School	91.38	88.33	89.83
SparseResidential	98.36	100.00	99.17
Square	98.44	95.45	96.92
Stadium	96.49	94.83	95.65
StorageTanks	100.00	100.00	100.00
Viaduct	100.00	98.81	99.40

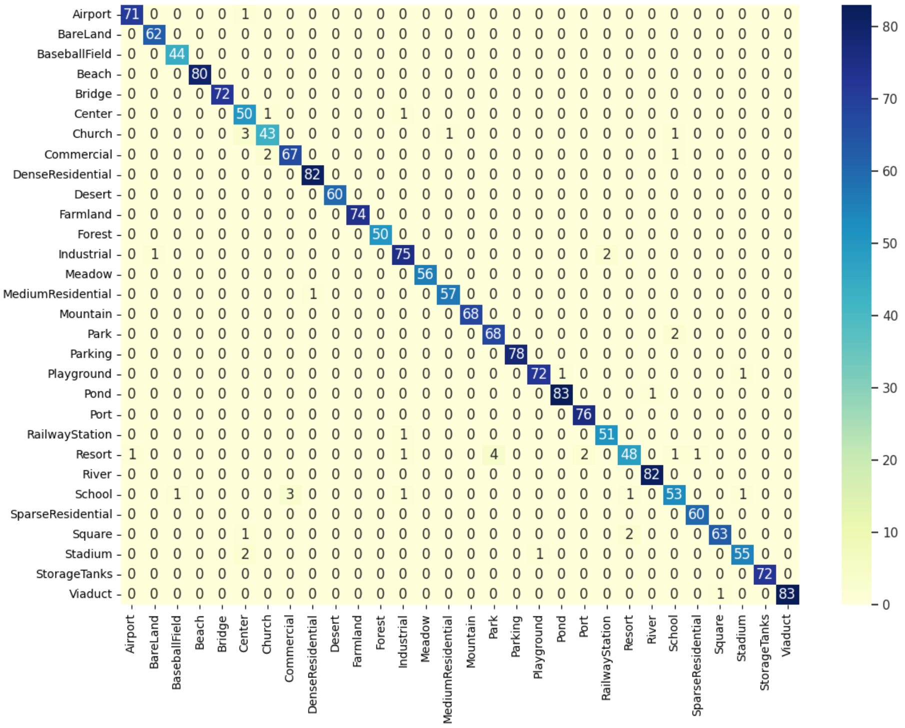

	Airport	BareLand	BaseballField	Beach	Bridge	Center	Church	Commercial	DenseResidential	Desert	Farmland	Forest	Industrial	Meadow	MediumResidential	Mountain	Park	Parking	Playground	Pond	Port	RailwayStation	Resort	River	School	SparseResidential	Square	Stadium	StorageTanks	Viaduct
Airport	71	0	0	0	0	1	0	0	0	0	0	0	0	0	0	0	0	0	0	0	0	0	0	0	0	0	0	0	0	0
BareLand	0	62	0	0	0	0	0	0	0	0	0	0	0	0	0	0	0	0	0	0	0	0	0	0	0	0	0	0	0	0
BaseballField	0	0	44	0	0	0	0	0	0	0	0	0	0	0	0	0	0	0	0	0	0	0	0	0	0	0	0	0	0	0
Beach	0	0	0	80	0	0	0	0	0	0	0	0	0	0	0	0	0	0	0	0	0	0	0	0	0	0	0	0	0	0
Bridge	0	0	0	0	72	0	0	0	0	0	0	0	0	0	0	0	0	0	0	0	0	0	0	0	0	0	0	0	0	0
Center	0	0	0	0	0	50	1	0	0	0	0	0	1	0	0	0	0	0	0	0	0	0	0	0	0	0	0	0	0	0
Church	0	0	0	0	0	3	43	0	0	0	0	0	0	0	1	0	0	0	0	0	0	0	0	0	1	0	0	0	0	0
Commercial	0	0	0	0	0	0	2	67	0	0	0	0	0	0	0	0	0	0	0	0	0	0	0	0	1	0	0	0	0	0
DenseResidential	0	0	0	0	0	0	0	0	82	0	0	0	0	0	0	0	0	0	0	0	0	0	0	0	0	0	0	0	0	0
Desert	0	0	0	0	0	0	0	0	0	60	0	0	0	0	0	0	0	0	0	0	0	0	0	0	0	0	0	0	0	0
Farmland	0	0	0	0	0	0	0	0	0	0	74	0	0	0	0	0	0	0	0	0	0	0	0	0	0	0	0	0	0	0
Forest	0	0	0	0	0	0	0	0	0	0	0	50	0	0	0	0	0	0	0	0	0	0	0	0	0	0	0	0	0	0
Industrial	0	1	0	0	0	0	0	0	0	0	0	0	75	0	0	0	0	0	0	0	0	2	0	0	0	0	0	0	0	0
Meadow	0	0	0	0	0	0	0	0	0	0	0	0	0	56	0	0	0	0	0	0	0	0	0	0	0	0	0	0	0	0
MediumResidential	0	0	0	0	0	0	0	0	1	0	0	0	0	0	57	0	0	0	0	0	0	0	0	0	0	0	0	0	0	0
Mountain	0	0	0	0	0	0	0	0	0	0	0	0	0	0	0	68	0	0	0	0	0	0	0	0	0	0	0	0	0	0
Park	0	0	0	0	0	0	0	0	0	0	0	0	0	0	0	0	68	0	0	0	0	0	0	0	2	0	0	0	0	0
Parking	0	0	0	0	0	0	0	0	0	0	0	0	0	0	0	0	0	78	0	0	0	0	0	0	0	0	0	0	0	0
Playground	0	0	0	0	0	0	0	0	0	0	0	0	0	0	0	0	0	0	72	1	0	0	0	0	0	0	0	1	0	0
Pond	0	0	0	0	0	0	0	0	0	0	0	0	0	0	0	0	0	0	0	83	0	0	0	1	0	0	0	0	0	0
Port	0	0	0	0	0	0	0	0	0	0	0	0	0	0	0	0	0	0	0	0	76	0	0	0	0	0	0	0	0	0
RailwayStation	0	0	0	0	0	0	0	0	0	0	0	0	1	0	0	0	0	0	0	0	0	51	0	0	0	0	0	0	0	0
Resort	1	0	0	0	0	0	0	0	0	0	0	0	1	0	0	0	4	0	0	0	2	0	48	0	1	1	0	0	0	0
River	0	0	0	0	0	0	0	0	0	0	0	0	0	0	0	0	0	0	0	0	0	0	0	82	0	0	0	0	0	0
School	0	0	1	0	0	0	0	3	0	0	0	0	1	0	0	0	0	0	0	0	0	0	1	0	53	0	0	1	0	0
SparseResidential	0	0	0	0	0	0	0	0	0	0	0	0	0	0	0	0	0	0	0	0	0	0	0	0	0	60	0	0	0	0
Square	0	0	0	0	0	1	0	0	0	0	0	0	0	0	0	0	0	0	0	0	0	0	2	0	0	0	63	0	0	0
Stadium	0	0	0	0	0	2	0	0	0	0	0	0	0	0	0	0	0	0	1	0	0	0	0	0	0	0	0	55	0	0
StorageTanks	0	0	0	0	0	0	0	0	0	0	0	0	0	0	0	0	0	0	0	0	0	0	0	0	0	0	0	0	72	0
Viaduct	0	0	0	0	0	0	0	0	0	0	0	0	0	0	0	0	0	0	0	0	0	0	0	0	0	0	1	0	0	83

Figure C.14: Confusion matrix for the pre-trained Vision Transformer model on the AID dataset.

C.4 Eurosat

EuroSAT [43] is a land use and land cover classification dataset based on Sentinel-2 satellite images covering 13 spectral bands and consisting out of 10 classes with in total 27000 labeled and geo-referenced images. The dataset provides RGB and multi-spectral (MS) version of the data. The spectral bands and their respective spatial resolutions are presented on Table C.19. The 10 image classes are the following: Annual Crop, Forest, Herbaceous Vegetation, Highway, Industrial, Pasture, Permanent Crop, Residential, River, Sea/Lake. Some samples from the dataset are presented on Figure C.15.The class distrubtion of our train, test and validation splits are provided on Figure C.16.

Detailed results for all pre-trained models are shown on Table C.20 and for all the models learned from scratch are presented on Table C.21. The best performing model is the pre-trained ResNet152 model. The results on a class level are show on Table C.22 along with a confusion matrix on Figure C.17.

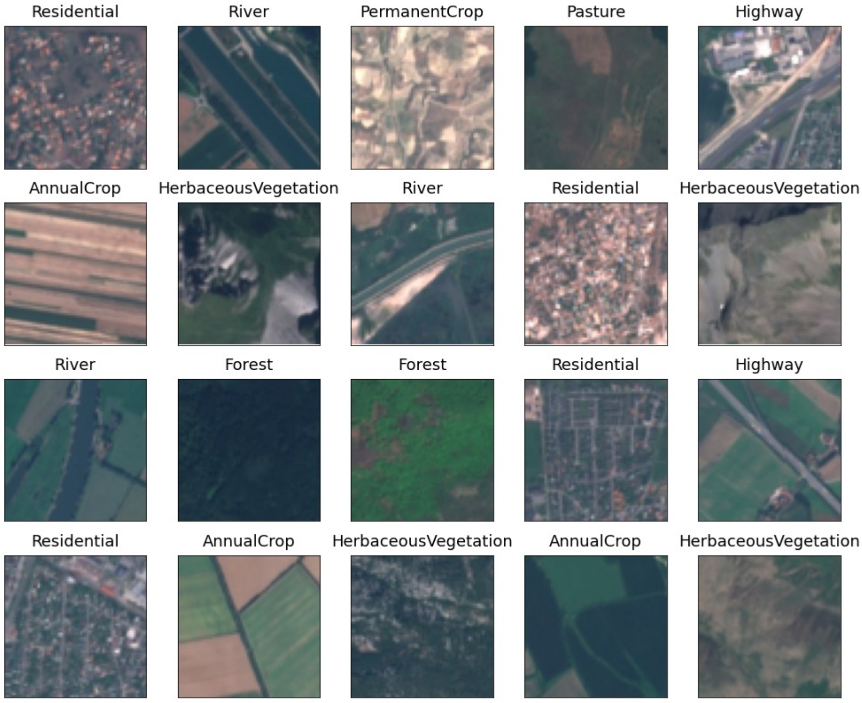

Figure C.15: Example images with labels from the Eurosat dataset.

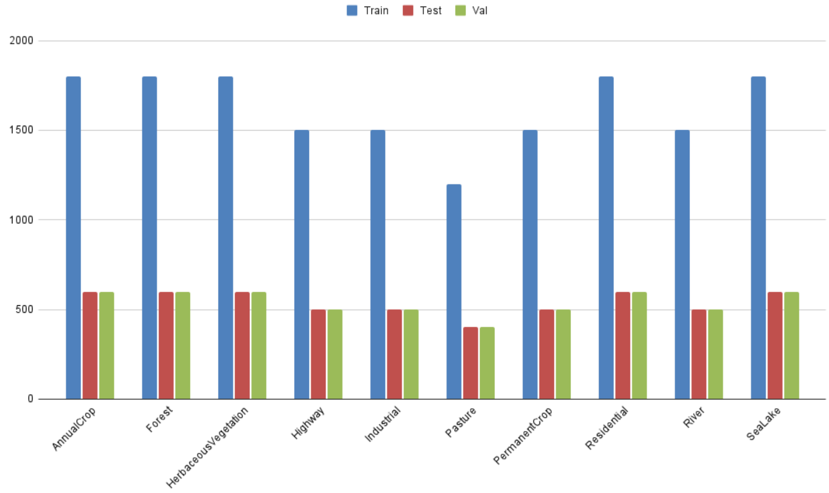

Figure C.16: Class distribution for the Eurosat dataset.

Table C.19: Eurosat bands and spatial resolutions.

Band	**Spatial resolution *m***
B01 - Aerosols	60
B02 - Blue	10
B03 - Green	10
B04 - Red	10
B05 - Red edge 1	20
B06 - Red edge 2	20
B07 - Red edge 3	20
B08 - NIR	10
B08A - Red edge 4	20
B09 - Water vapor	60
B10 - Cirrus	60
B11 - SWIR 1	20
B12 - SWIR 2	20

Table C.20: Detailed results for pre-trained models on the Eurosat dataset.

Model \Metric	Accuracy	Macro Precision	Weighted Precision	Macro Recall	Weighted Recall	Macro F1 score	Weighted F1 score	Avg. time / epoch (sec.)	Total time (sec.)	Best epoch
AlexNet	97.57	97.48	97.58	97.48	97.57	97.48	97.57	8.88	426	38
VGG16	98.15	98.14	98.15	98.06	98.15	98.09	98.15	33.69	977	19
ResNet50	98.83	98.82	98.83	98.77	98.83	98.79	98.83	26.56	1912	62
RestNet152	**99.00**	99.00	99.00	98.96	99.00	98.98	99.00	56.00	1904	24
DenseNet161	98.89	98.88	98.89	98.82	98.89	98.85	98.89	61.12	2078	24
EfficientNetB0	98.91	98.91	98.91	98.86	98.91	98.88	98.91	23.47	1056	35
ConvNeXt	98.78	98.76	98.78	98.75	98.78	98.75	98.78	40.38	1050	16
Vision Transformer	98.72	98.71	98.73	98.64	98.72	98.68	98.72	43.19	1123	16
MLP Mixer	98.74	98.73	98.74	98.65	98.74	98.68	98.74	30.41	669	12

Table C.21: Detailed results for models trained from scratch on the Eurosat dataset.

Model \Metric	Accuracy	Macro Precision	Weighted Precision	Macro Recall	Weighted Recall	Macro F1 score	Weighted F1 score	Avg. time / epoch (sec.)	Total time (sec.)	Best epoch
AlexNet	96.17	96.02	96.18	96.10	96.17	96.06	96.17	8.02	802	95
VGG16	97.19	97.17	97.19	97.04	97.19	97.10	97.18	33.62	2622	63
ResNet50	97.00	96.93	97.01	96.85	97.00	96.88	97.00	26.45	2619	84
RestNet152	97.41	97.36	97.41	97.27	97.41	97.31	97.40	56.21	4328	62
DenseNet161	97.63	97.57	97.64	97.51	97.63	97.54	97.63	62.50	5125	67
EfficientNetB0	**97.80**	97.76	97.80	97.72	97.80	97.74	97.79	24.19	2032	69
ConvNeXt	95.43	95.25	95.44	95.29	95.43	95.27	95.43	40.03	2642	51
Vision Transformer	95.04	94.86	95.02	94.80	95.04	94.82	95.02	44.22	2963	52
MLP Mixer	95.50	95.29	95.50	95.35	95.50	95.31	95.49	31.45	2327	59

Table C.22: Per class results for the pre-trained ResNet152 model on the Eurosat dataset.

Label	Precision	Recall	F1 score
Annual Crop	98.66	98.33	98.50
Forest	99.17	99.50	99.33
Herbaceous Vegetation	98.01	98.67	98.34
Highway	99.20	98.80	99.00
Industrial	99.40	99.00	99.20
Pasture	98.74	98.25	98.50
Permanent Crop	98.59	97.60	98.09
Residential	99.50	100.00	99.75
River	99.20	99.60	99.40
Sea Lake	99.50	99.83	99.67

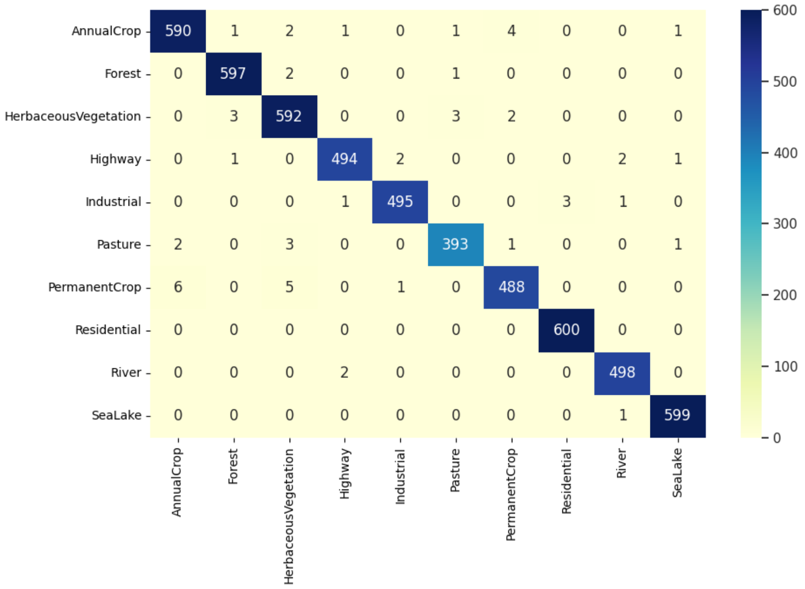

Figure C.17: Confusion matrix for the pre-trained ResNet152 model on the Eurosat dataset.

C.5 PatternNet

PatternNet is a large-scale remote sensing dataset that was collected specifically for Remote sensing image retrieval. It contains 38 classes: airplane, baseball field, basketball court, beach, bridge, cemetery, chaparral, christmas tree farm, closed road, coastal mansion, crosswalk, dense residential, ferry terminal, football field, forest, freeway, golf course, harbor, intersection, mobile home park, nursing home, oil gas field, oil well, overpass, parking lot, parking space, railway, river, runway, runway marking, shipping yard, solar panel, sparse residential, storage tank, swimming pool, tennis court, transformer station and wastewater treatment plant. There are a total of 38 classes with 800 images of size 256×256 pixels for each class. The class distribution of the train, test and validation splits we generated is presented on Figure C.19, since the dataset does not have predefined ones.

PatternNet dataset has the following main characteristics: It's the largest publicly available dataset specifically designed for remote sensing image retrieval. It has a higher spatial resolution, so that the classes of interest constitute a larger portion of the image. It has high inter-class similarity and high intra-class diversity. Some sample images are shown on Figure C.18.

Detailed results for all pre-trained models are shown on Table C.23 and for all the models learned from scratch are presented on Table C.24. The best performing models are the pre-trained DenseNet161 and ResNet50 models. The results on a class level are show on Table C.25 along with a confusion matrix on Figure C.20.

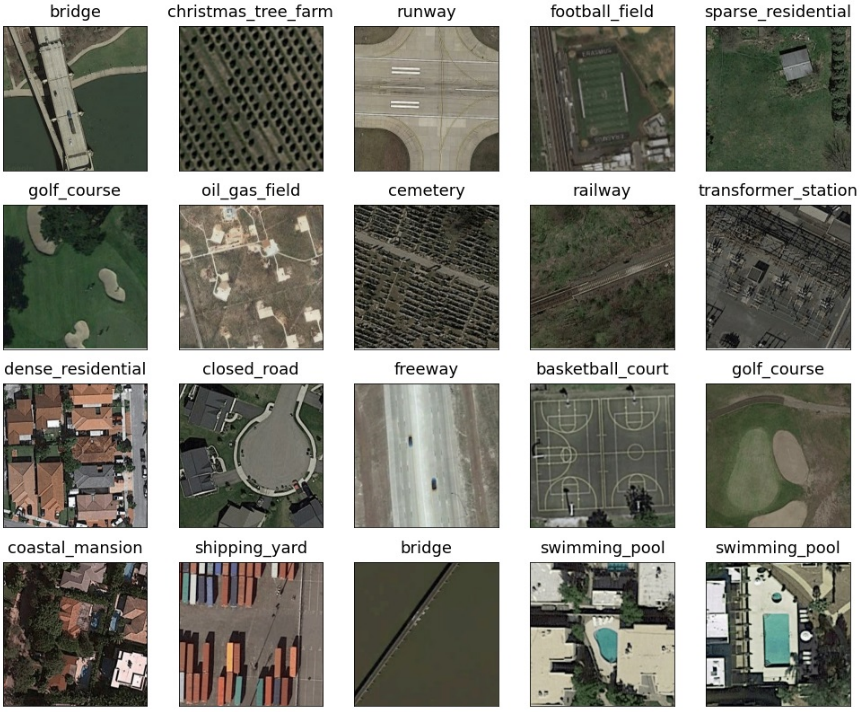

Figure C.18: Example images with labels from the PatternNet dataset.

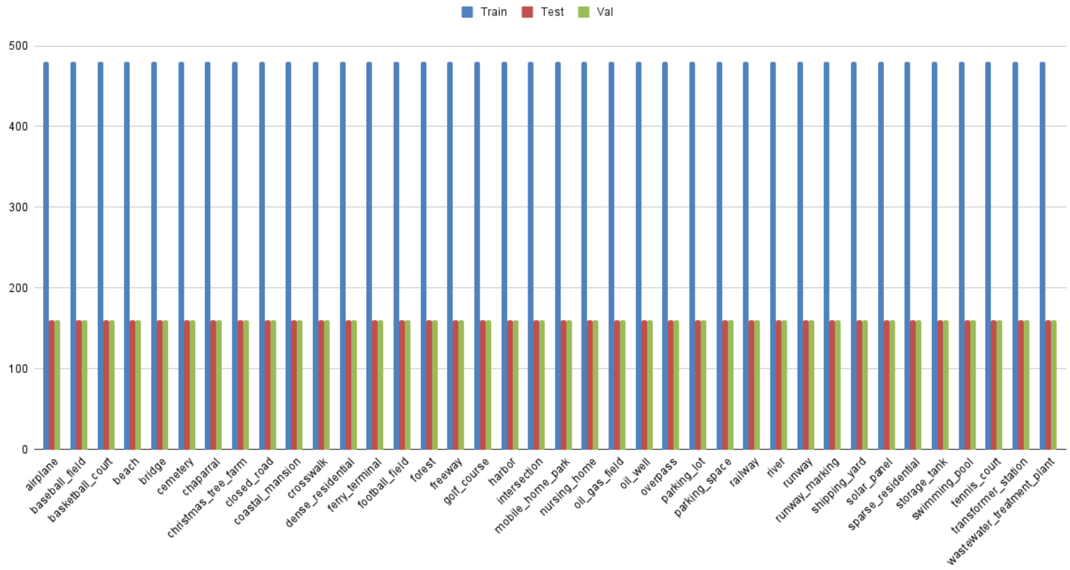

Figure C.19: Class distribution for the PatternNet dataset.

Table C.23: Detailed results for pre-trained models on the PatternNet dataset.

Model \Metric	Accuracy	Macro Precision	Weighted Precision	Macro Recall	Weighted Recall	Macro F1 score	Weighted F1 score	Avg. time / epoch (sec.)	Total time (sec.)	Best epoch
AlexNet	99.16	99.17	99.17	99.16	99.16	99.16	99.16	15.17	637	32
VGG16	99.42	99.43	99.43	99.42	99.42	99.42	99.42	37.74	1321	25
ResNet50	**99.74**	99.74	99.74	99.74	99.74	99.74	99.74	29.10	1193	31
RestNet152	99.49	99.49	99.49	99.49	99.49	99.49	99.49	62.94	1070	7
DenseNet161	**99.74**	99.74	99.74	99.74	99.74	99.74	99.74	68.87	3168	36
EfficientNetB0	99.54	99.54	99.54	99.54	99.54	99.54	99.54	25.86	569	12
ConvNeXt	99.67	99.67	99.67	99.67	99.67	99.67	99.67	45.93	1378	20
Vision Transformer	99.65	99.66	99.66	99.65	99.65	99.65	99.65	48.50	1067	12
MLP Mixer	99.70	99.71	99.71	99.70	99.70	99.70	99.70	33.80	1521	35

Table C.24: Detailed results for models trained from scratch on the PatternNet dataset.

Model \Metric	Accuracy	Macro Precision	Weighted Precision	Macro Recall	Weighted Recall	Macro F1 score	Weighted F1 score	Avg. time / epoch (sec.)	Total time (sec.)	Best epoch
AlexNet	97.83	97.83	97.83	97.83	97.83	97.82	97.82	13.75	1141	68
VGG16	97.91	97.93	97.93	97.91	97.91	97.91	97.91	37.47	2061	40
ResNet50	99.06	99.07	99.07	99.06	99.06	99.06	99.06	35.65	3030	70
RestNet152	98.88	98.89	98.89	98.88	98.88	98.88	98.88	69.05	6905	88
DenseNet161	**99.24**	99.25	99.25	99.24	99.24	99.24	99.24	71.08	5260	59
EfficientNetB0	98.83	98.84	98.84	98.83	98.83	98.83	98.83	27.54	2286	68
ConvNeXt	97.83	97.83	97.83	97.83	97.83	97.82	97.82	45.06	4326	81
Vision Transformer	96.69	96.69	96.69	96.69	96.69	96.68	96.68	49.05	3237	51
MLP Mixer	98.83	98.84	98.84	98.83	98.83	98.83	98.83	34.54	2038	44

Table C.25: Per class results for the pre-trained DenseNet161 model on the PatternNet dataset.

Label	Precision	Recall	F1 score
airplane	100.00	100.00	100.00
baseball field	100.00	100.00	100.00
basketball court	99.37	98.75	99.06
beach	100.00	100.00	100.00
bridge	98.77	100.00	99.38
cemetery	100.00	100.00	100.00
chaparral	100.00	100.00	100.00
christmas tree farm	100.00	100.00	100.00
closed_road	99.38	100.00	99.69
coastal_mansion	98.73	97.50	98.11
crosswalk	100.00	100.00	100.00
dense_residential	100.00	100.00	100.00
ferry terminal	100.00	98.75	99.37
football field	100.00	100.00	100.00
forest	100.00	100.00	100.00
freeway	100.00	100.00	100.00
golf course	100.00	100.00	100.00
harbor	100.00	100.00	100.00
intersection	99.38	100.00	99.69
mobile home park	100.00	100.00	100.00
nursing home	100.00	99.38	99.69
oil gas field	100.00	100.00	100.00
oil well	100.00	100.00	100.00
overpass	100.00	100.00	100.00
parking lot	100.00	100.00	100.00
parking space	100.00	100.00	100.00
railway	100.00	100.00	100.00
river	100.00	100.00	100.00
runway	100.00	99.38	99.69
runway marking	99.38	100.00	99.69
shipping yard	100.00	100.00	100.00
solar panel	100.00	100.00	100.00
sparse residential	96.91	98.13	97.52
storage tank	99.38	99.38	99.38
swimming pool	100.00	100.00	100.00
tennis court	100.00	99.38	99.69
transformer station	99.38	100.00	99.69
wastewater treatment plant	99.38	99.38	99.38

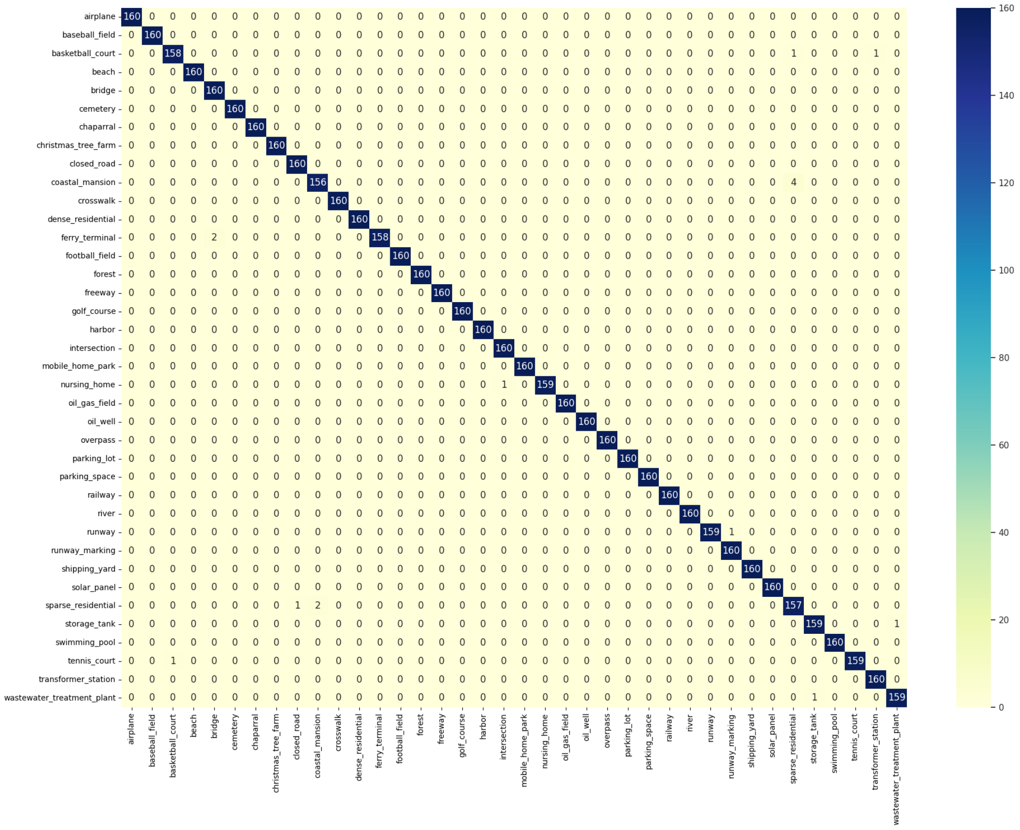

	airplane	baseball_field	basketball_court	beach	bridge	cemetery	chaparral	christmas_tree_farm	closed_road	coastal_mansion	crosswalk	dense_residential	ferry_terminal	football_field	forest	freeway	golf_course	harbor	intersection	mobile_home_park	nursing_home	oil_gas_field	oil_well	overpass	parking_lot	parking_space	railway	river	runway	runway_marking	shipping_yard	solar_panel	sparse_residential	storage_tank	swimming_pool	tennis_court	transformer_station	wastewater_treatment_plant
airplane	160	0	0	0	0	0	0	0	0	0	0	0	0	0	0	0	0	0	0	0	0	0	0	0	0	0	0	0	0	0	0	0	0	0	0	0	0	0
baseball_field	0	160	0	0	0	0	0	0	0	0	0	0	0	0	0	0	0	0	0	0	0	0	0	0	0	0	0	0	0	0	0	0	0	0	0	0	0	0
basketball_court	0	0	158	0	0	0	0	0	0	0	0	0	0	0	0	0	0	0	0	0	0	0	0	0	0	0	0	0	0	0	0	0	1	0	0	0	1	0
beach	0	0	0	160	0	0	0	0	0	0	0	0	0	0	0	0	0	0	0	0	0	0	0	0	0	0	0	0	0	0	0	0	0	0	0	0	0	0
bridge	0	0	0	0	160	0	0	0	0	0	0	0	0	0	0	0	0	0	0	0	0	0	0	0	0	0	0	0	0	0	0	0	0	0	0	0	0	0
cemetery	0	0	0	0	0	160	0	0	0	0	0	0	0	0	0	0	0	0	0	0	0	0	0	0	0	0	0	0	0	0	0	0	0	0	0	0	0	0
chaparral	0	0	0	0	0	0	160	0	0	0	0	0	0	0	0	0	0	0	0	0	0	0	0	0	0	0	0	0	0	0	0	0	0	0	0	0	0	0
christmas_tree_farm	0	0	0	0	0	0	0	160	0	0	0	0	0	0	0	0	0	0	0	0	0	0	0	0	0	0	0	0	0	0	0	0	0	0	0	0	0	0
closed_road	0	0	0	0	0	0	0	0	160	0	0	0	0	0	0	0	0	0	0	0	0	0	0	0	0	0	0	0	0	0	0	0	0	0	0	0	0	0
coastal_mansion	0	0	0	0	0	0	0	0	0	156	0	0	0	0	0	0	0	0	0	0	0	0	0	0	0	0	0	0	0	0	0	0	4	0	0	0	0	0
crosswalk	0	0	0	0	0	0	0	0	0	0	160	0	0	0	0	0	0	0	0	0	0	0	0	0	0	0	0	0	0	0	0	0	0	0	0	0	0	0
dense_residential	0	0	0	0	0	0	0	0	0	0	0	160	0	0	0	0	0	0	0	0	0	0	0	0	0	0	0	0	0	0	0	0	0	0	0	0	0	0
ferry_terminal	0	0	0	0	2	0	0	0	0	0	0	0	158	0	0	0	0	0	0	0	0	0	0	0	0	0	0	0	0	0	0	0	0	0	0	0	0	0
football_field	0	0	0	0	0	0	0	0	0	0	0	0	0	160	0	0	0	0	0	0	0	0	0	0	0	0	0	0	0	0	0	0	0	0	0	0	0	0
forest	0	0	0	0	0	0	0	0	0	0	0	0	0	0	160	0	0	0	0	0	0	0	0	0	0	0	0	0	0	0	0	0	0	0	0	0	0	0
freeway	0	0	0	0	0	0	0	0	0	0	0	0	0	0	0	160	0	0	0	0	0	0	0	0	0	0	0	0	0	0	0	0	0	0	0	0	0	0
golf_course	0	0	0	0	0	0	0	0	0	0	0	0	0	0	0	0	160	0	0	0	0	0	0	0	0	0	0	0	0	0	0	0	0	0	0	0	0	0
harbor	0	0	0	0	0	0	0	0	0	0	0	0	0	0	0	0	0	160	0	0	0	0	0	0	0	0	0	0	0	0	0	0	0	0	0	0	0	0
intersection	0	0	0	0	0	0	0	0	0	0	0	0	0	0	0	0	0	0	160	0	0	0	0	0	0	0	0	0	0	0	0	0	0	0	0	0	0	0
mobile_home_park	0	0	0	0	0	0	0	0	0	0	0	0	0	0	0	0	0	0	0	160	0	0	0	0	0	0	0	0	0	0	0	0	0	0	0	0	0	0
nursing_home	0	0	0	0	0	0	0	0	0	0	0	0	0	0	0	0	0	0	1	0	159	0	0	0	0	0	0	0	0	0	0	0	0	0	0	0	0	0
oil_gas_field	0	0	0	0	0	0	0	0	0	0	0	0	0	0	0	0	0	0	0	0	0	160	0	0	0	0	0	0	0	0	0	0	0	0	0	0	0	0
oil_well	0	0	0	0	0	0	0	0	0	0	0	0	0	0	0	0	0	0	0	0	0	0	160	0	0	0	0	0	0	0	0	0	0	0	0	0	0	0
overpass	0	0	0	0	0	0	0	0	0	0	0	0	0	0	0	0	0	0	0	0	0	0	0	160	0	0	0	0	0	0	0	0	0	0	0	0	0	0
parking_lot	0	0	0	0	0	0	0	0	0	0	0	0	0	0	0	0	0	0	0	0	0	0	0	0	160	0	0	0	0	0	0	0	0	0	0	0	0	0
parking_space	0	0	0	0	0	0	0	0	0	0	0	0	0	0	0	0	0	0	0	0	0	0	0	0	0	160	0	0	0	0	0	0	0	0	0	0	0	0
railway	0	0	0	0	0	0	0	0	0	0	0	0	0	0	0	0	0	0	0	0	0	0	0	0	0	0	160	0	0	0	0	0	0	0	0	0	0	0
river	0	0	0	0	0	0	0	0	0	0	0	0	0	0	0	0	0	0	0	0	0	0	0	0	0	0	0	160	0	0	0	0	0	0	0	0	0	0
runway	0	0	0	0	0	0	0	0	0	0	0	0	0	0	0	0	0	0	0	0	0	0	0	0	0	0	0	0	159	1	0	0	0	0	0	0	0	0
runway_marking	0	0	0	0	0	0	0	0	0	0	0	0	0	0	0	0	0	0	0	0	0	0	0	0	0	0	0	0	0	160	0	0	0	0	0	0	0	0
shipping_yard	0	0	0	0	0	0	0	0	0	0	0	0	0	0	0	0	0	0	0	0	0	0	0	0	0	0	0	0	0	0	160	0	0	0	0	0	0	0
solar_panel	0	0	0	0	0	0	0	0	0	0	0	0	0	0	0	0	0	0	0	0	0	0	0	0	0	0	0	0	0	0	0	160	0	0	0	0	0	0
sparse_residential	0	0	0	0	0	0	0	0	1	2	0	0	0	0	0	0	0	0	0	0	0	0	0	0	0	0	0	0	0	0	0	0	157	0	0	0	0	0
storage_tank	0	0	0	0	0	0	0	0	0	0	0	0	0	0	0	0	0	0	0	0	0	0	0	0	0	0	0	0	0	0	0	0	0	159	0	0	0	1
swimming_pool	0	0	0	0	0	0	0	0	0	0	0	0	0	0	0	0	0	0	0	0	0	0	0	0	0	0	0	0	0	0	0	0	0	0	160	0	0	0
tennis_court	0	0	1	0	0	0	0	0	0	0	0	0	0	0	0	0	0	0	0	0	0	0	0	0	0	0	0	0	0	0	0	0	0	0	0	159	0	0
transformer_station	0	0	0	0	0	0	0	0	0	0	0	0	0	0	0	0	0	0	0	0	0	0	0	0	0	0	0	0	0	0	0	0	0	0	0	0	160	0
wastewater_treatment_plant	0	0	0	0	0	0	0	0	0	0	0	0	0	0	0	0	0	0	0	0	0	0	0	0	0	0	0	0	0	0	0	0	0	1	0	0	0	159

Figure C.20: Confusion matrix for the pre-trained DenseNet161 model on the PatternNet dataset.

C.6 Resisc45

RESISC45 [76] dataset is a publicly available benchmark for Remote Sensing Image Scene Classification (RESISC), created by Northwestern Polytechnical University (NWPU). This dataset contains 31500 images, covering 45 scene classes with 700 images in each class. The 45 scene classes are as follows: airplane, airport, baseball diamond, basketball court, beach, bridge, chaparral, church, circular farmland, cloud, commercial area, dense residential, desert, forest, freeway, golf course, ground track field, harbor, industrial area, intersection, island, lake, meadow, medium residential, mobile home park, mountain, overpass, palace, parking lot, railway, railway station, rectangular farmland, river, roundabout, runway, sea ice, ship, snowberg, sparse residential, stadium, storage tank, tennis court, terrace, thermal power station, and wetland. Accordingly, these classes contain a variety of spatial patterns, some homogeneous with respect to texture, some homogeneous with respect to color, others not homogeneous at all.

The images are with a size of 256x256 pixels in the RGB color space. The spatial resolution varies from about 30m to 0.2m per pixel for most of the scene classes except for the classes of island, lake, mountain, and snowberg that have lower spatial resolutions. The 31500 images cover more than 100 countries and regions all over the world, including developing, transition, and highly developed economies (Figure C.21). Our generated train, test and validation splits distribution is show on Figure C.22.

Detailed results for all pre-trained models are shown on Table C.26 and for all the models learned from scratch are presented on Table C.27. The best performing model is the pre-trained Vision Transformer model. The results on a class level are show on Table C.28 along with a confusion matrix on Figure C.23.

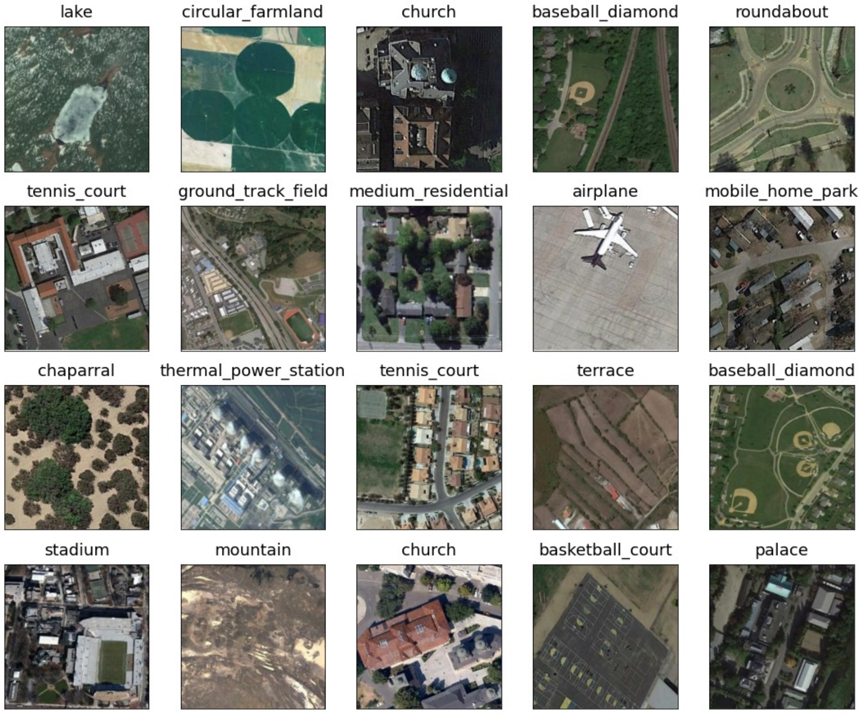

Figure C.21: Example images with labels from the Resisc45 dataset.

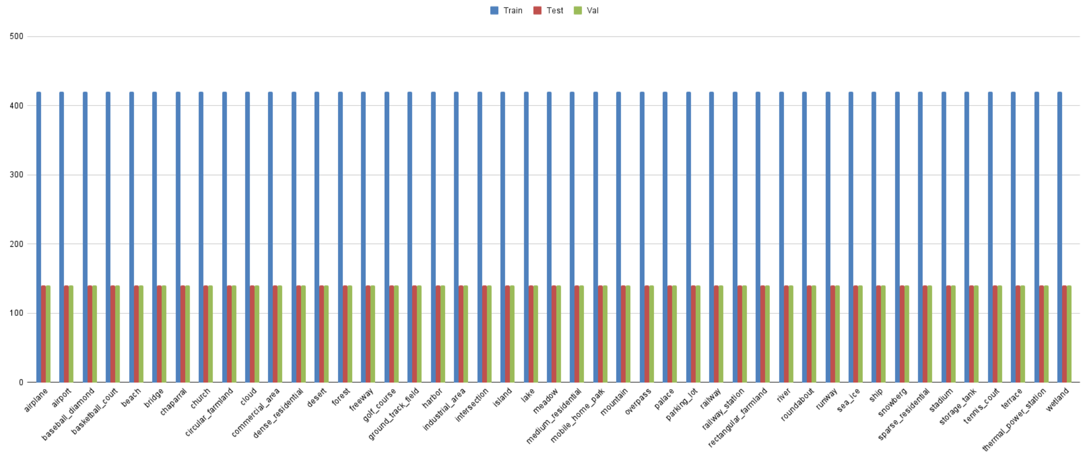

Figure C.22: Class distribution for the Resisc45 dataset.

Table C.26: Detailed results for pre-trained models on the Resisc45 dataset.

Model \Metric	Accuracy	Macro Precision	Weighted Precision	Macro Recall	Weighted Recall	Macro F1 score	Weighted F1 score	Avg. time / epoch (sec.)	Total time (sec.)	Best epoch
AlexNet	90.49	90.56	90.56	90.49	90.49	90.49	90.49	12.03	385	22
VGG16	93.90	93.91	93.91	93.90	93.90	93.89	93.89	39.87	1196	20
ResNet50	96.46	96.50	96.50	96.46	96.46	96.46	96.46	30.61	1163	28
RestNet152	96.54	96.57	96.57	96.54	96.54	96.54	96.54	65.11	2409	27
DenseNet161	96.51	96.53	96.53	96.51	96.51	96.51	96.51	72.05	3098	33
EfficientNetB0	94.87	94.93	94.93	94.87	94.87	94.88	94.88	27.12	678	15
ConvNeXt	96.27	96.28	96.28	96.27	96.27	96.26	96.26	46.79	1778	28
Vision Transformer	**97.08**	97.10	97.10	97.08	97.08	97.07	97.07	51.19	2713	43
MLP Mixer	95.95	95.99	95.99	95.95	95.95	95.96	95.96	35.62	1033	19

Table C.27: Detailed results for models trained from scratch on the Resisc45 dataset.

Model \Metric	Accuracy	Macro Precision	Weighted Precision	Macro Recall	Weighted Recall	Macro F1 score	Weighted F1 score	Avg. time / epoch (sec.)	Total time (sec.)	Best epoch
AlexNet	82.16	82.29	82.29	82.16	82.16	82.10	82.10	10.91	633	43
VGG16	83.89	84.00	84.00	83.89	83.89	83.84	83.84	38.37	2993	63
ResNet50	92.33	92.40	92.40	92.33	92.33	92.33	92.33	31.31	1941	47
RestNet152	90.68	90.79	90.79	90.68	90.68	90.69	90.69	64.83	4084	48
DenseNet161	**93.46**	93.50	93.50	93.46	93.46	93.46	93.46	71.22	5484	62
EfficientNetB0	91.37	91.47	91.47	91.37	91.37	91.38	91.38	27.66	2102	61
ConvNeXt	85.94	86.30	86.30	85.94	85.94	86.05	86.05	46.51	2279	34
Vision Transformer	81.02	81.18	81.18	81.02	81.02	80.98	80.98	50.21	2611	37
MLP Mixer	69.41	69.67	69.67	69.41	69.41	69.22	69.22	35.69	1285	21

Table C.28: Per class results for the pre-trained Vision Transformer model on the Resisc45 dataset,

Label	Precision	Recall	F1 score
airplane	99.28	98.57	98.92
airport	95.89	100.00	97.90
baseball_diamond	97.89	99.29	98.58
basketball_court	97.22	100.00	98.59
beach	98.59	100.00	99.29
bridge	97.87	98.57	98.22
chaparral	97.90	100.00	98.94
church	90.85	92.14	91.49
circular_farmland	98.59	100.00	99.29
cloud	100.00	99.29	99.64
commercial_area	95.07	96.43	95.74
dense_residential	94.20	92.86	93.53
desert	97.86	97.86	97.86
forest	97.79	95.00	96.38
freeway	99.27	97.14	98.19
golf_course	98.58	99.29	98.93
ground_track_field	100.00	99.29	99.64
harbor	100.00	100.00	100.00
industrial_area	94.96	94.29	94.62
intersection	97.86	97.86	97.86
island	98.59	100.00	99.29
lake	93.75	96.43	95.07
meadow	95.00	95.00	95.00
medium_residential	91.61	93.57	92.58
mobile_home_park	97.22	100.00	98.59
mountain	95.74	96.43	96.09
overpass	99.25	94.29	96.70
palace	91.91	89.29	90.58
parking_lot	99.28	98.57	98.92
railway	93.84	97.86	95.80
railway_station	96.30	92.86	94.55
rectangular_farmland	91.95	97.86	94.81
river	99.24	92.86	95.94
roundabout	99.29	100.00	99.64
runway	100.00	95.71	97.81
sea_ice	100.00	98.57	99.28
ship	97.22	100.00	98.59
snowberg	98.59	100.00	99.29
sparse_residential	96.43	96.43	96.43
stadium	97.90	100.00	98.94
storage_tank	98.56	97.86	98.21
tennis_court	98.54	96.43	97.47
terrace	96.21	90.71	93.38
thermal_power_station	96.45	97.14	96.80
wetland	97.01	92.86	94.89

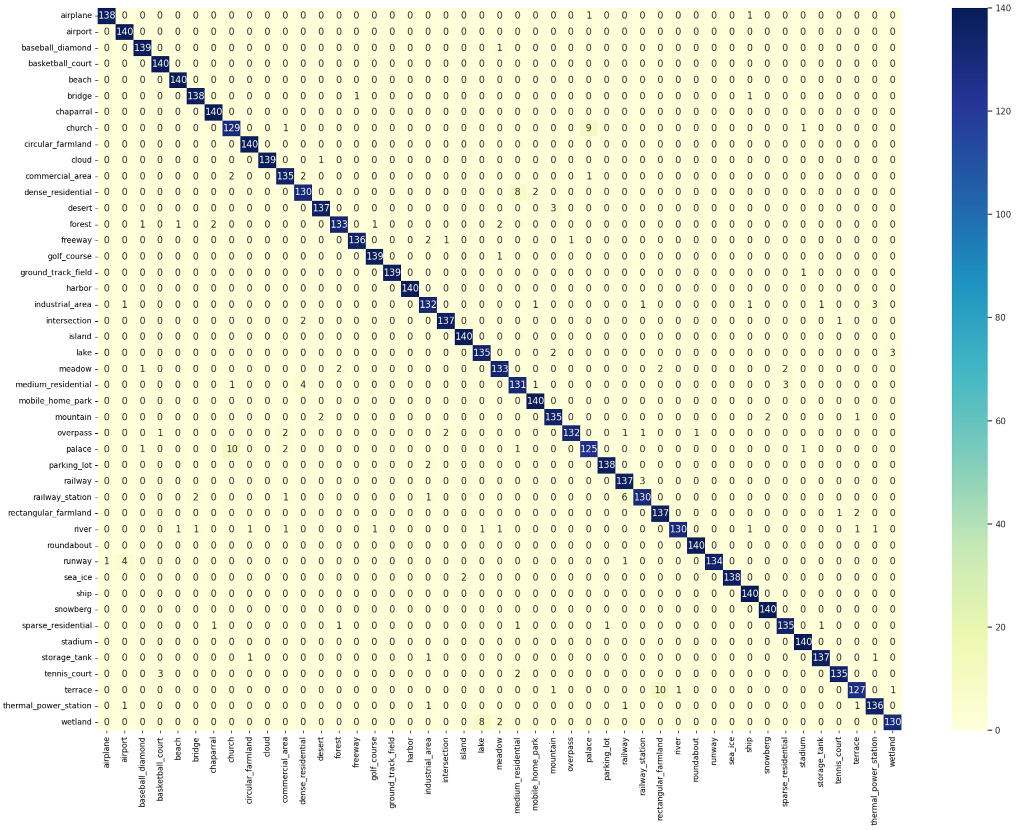

Figure C.23: Confusion matrix for the pre-trained Vision Transformer model on the Resisc45 dataset.

C.7 RSI-CB256

RSI-CB256 [46] is a large scale remote sensing image classification benchmark via crowdsource data such as Open Street Map (OSM) data, ground objects in remote sensing images etc. It contains 35 categories and more than 24000 images with a size of 256x256 pixels (Figure C.24). A strict object category system according to the national standard of land-use classification in China and the hierarchical grading mechanism of ImageNet-1K has been established. Using crowd-source data as a supervisor facilitates machine self-learning through the Internet. The class distribution of the train, test and validation splits is presented in Figure C.25.

Detailed results for all pre-trained models are shown on Table C.29 and for all the models learned from scratch are presented on Table C.30. The best performing model is the pre-trained ResNet152 model. The results on a class level are show on Table C.31 along with a confusion matrix on Figure C.26.

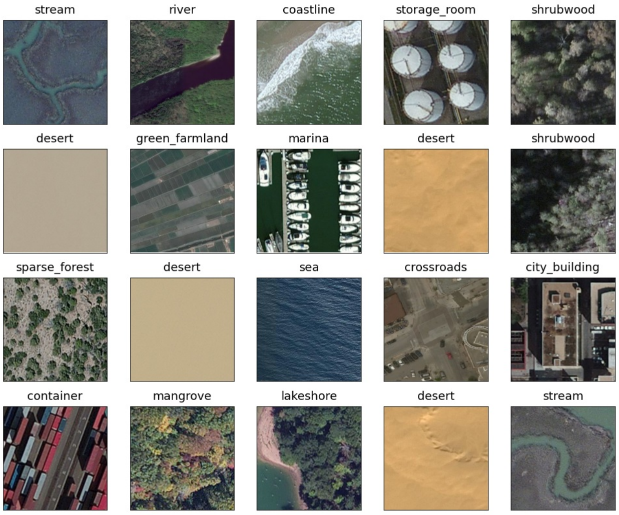

Figure C.24: Example images with labels from the RSI-CB256 dataset.

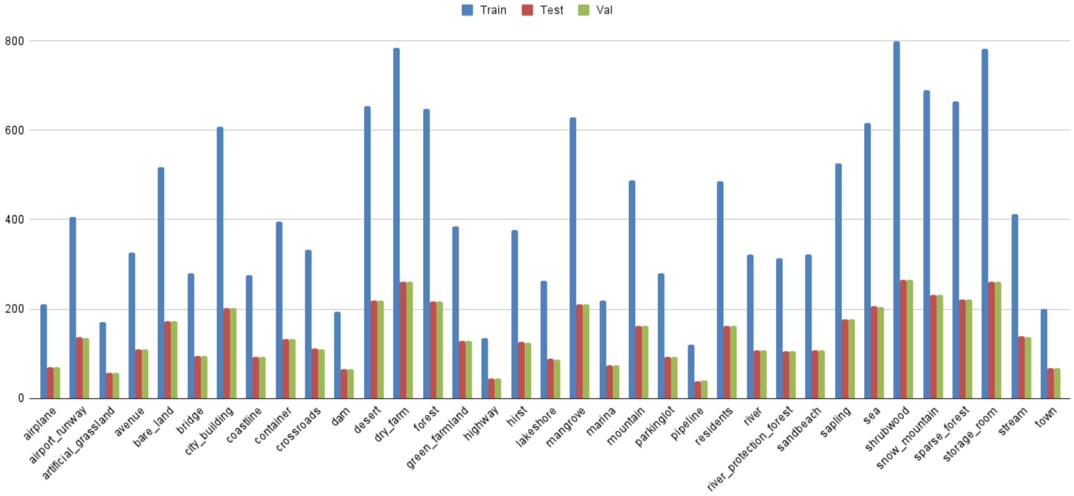

Figure C.25: Class distribution for the RSI-CB526 dataset.

Table C.29: Detailed results for pre-trained models on the RSI-CB256 dataset.

Model \Metric	Accuracy	Macro Precision	Weighted Precision	Macro Recall	Weighted Recall	Macro F1 score	Weighted F1 score	Avg. time / epoch (sec.)	Total time (sec.)	Best epoch
AlexNet	99.35	99.13	99.36	99.06	99.35	99.09	99.35	34.84	1568	35
VGG16	99.05	98.93	99.07	98.75	99.05	98.83	99.05	34.04	885	16
ResNet50	99.68	99.53	99.68	99.54	99.68	99.53	99.68	33.69	1078	22
RestNet152	**99.86**	99.85	99.86	99.82	99.86	99.83	99.86	51.90	1609	21
DenseNet161	99.74	99.68	99.74	99.64	99.74	99.66	99.74	56.60	2717	38
EfficientNetB0	99.72	99.63	99.72	99.65	99.72	99.64	99.72	33.50	1340	30
ConvNeXt	99.60	99.50	99.60	99.55	99.60	99.52	99.60	40.35	1977	39
Vision Transformer	99.76	99.75	99.76	99.71	99.76	99.73	99.76	41.18	1400	24
MLP Mixer	99.66	99.54	99.66	99.61	99.66	99.57	99.66	35.29	1235	25

Table C.30: Detailed results for models trained from scratch on the RSI-CB256 dataset.

Model \Metric	Accuracy	Macro Precision	Weighted Precision	Macro Recall	Weighted Recall	Macro F1 score	Weighted F1 score	Avg. time / epoch (sec.)	Total time (sec.)	Best epoch
AlexNet	97.35	96.55	97.39	96.54	97.35	96.51	97.35	34.99	2414	54
VGG16	98.83	98.51	98.84	98.36	98.83	98.43	98.83	34.90	2757	64
ResNet50	98.83	98.51	98.84	98.36	98.83	98.43	98.83	36.39	3166	72
RestNet152	**99.15**	98.98	99.15	98.81	99.15	98.89	99.15	51.86	4472	72
DenseNet161	99.13	98.80	99.13	98.71	99.13	98.75	99.13	56.75	4029	56
EfficientNetB0	99.11	98.85	99.12	98.91	99.11	98.87	99.11	26.50	2123	71
ConvNeXt	98.44	97.75	98.45	97.74	98.44	97.73	98.44	36.93	2622	56
Vision Transformer	98.12	97.52	98.13	97.12	98.12	97.31	98.12	41.08	3204	63
MLP Mixer	98.42	97.81	98.43	97.80	98.42	97.79	98.42	29.00	2900	86

Table C.31: Per class results for the pre-trained ResNet152 model on the RSI-CB256 dataset.

Label	Precision	Recall	F1 score
airplane	100.00	100.00	100.00
airport_runway	100.00	100.00	100.00
artificial_grassland	100.00	100.00	100.00
avenue	100.00	99.08	99.54
bare_land	98.30	100.00	99.14
bridge	98.95	100.00	99.47
city_building	100.00	100.00	100.00
coastline	100.00	98.91	99.45
container	100.00	99.24	99.62
crossroads	99.11	100.00	99.55
dam	100.00	100.00	100.00
desert	100.00	98.62	99.31
dry_farm	100.00	100.00	100.00
forest	100.00	100.00	100.00
green_farmland	100.00	100.00	100.00
highway	100.00	97.73	98.85
hirst	100.00	100.00	100.00
lakeshore	100.00	100.00	100.00
mangrove	100.00	100.00	100.00
marina	100.00	100.00	100.00
mountain	100.00	100.00	100.00
parkinglot	98.94	100.00	99.47
pipeline	100.00	100.00	100.00
residents	100.00	100.00	100.00
river	100.00	100.00	100.00
river_protection_forest	100.00	100.00	100.00
sandbeach	100.00	100.00	100.00
sapling	100.00	100.00	100.00
sea	99.52	100.00	99.76
shrubwood	100.00	100.00	100.00
snow_mountain	100.00	100.00	100.00
sparse_forest	100.00	100.00	100.00
storage_room	100.00	100.00	100.00
stream	100.00	100.00	100.00
town	100.00	100.00	100.00

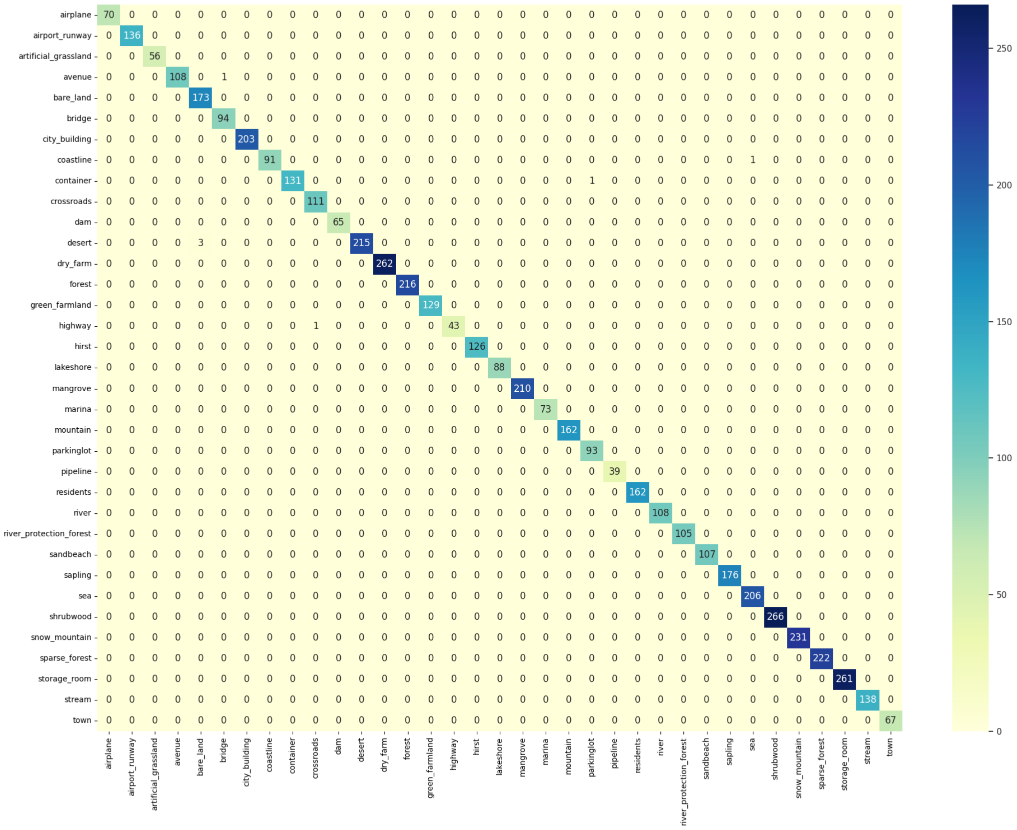

Figure C.26: Confusion matrix for the pre-trained ResNet152 model on the RSI-CB256 dataset.

C.8 RSSCN7

RSSCN7 [47] is a scene classification dataset. The images are obtained from Google Earth. This dataset was collected for academic research. It contains a total of 2800 remote sensing images, which are organized into 7 scene classes: grass land, forest, farm land, parking lot, residential region, industrial region, and river/lake (Figure C.27). For each, class there are 400 RGB images that are cropped on four different scales with 100 images per scale. Each image has a 400x400 pixels size. The main challenge of this dataset is the scale variations of the images. The class distribution over the train, test and validation splits is presented on Figure C.28.

Detailed results for all pre-trained models are shown on Table C.32 and for all the models learned from scratch are presented on Table C.33. The best performing model is the pre-trained Vision Transformer model. The results on a class level are show on Table C.34 along with a confusion matrix on Figure C.29.

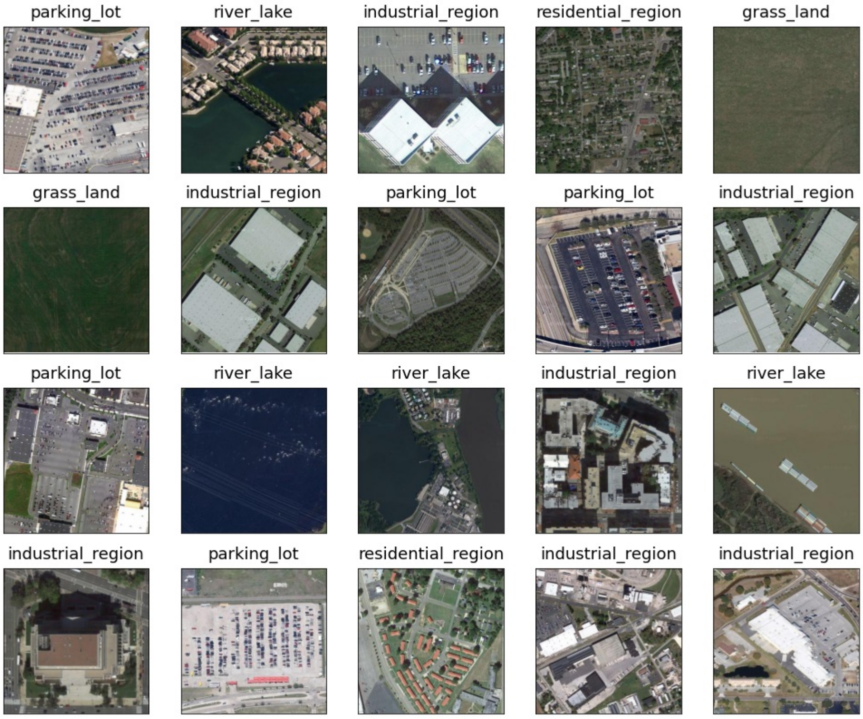

Figure C.27: Example images with labels from the RSSCN7 dataset.

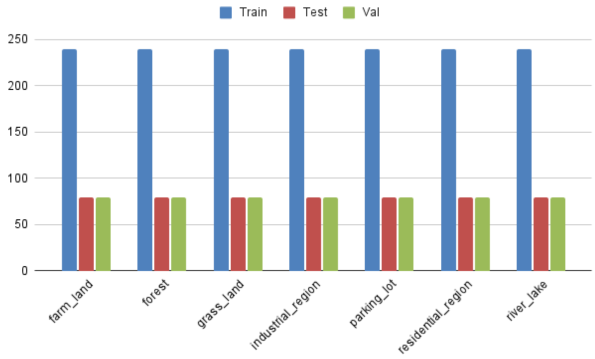

Figure C.28: Class distribution for the RSSCN7 dataset.

Table C.32: Detailed results for pre-trained models on the RSSCN7 dataset.

Model \Metric	Accuracy	Macro Precision	Weighted Precision	Macro Recall	Weighted Recall	Macro F1 score	Weighted F1 score	Avg. time / epoch (sec.)	Total time (sec.)	Best epoch
AlexNet	91.96	92.05	92.05	91.96	91.96	91.92	91.92	3.19	118	27
VGG16	93.93	93.95	93.95	93.93	93.93	93.90	93.90	4.68	159	24
ResNet50	95.00	95.08	95.08	95.00	95.00	94.99	94.99	3.90	121	21
RestNet152	95.00	95.07	95.07	95.00	95.00	95.01	95.01	7.09	241	24
DenseNet161	94.82	94.83	94.83	94.82	94.82	94.82	94.82	7.59	220	19
EfficientNetB0	95.54	95.56	95.56	95.54	95.54	95.54	95.54	3.79	163	33
ConvNeXt	94.64	94.76	94.76	94.64	94.64	94.61	94.61	5.23	183	25
Vision Transformer	**95.89**	95.95	95.95	95.89	95.89	95.91	95.91	5.54	227	31
MLP Mixer	95.18	95.23	95.23	95.18	95.18	95.17	95.17	4.30	86	10

Table C.33: Detailed results for models trained from scratch on the RSSCN7 dataset.

Model \Metric	Accuracy	Macro Precision	Weighted Precision	Macro Recall	Weighted Recall	Macro F1 score	Weighted F1 score	Avg. time / epoch (sec.)	Total time (sec.)	Best epoch
AlexNet	80.54	80.64	80.64	80.54	80.54	80.45	80.45	6.97	697	85
VGG16	81.61	81.50	81.50	81.61	81.61	81.41	81.41	6.74	526	63
ResNet50	82.68	82.65	82.65	82.68	82.68	82.41	82.41	3.76	316	69
RestNet152	82.68	82.65	82.65	82.68	82.68	82.41	82.41	6.90	407	44
DenseNet161	**87.32**	87.55	87.55	87.32	87.32	87.38	87.38	8.50	595	55
EfficientNetB0	83.93	84.03	84.03	83.93	83.93	83.87	83.87	3.65	365	93
ConvNeXt	83.04	82.84	82.84	83.04	83.04	82.90	82.90	5.43	543	87
Vision Transformer	86.07	86.17	86.17	86.07	86.07	86.00	86.00	5.52	453	67
MLP Mixer	83.21	83.29	83.29	83.21	83.21	83.17	83.17	4.08	408	100

Table C.34: Per class results for the pre-trained Vision Transformer model on the RSSCN7 dataset.

Label	Precision	Recall	F1 score
farm_land	97.40	93.75	95.54
forest	100.00	98.75	99.37
grass_land	91.57	95.00	93.25
industrial_region	92.59	93.75	93.17
parking_lot	94.94	93.75	94.34
residential_region	100.00	98.75	99.37
river_lake	95.12	97.50	96.30

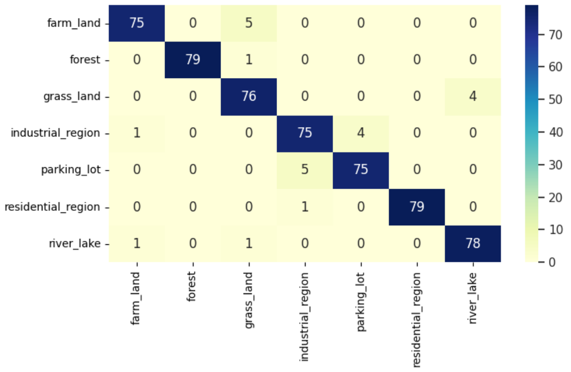

Figure C.29: Confusion matrix for the pre-trained Vision Transformer model on the RSSCN7 dataset.

C.9 SAT6

SAT-6 [48] consists of a total of 405000 image patches each of size 28x28 and covering 6 land cover classes - barren land, trees, grassland, roads, buildings and water bodies (Figure C.30). The authors of the dataset selected 324000 images for the training dataset and 81000 were selected as testing dataset. Additionally we have selected 20% of the images from the train dataset to create the validation split. The training and test datasets were selected from disjoint National Agriculture Imagery Program (NAIP) tiles. The specifications for the various land cover classes of SAT-6 were adopted from those used in the National Land Cover Data (NLCD) algorithm. The class distribution of the train, test and validation splits is presented on Figure C.30.

Detailed results for all pre-trained models are shown on Table C.35 and for all the models learned from scratch are presented on Table C.36. All pre-trained model obtained excellent result on the dataset with ResNet50, ResNet152, DenseNet161, ConvNeXt, Vision Transformer and MLPMixer achieving 100 % accuracy. The results on a class level are show on Table C.37 along with a confusion matrix on Figure C.32 for the DenseNet161 model.

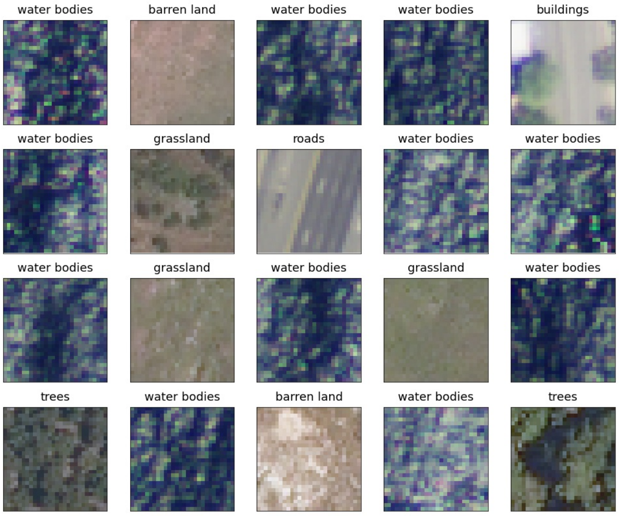

Figure C.30: Example images with labels from the SAT6 dataset.

Table C.35: Detailed results for pre-trained models on the SAT6 dataset.

Model \Metric	Accuracy	Macro Precision	Weighted Precision	Macro Recall	Weighted Recall	Macro F1 score	Weighted F1 score	Avg. time / epoch (sec.)	Total time (sec.)	Best epoch
AlexNet	99.98	99.98	99.98	99.97	99.98	99.97	99.98	92.48	5364	48
VGG16	99.99	99.99	99.99	99.99	99.99	99.99	99.99	550.04	29702	44
ResNet50	100.00	100.00	100.00	100.00	100.00	100.00	100.00	410.33	37340	81
RestNet152	100.00	100.00	100.00	100.00	100.00	100.00	100.00	872.87	61974	61
DenseNet161	100.00	100.00	100.00	100.00	100.00	100.00	100.00	970.39	55312	47
EfficientNetB0	99.99	99.99	99.99	99.99	99.99	99.99	99.99	363.00	8712	14
ConvNeXt	100.00	100.00	100.00	99.99	100.00	100.00	100.00	630.78	42262	57
Vision Transformer	100.00	100.00	100.00	100.00	100.00	100.00	100.00	692.50	42935	52
MLP Mixer	100.00	100.00	100.00	100.00	100.00	100.00	100.00	476.34	15243	22

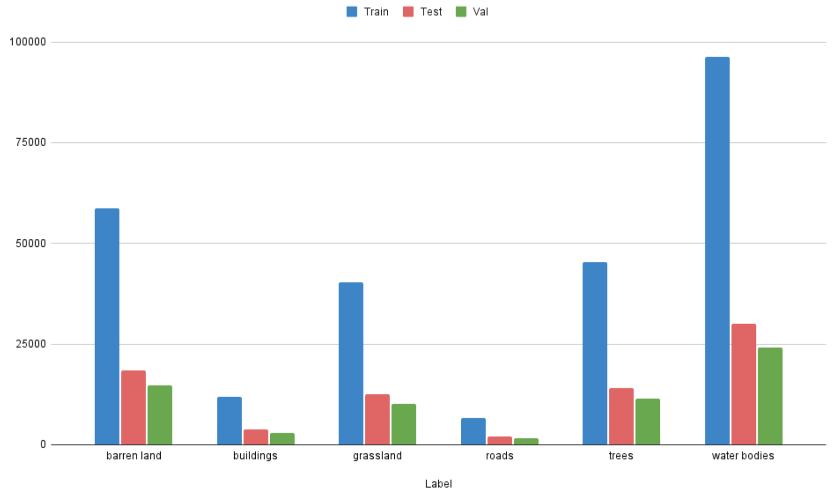

Figure C.31: Class distribution for the SAT6 dataset.

Table C.36: Detailed results for models trained from scratch on the SAT6 dataset.

Model \Metric	Accuracy	Macro Precision	Weighted Precision	Macro Recall	Weighted Recall	Macro F1 score	Weighted F1 score	Avg. time / epoch (sec.)	Total time (sec.)	Best epoch
AlexNet	99.27	98.67	99.27	98.65	99.27	98.66	99.27	107.26	10726	98
VGG16	99.56	99.42	99.56	99.42	99.56	99.42	99.56	579.10	57910	98
ResNet50	100.00	100.00	100.00	100.00	100.00	100.00	100.00	457.04	45704	99
RestNet152	100.00	100.00	100.00	100.00	100.00	100.00	100.00	987.21	98721	94
DenseNet161	100.00	100.00	100.00	100.00	100.00	100.00	100.00	956.03	95603	85
EfficientNetB0	100.00	100.00	100.00	100.00	100.00	100.00	100.00	420.37	42037	95
ConvNeXt	100.00	100.00	100.00	100.00	100.00	100.00	100.00	627.69	62769	97
Vision Transformer	99.99	99.98	99.99	99.98	99.99	99.98	99.99	687.12	61841	75
MLP Mixer	99.98	99.98	99.98	99.96	99.98	99.97	99.98	479.37	47937	95

Table C.37: Per class results for the pre-trained DenseNet model on the SAT6 dataset.

Label	Precision	Recall	F1 score
buildings	100.00	100.00	100.00
barren land	100.00	100.00	100.00
trees	100.00	100.00	100.00
grassland	100.00	100.00	100.00
roads	100.00	100.00	100.00
water bodies	100.00	100.00	100.00

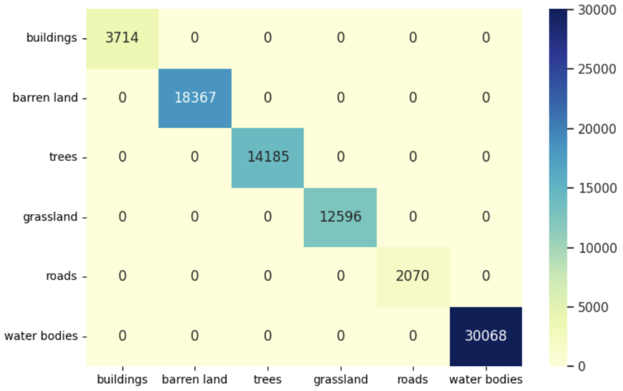

Figure C.32: Confusion matrix for the pre-trained DenseNet161 model on the SAT6 dataset.

C.10 Siri-Whu

The SIRI-WHU [49] is a scene classification dataset comprised of 2400 images organized into 12 classes. Each class contains 200 images with a 2m spatial resolution and a size of 200×200 pixels (Figure C.33). It was collected from Google Earth (Google Inc.) by the Intelligent Data Extraction and Analysis of Remote Sensing (RS_IDEA) Group in Wuhan University. The 12 land-use classes contain agriculture, commercial, harbor, idle land, industrial, meadow, overpass, park, pond, residential, river, and water. This dataset mainly covers urban areas in China, which means it lack diversity and is less challenging. The class distribution is presented on Figure C.34.

Detailed results for all pre-trained models are shown on Table C.38 and for all the models learned from scratch are presented on Table C.39. The best performing model is the pre-trained ResNet152 model. The results on a class level are show on Table C.40 along with a confusion matrix on Figure C.35.

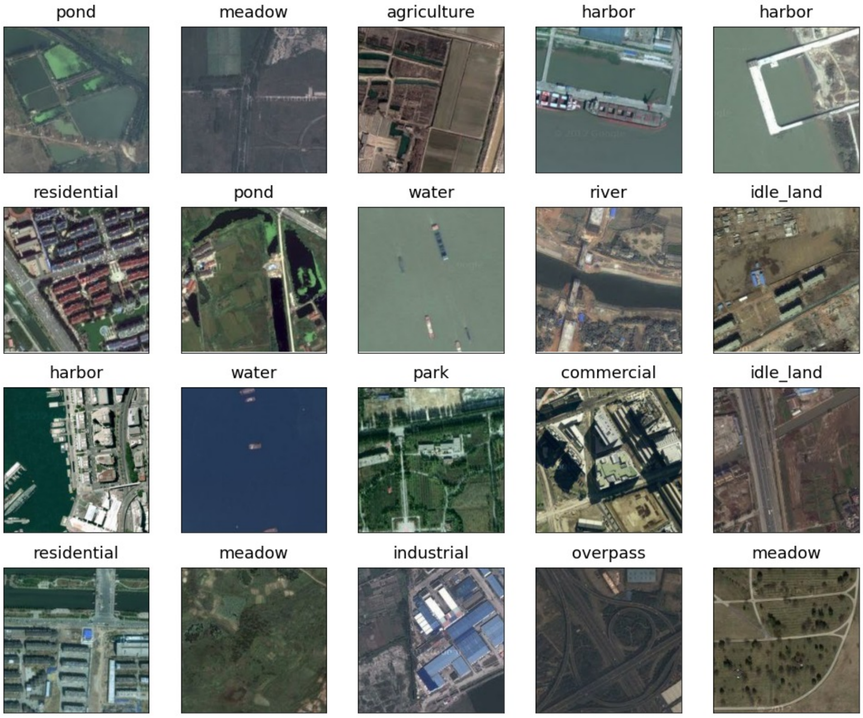

Figure C.33: Example images with labels from the SIRI-WHU dataset.

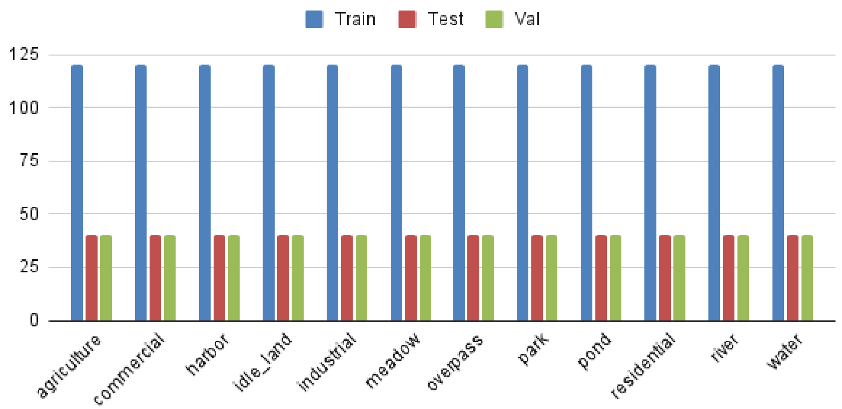

Figure C.34: Class distribution for the SIRI-WHU dataset.

Table C.38: Detailed results for pre-trained models on the SIRI-WHU dataset.

Model \Metric	Accuracy	Macro Precision	Weighted Precision	Macro Recall	Weighted Recall	Macro F1 score	Weighted F1 score	Avg. time / epoch (sec.)	Total time (sec.)	Best epoch
AlexNet	92.29	92.64	92.64	92.29	92.29	92.31	92.31	4.28	197	36
VGG16	93.96	94.08	94.08	93.96	93.96	93.96	93.96	4.98	214	33
ResNet50	95.00	95.12	95.12	95.00	95.00	95.01	95.01	4.66	191	31
RestNet152	**96.25**	96.27	96.27	96.25	96.25	96.24	96.24	6.65	226	24
DenseNet161	95.63	95.64	95.64	95.63	95.63	95.61	95.61	7.30	365	40
EfficientNetB0	95.00	95.09	95.09	95.00	95.00	95.01	95.01	4.57	329	62
ConvNeXt	96.25	96.34	96.34	96.25	96.25	96.24	96.24	5.64	203	26
Vision Transformer	95.63	95.73	95.73	95.63	95.62	95.63	95.63	5.37	322	50
MLP Mixer	95.21	95.36	95.36	95.21	95.21	95.23	95.23	4.55	150	23

Table C.39: Detailed results for models trained from scratch on the SIRI-WHU dataset.

Model \Metric	Accuracy	Macro Precision	Weighted Precision	Macro Recall	Weighted Recall	Macro F1 score	Weighted F1 score	Avg. time / epoch (sec.)	Total time (sec.)	Best epoch
AlexNet	83.75	83.83	83.83	83.75	83.75	83.66	83.66	3.54	326	77
VGG16	84.79	85.05	85.05	84.79	84.79	84.70	84.70	7.32	732	93
ResNet50	**88.96**	89.14	89.14	88.96	88.96	88.94	88.94	3.81	305	65
RestNet152	88.75	88.67	88.67	88.75	88.75	88.62	88.62	6.54	608	78
DenseNet161	86.67	87.38	87.38	86.67	86.67	86.56	86.56	7.49	749	94
EfficientNetB0	86.04	86.23	86.23	86.04	86.04	85.94	85.94	3.61	238	51
ConvNeXt	84.17	84.32	84.32	84.17	84.17	84.09	84.09	11.99	1007	69
Vision Transformer	86.25	86.31	86.31	86.25	86.25	86.14	86.14	5.08	503	84
MLP Mixer	82.50	82.40	82.40	82.50	82.50	82.34	82.34	3.92	392	98

Table C.40: Per class results for the pre-trained ResNet152 model on the SIRI-WHU dataset.

Label	Precision	Recall	F1 score
agriculture	100.00	100.00	100.00
commercial	100.00	97.50	98.73
harbor	90.48	95.00	92.68
idle_land	97.50	97.50	97.50
industrial	100.00	97.50	98.73
meadow	92.11	87.50	89.74
overpass	95.24	100.00	97.56
park	92.31	90.00	91.14
pond	100.00	100.00	100.00
residential	97.56	100.00	98.77
river	92.50	92.50	92.50
water	97.50	97.50	97.50

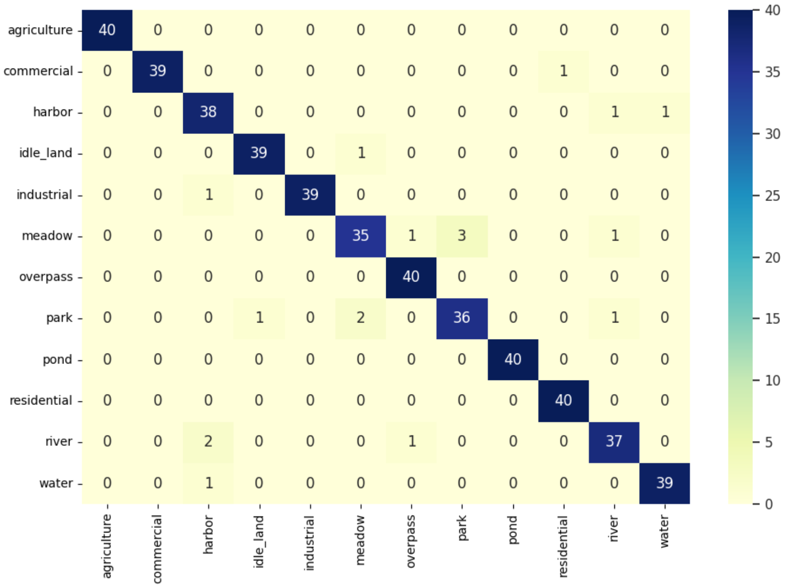

Figure C.35: Confusion matrix for the pre-trained ResNet152 model on the SIRI-WHU dataset.

C.11 CLRS

This dataset [50] is a database designed for the task named Continual/Lifelong learning for remote sensing image scene classification. The proposed CLRS dataset consists of 15000 remote sensing images divided into 25 scene classes covering over 100 countries (Figure C.36). The images have a spatial resolution between 0.26 8.85 meters. The data is acquired from multiple sources such as: Google Earth, Bing Map, Google Map, and Tianditu. The class distribution of the train, test and validation splits is presented on Figure C.37.

Detailed results for all pre-trained models are shown on Table C.41 and for all the models learned from scratch are presented on Table C.42. The best performing model is the pre-trained Vision Transformer model. The results on a class level are show on Table C.43 along with a confusion matrix on Figure C.38.

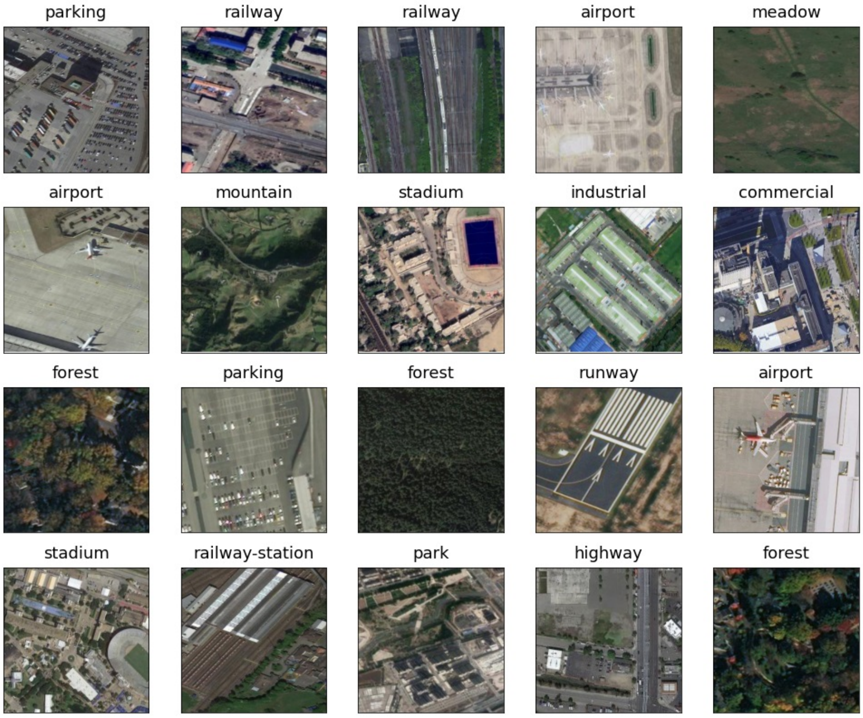

Figure C.36: Example images with labels from the CLRS dataset.

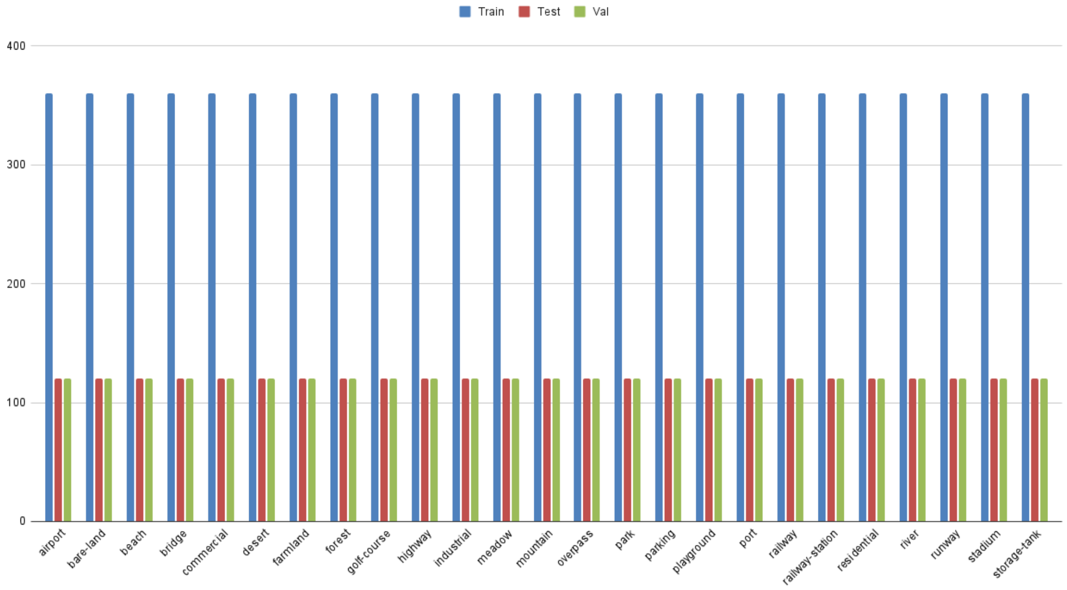

Figure C.37: Class distribution for the CLRS dataset.

Table C.41: Detailed results for pre-trained models on the CLRS dataset.

Model \Metric	Accuracy	Macro Precision	Weighted Precision	Macro Recall	Weighted Recall	Macro F1 score	Weighted F1 score	Avg. time / epoch (sec.)	Total time (sec.)	Best epoch
AlexNet	84.10	84.19	84.19	84.10	84.10	84.03	84.03	20.48	635	21
VGG16	89.90	89.97	89.97	89.90	89.90	89.90	89.90	20.23	607	20
ResNet50	91.57	91.67	91.67	91.57	91.57	91.58	91.58	18.60	279	15
RestNet152	91.90	91.99	91.99	91.90	91.90	91.91	91.91	31.96	799	15
DenseNet161	92.20	92.29	92.29	92.20	92.20	92.20	92.20	35.46	993	18
EfficientNetB0	90.50	90.61	90.61	90.50	90.50	90.49	90.49	19.73	513	16
ConvNeXt	91.10	91.29	91.29	91.10	91.10	91.12	91.12	23.62	496	11
Vision Transformer	**93.20**	93.29	93.29	93.20	93.20	93.22	93.22	25.32	785	21
MLP Mixer	90.10	90.21	90.21	90.10	90.10	90.05	90.05	19.75	316	6

Table C.42: Detailed results for models trained from scratch on the CLRS dataset.

Model \Metric	Accuracy	Macro Precision	Weighted Precision	Macro Recall	Weighted Recall	Macro F1 score	Weighted F1 score	Avg. time / epoch (sec.)	Total time (sec.)	Best epoch
AlexNet	71.40	71.59	71.59	71.40	71.40	71.33	71.33	20.35	2035	92
VGG16	76.07	76.20	76.20	76.07	76.07	76.00	76.00	19.33	1450	60
ResNet50	85.57	85.72	85.72	85.57	85.57	85.57	85.57	19.43	1788	77
RestNet152	82.30	82.47	82.47	82.30	82.30	82.19	82.19	32.05	2373	60
DenseNet161	**86.17**	86.29	86.29	86.17	86.17	86.18	86.18	35.81	2757	62
EfficientNetB0	82.27	82.55	82.55	82.27	82.27	82.31	82.31	20.71	1512	58
ConvNeXt	69.17	69.02	69.02	69.17	69.17	69.01	69.01	23.09	2309	96
Vision Transformer	65.47	66.41	66.41	65.47	65.47	65.49	65.49	24.96	1173	32
MLP Mixer	61.13	62.18	62.18	61.13	61.13	60.87	60.87	17.98	809	30

Table C.43: Per class results for the pre-trained Vision Transformer model on the CLRS dataset.

Label	Precision	Recall	F1 score
airport	97.48	96.67	97.07
bare-land	92.00	95.83	93.88
beach	99.15	97.50	98.32
bridge	90.91	91.67	91.29
commercial	79.84	85.83	82.73
desert	97.50	97.50	97.50
farmland	93.70	99.17	96.36
forest	100.00	100.00	100.00
golf-course	94.96	94.17	94.56
highway	92.11	87.50	89.74
industrial	88.79	85.83	87.29
meadow	96.72	98.33	97.52
mountain	99.15	97.50	98.32
overpass	89.68	94.17	91.87
park	85.60	89.17	87.35
parking	98.25	93.33	95.73
playground	95.04	95.83	95.44
port	94.74	90.00	92.31
railway	86.29	89.17	87.70
railway-station	88.79	85.83	87.29
residential	90.68	89.17	89.92
river	90.32	93.33	91.80
runway	98.33	98.33	98.33
stadium	95.61	90.83	93.16
storage-tank	96.55	93.33	94.92

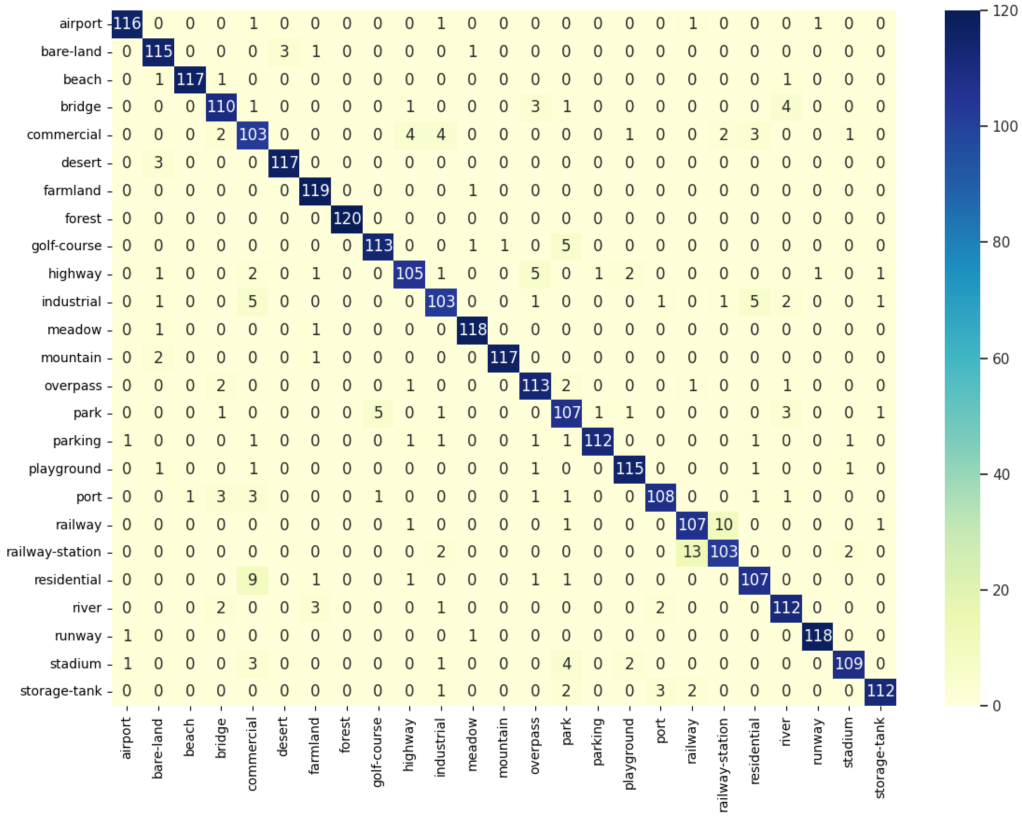

	airport	bare-land	beach	bridge	commercial	desert	farmland	forest	golf-course	highway	industrial	meadow	mountain	overpass	park	parking	playground	port	railway	railway-station	residential	river	runway	stadium	storage-tank
airport	116	0	0	0	1	0	0	0	0	0	1	0	0	0	0	0	0	0	1	0	0	0	1	0	0
bare-land	0	115	0	0	0	3	1	0	0	0	0	1	0	0	0	0	0	0	0	0	0	0	0	0	0
beach	0	1	117	1	0	0	0	0	0	0	0	0	0	0	0	0	0	0	0	0	0	1	0	0	0
bridge	0	0	0	110	1	0	0	0	0	1	0	0	0	3	1	0	0	0	0	0	0	4	0	0	0
commercial	0	0	0	2	103	0	0	0	0	4	4	0	0	0	0	0	1	0	0	2	3	0	0	1	0
desert	0	3	0	0	0	117	0	0	0	0	0	0	0	0	0	0	0	0	0	0	0	0	0	0	0
farmland	0	0	0	0	0	0	119	0	0	0	0	1	0	0	0	0	0	0	0	0	0	0	0	0	0
forest	0	0	0	0	0	0	0	120	0	0	0	0	0	0	0	0	0	0	0	0	0	0	0	0	0
golf-course	0	0	0	0	0	0	0	0	113	0	0	1	1	0	5	0	0	0	0	0	0	0	0	0	0
highway	0	1	0	0	2	0	1	0	0	105	1	0	0	5	0	1	2	0	0	0	0	0	1	0	1
industrial	0	1	0	0	5	0	0	0	0	0	103	0	0	1	0	0	0	1	0	1	5	2	0	0	1
meadow	0	1	0	0	0	0	1	0	0	0	0	118	0	0	0	0	0	0	0	0	0	0	0	0	0
mountain	0	2	0	0	0	0	1	0	0	0	0	0	117	0	0	0	0	0	0	0	0	0	0	0	0
overpass	0	0	0	2	0	0	0	0	0	1	0	0	0	113	2	0	0	0	1	0	0	1	0	0	0
park	0	0	0	1	0	0	0	0	5	0	1	0	0	0	107	1	1	0	0	0	0	3	0	0	1
parking	1	0	0	0	1	0	0	0	0	1	1	0	0	1	1	112	0	0	0	0	1	0	0	1	0
playground	0	1	0	0	1	0	0	0	0	0	0	0	0	1	0	0	115	0	0	0	1	0	0	1	0
port	0	0	1	3	3	0	0	0	1	0	0	0	0	1	1	0	0	108	0	0	1	1	0	0	0
railway	0	0	0	0	0	0	0	0	0	1	0	0	0	0	1	0	0	0	107	10	0	0	0	0	1
railway-station	0	0	0	0	0	0	0	0	0	0	2	0	0	0	0	0	0	0	13	103	0	0	0	2	0
residential	0	0	0	0	9	0	1	0	0	1	0	0	0	1	1	0	0	0	0	0	107	0	0	0	0
river	0	0	0	2	0	0	3	0	0	0	1	0	0	0	0	0	0	2	0	0	0	112	0	0	0
runway	1	0	0	0	0	0	0	0	0	0	0	1	0	0	0	0	0	0	0	0	0	0	118	0	0
stadium	1	0	0	0	3	0	0	0	0	0	1	0	0	0	4	0	2	0	0	0	0	0	0	109	0
storage-tank	0	0	0	0	0	0	0	0	0	0	1	0	0	0	2	0	0	3	2	0	0	0	0	0	112

Figure C.38: Confusion matrix for the pre-trained Vision Transformer model on the CLRS dataset.

C.12 RSD46-WHU

RSD46-WHU is a large-scale open dataset for scene classification in remote sensing images. The dataset is manually collected from Google Earth and Tianditu. The ground resolution of most classes is 0.5m, and the others are about 2m. There are 500-3000 images in each class. The RSD46-WHU dataset contains around 117000 images with 46 classes (Figure C.39). The image are not evenly distributed between classes and each class contains between 428 to 3000 images. The dataset comes with predefined train and test splits. For creating the validation split we used 20% of the images from the train split. The class distribution of the different splits is presented on Figure C.40.

Detailed results for all pre-trained models are shown on Table C.44 and for all the models learned from scratch are presented on Table C.45. The best performing model is the pre-trained DenseNet161 model. The results on a class level are show on Table C.46 along with a confusion matrix on Figure C.41.

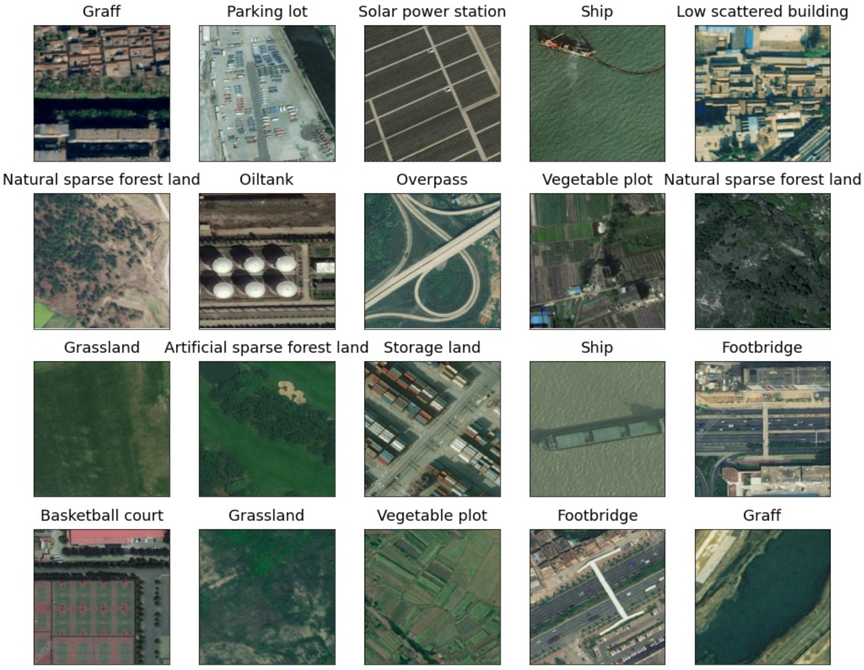

Figure C.39: Example images with labels from the RSD46-WHU dataset.

Table C.44: Detailed results for pre-trained models on the RSD46-WHU dataset.

Model \Metric	Accuracy	Macro Precision	Weighted Precision	Macro Recall	Weighted Recall	Macro F1 score	Weighted F1 score	Avg. time / epoch (sec.)	Total time (sec.)	Best epoch
AlexNet	90.65	90.43	90.61	90.35	90.65	90.36	90.61	58.03	2031	25
VGG16	92.42	92.30	92.38	92.25	92.42	92.22	92.37	158.32	4433	18
ResNet50	94.16	94.07	94.15	94.18	94.16	94.11	94.14	123.27	3205	16
RestNet152	94.40	94.33	94.40	94.41	94.40	94.36	94.39	269.45	7814	19
DenseNet161	**94.51**	94.36	94.49	94.41	94.51	94.36	94.48	297.70	6847	13
EfficientNetB0	93.39	93.20	93.38	93.39	93.39	93.26	93.35	111.55	2231	10
ConvNeXt	93.63	93.61	93.67	93.47	93.63	93.48	93.60	196.20	3924	10
Vision Transformer	94.24	94.38	94.23	94.08	94.24	94.16	94.20	210.37	3997	9
MLP Mixer	93.67	93.77	93.69	93.47	93.67	93.55	93.65	148.25	3558	14

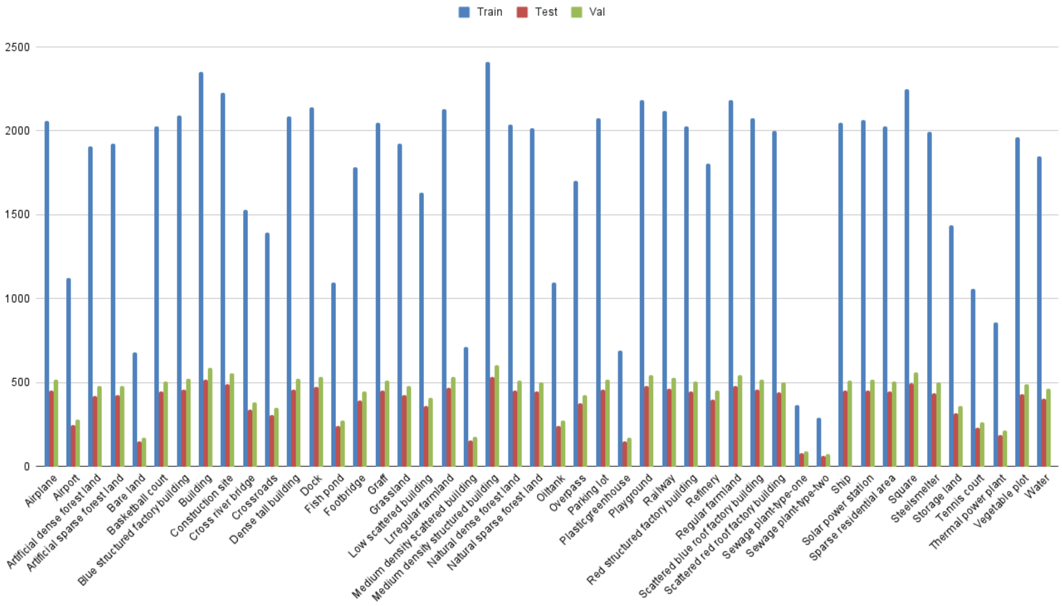

Figure C.40: Class distribution for the RSD46-WHU dataset.

Table C.45: Detailed results for models trained from scratch on the RSD46-WHU dataset.

Model \Metric	Accuracy	Macro Precision	Weighted Precision	Macro Recall	Weighted Recall	Macro F1 score	Weighted F1 score	Avg. time / epoch (sec.)	Total time (sec.)	Best epoch
AlexNet	86.03	85.83	86.03	85.67	86.03	85.71	85.99	58.84	3707	48
VGG16	88.62	88.37	88.56	88.37	88.62	88.32	88.55	162.89	8796	39
ResNet50	90.55	90.40	90.53	90.26	90.55	90.30	90.52	127.53	8672	53
RestNet152	89.94	89.84	89.99	89.77	89.94	89.78	89.95	272.70	19907	58
DenseNet161	**92.21**	92.11	92.23	92.03	92.21	92.06	92.21	301.16	15318	36
EfficientNetB0	90.61	90.57	90.61	90.25	90.61	90.37	90.58	113.93	6446	40
ConvNeXt	88.69	88.66	88.67	88.33	88.69	88.46	88.66	194.93	11891	46
Vision Transformer	86.47	86.22	86.45	85.94	86.47	86.02	86.42	211.93	9325	29
MLP Mixer	81.25	81.56	81.59	80.11	81.25	80.51	81.19	148.42	4149	12

Table C.46: Per class results for the pre-trained DenseNet161 model on the RSD46-WHU dataset.

Label	Precision	Recall	F1 score
Airplane	99.56	99.78	99.67
Airport	98.39	99.19	98.79
Artificial dense forest land	87.11	86.90	87.01
Artificial sparse forest land	87.06	82.55	84.75
Bare land	94.12	96.00	95.05
Basketball court	90.37	92.39	91.37
Blue structured factory building	96.57	97.83	97.19
Building	82.44	83.40	82.92
Construction site	82.11	79.43	80.75
Cross river bridge	99.70	99.70	99.70
Crossroads	97.74	98.70	98.22
Dense tall building	94.35	94.35	94.35
Dock	98.94	98.73	98.83
Fish pond	97.52	97.93	97.72
Footbridge	99.49	99.24	99.36
Graff	98.37	93.79	96.03
Grassland	95.07	95.52	95.29
Low scattered building	96.15	97.49	96.82
Lrregular farmland	97.68	98.51	98.09
Medium density scattered building	76.98	68.15	72.30
Medium density structured building	89.58	92.11	90.82
Natural dense forest land	95.40	96.89	96.14
Natural sparse forest land	93.16	97.98	95.51
Oiltank	90.66	96.68	93.57
Overpass	99.19	98.13	98.66
Parking lot	96.49	96.07	96.28
Plasticgreenhouse	100.00	99.34	99.67
Playground	96.85	95.84	96.34
Railway	99.14	99.14	99.14
Red structured factory building	97.78	98.66	98.22
Refinery	92.84	87.72	90.21
Regular farmland	95.20	94.80	95.00
Scattered blue roof factory building	94.44	96.72	95.57
Scattered red roof factory building	93.28	97.73	95.45
Sewage plant-type-one	95.06	96.25	95.65
Sewage plant-type-two	88.73	98.44	93.33
Ship	99.56	99.33	99.45
Solar power station	99.78	99.78	99.78
Sparse residential area	91.42	88.14	89.75
Square	94.52	97.38	95.93
Steelsmelter	90.48	90.89	90.68
Storage land	99.03	96.52	97.76
Tennis court	95.93	91.38	93.60
Thermal power plant	88.95	85.19	87.03
Vegetable plot	94.12	92.59	93.35
Water	99.02	99.51	99.26

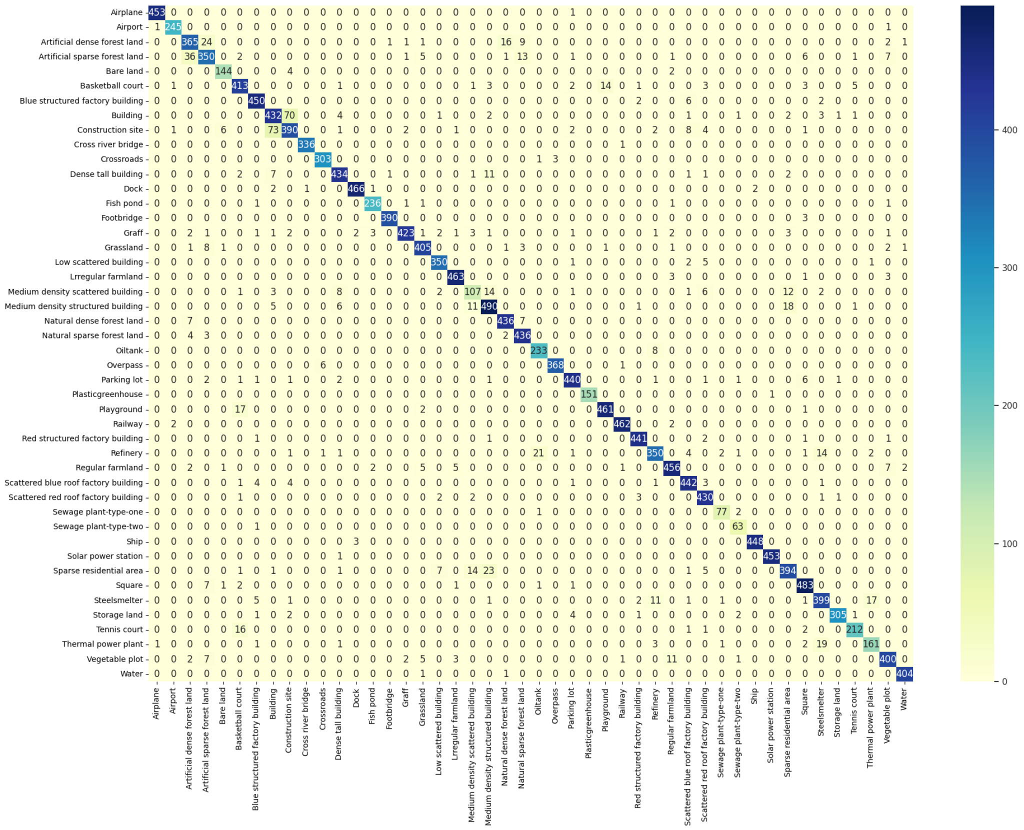

Figure C.41: Confusion matrix for the pre-trained DenseNet161 model on the RSD46-WHU dataset.

C.13 Brazilian Coffee Scenes

The Brazilian Coffee Scenes dataset [53] consists of only two classes: coffee and non-coffee class. Each class has 1438 images with 64x64 pixels cropped from SPOT satellite images over four counties in the state of Minas Gerais, Brazil: Arceburgo, Guaranesia, Guaxupe, and Monte Santo (Figure C.42). The images in the dataset are in green, red and near-infrared spectral bands, since these are most useful and representative for distinguishing vegetation areas. The dataset is manually annotated by agricultural researchers. Images which contain coffee pixels in at least 85% of the image were assigned to the coffee class. Image with less than 10% of coffee pixels are assigned to the non-coffee class. The number of classes and the degree to which the data is tailored, should make this less challenging dataset. The class distribution is presented on Figure C.43.

Detailed results for all pre-trained models are shown on Table C.47 and for all the models learned from scratch are presented on Table C.48. The best performing model is the pre-trained MLPMixer model. The results on a class level are show on Table C.49 along with a confusion matrix on Figure C.44.

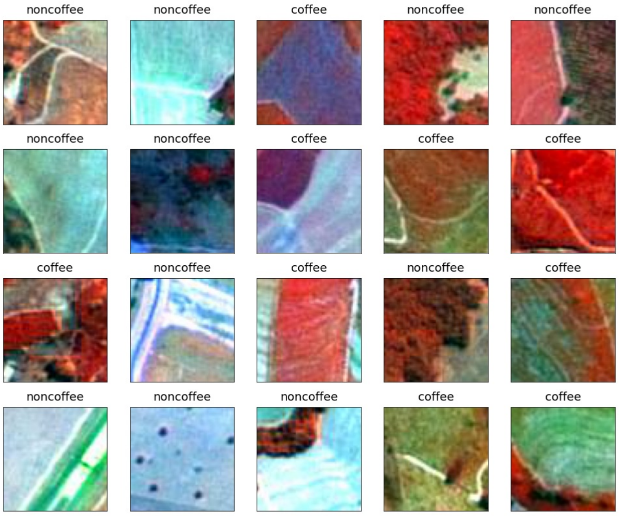

Figure C.42: Example images with labels from the Brazilian Coffee Scenes dataset.

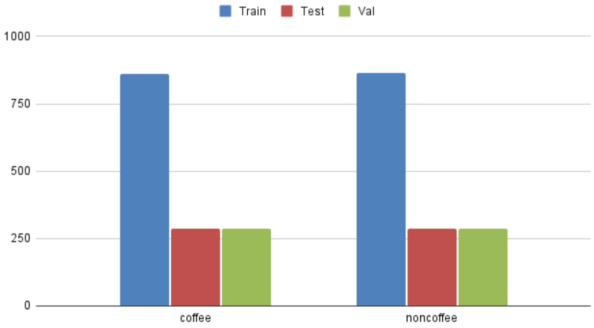

Figure C.43: Class distribution for the Brazilian Coffee Scenes dataset.

Table C.47: Detailed results for pre-trained models on the Brazilian Coffee Scenes dataset.

Model \Metric	Accuracy	Macro Precision	Weighted Precision	Macro Recall	Weighted Recall	Macro F1 score	Weighted F1 score	Avg. time / epoch (sec.)	Total time (sec.)	Best epoch
AlexNet	89.58	89.59	89.59	89.58	89.58	89.58	89.58	1.48	43	19
VGG16	90.97	91.00	91.00	90.97	90.97	90.97	90.97	4.17	121	19
ResNet50	92.01	92.06	92.06	92.01	92.01	92.01	92.01	3.45	76	12
RestNet152	92.36	92.37	92.37	92.36	92.36	92.36	92.36	6.61	119	8
DenseNet161	92.71	92.81	92.81	92.71	92.71	92.70	92.70	7.33	176	14
EfficientNetB0	91.32	91.32	91.32	91.32	91.32	91.32	91.32	3.17	133	32
ConvNeXt	91.49	91.58	91.58	91.49	91.49	91.49	91.49	5.08	132	16
Vision Transformer	92.01	92.03	92.03	92.01	92.01	92.01	92.01	5.07	76	5
MLP Mixer	**93.06**	93.07	93.07	93.06	93.06	93.05	93.05	3.94	67	7

Table C.48: Detailed results for models trained from scratch on the Brazilian Coffee Scenes dataset.

Model \Metric	Accuracy	Macro Precision	Weighted Precision	Macro Recall	Weighted Recall	Macro F1 score	Weighted F1 score	Avg. time / epoch (sec.)	Total time (sec.)	Best epoch
AlexNet	89.41	89.62	89.62	89.41	89.41	89.40	89.40	1.53	115	60
VGG16	89.41	89.45	89.45	89.41	89.41	89.41	89.41	5.95	440	59
ResNet50	89.24	89.39	89.39	89.24	89.24	89.23	89.23	4.55	296	50
RestNet152	88.54	88.56	88.56	88.54	88.54	88.54	88.54	7.95	469	44
DenseNet161	**90.80**	90.80	90.80	90.80	90.80	90.80	90.80	7.31	373	36
EfficientNetB0	85.42	85.71	85.71	85.42	85.42	85.39	85.39	3.26	326	98
ConvNeXt	84.38	84.39	84.39	84.38	84.38	84.37	84.37	5.09	509	95
Vision Transformer	87.85	87.89	87.89	87.85	87.85	87.84	87.84	5.55	322	43
MLP Mixer	86.28	86.29	86.29	86.28	86.28	86.28	86.28	4.47	201	30

Table C.49: Per class results for MLPMixer on the Brazilian Coffee Scenes dataset.

Label	Precision	Recall	F1 score
coffee	92.18	94.10	93.13
noncoffee	93.97	92.01	92.98

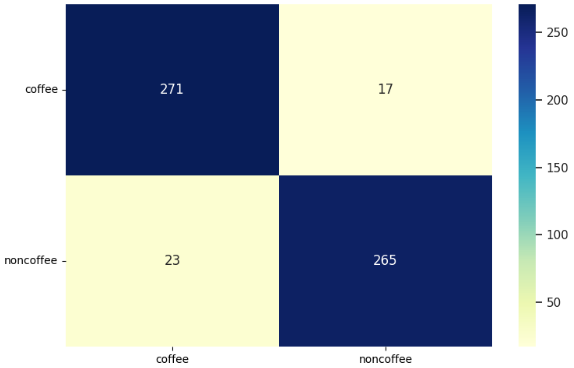

Figure C.44: Confusion matrix for MLPMixer on the Brazilian Coffee Scenes dataset.

C.14 Optimal 31

The Optimal 31 dataset [52] is for remote sensing image scene classification. The dataset contains 31 classes, each class contains 60 images with a size of 256×256 pixels. Totaling 1860 aerial RGB images (Figure C.45). These classes include: airplane, airport, basketball court, baseball field, bridge, beach, bushes, crossroads, church, round farmland, business district, desert, harbor, dense houses, factory, forest, freeway, golf field, island, lake, meadow, medium houses, mountain, mobile house area, overpass, playground, parking lot, roundabout, runway, railway, and square farmland. It is considered challenging due to small number of images dispersed across many classes. We have generated train, test and validation spits for our study and their class distribution is presented on Figure C.46.

Detailed results for all pre-trained models are shown on Table C.50 and for all the models learned from scratch are presented on Table C.51. The best performing model is the pre-trained Vision Transformer model. The results on a class level are show on Table C.52 along with a confusion matrix on Figure C.47.

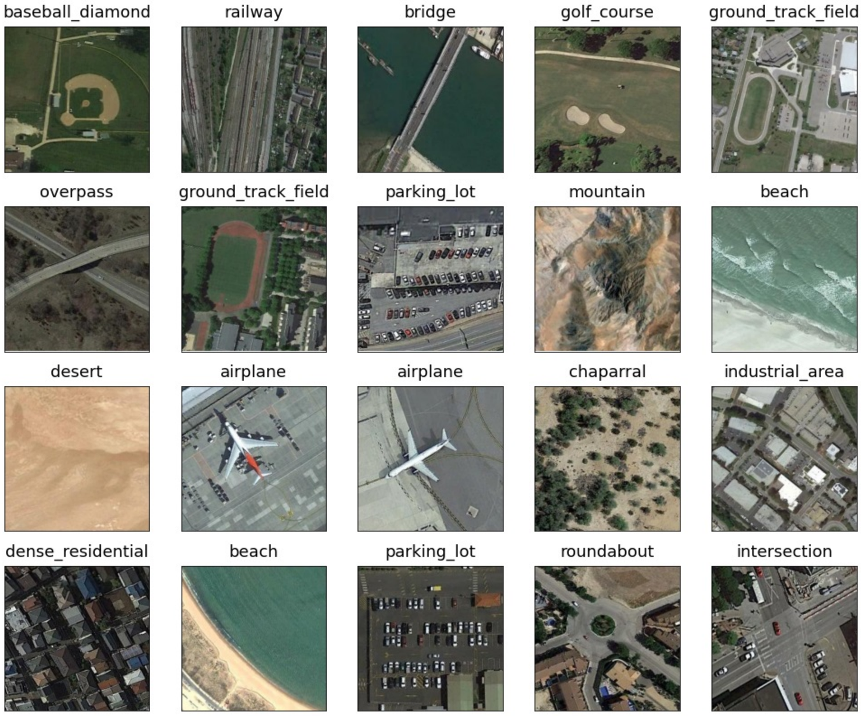

Figure C.45: Example images with labels from the Optimal 31 dataset.

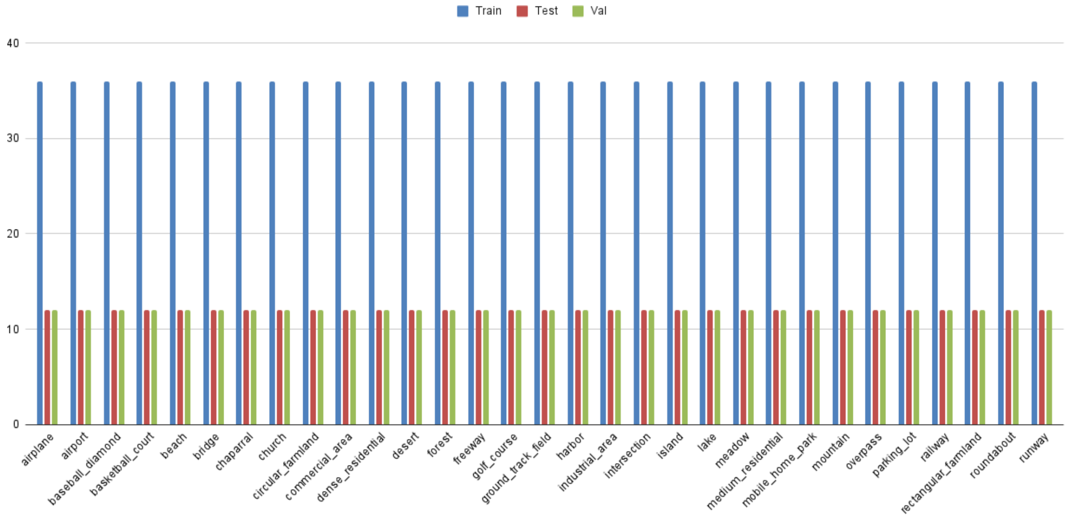

Figure C.46: Class distribution for the Optimal 31 dataset.

Table C.50: Detailed results for pre-trained models on the Optimal 31 dataset.

Model \Metric	Accuracy	Macro Precision	Weighted Precision	Macro Recall	Weighted Recall	Macro F1 score	Weighted F1 score	Avg. time / epoch (sec.)	Total time (sec.)	Best epoch
AlexNet	80.91	81.90	81.90	80.91	80.91	80.74	80.74	1.10	45	31
VGG16	88.71	89.58	89.58	88.71	88.71	88.79	88.79	2.97	95	22
ResNet50	92.20	92.85	92.85	92.20	92.20	92.25	92.25	2.58	129	40
RestNet152	92.47	92.99	92.99	92.47	92.47	92.47	92.47	4.62	217	37
DenseNet161	94.35	94.92	94.92	94.35	94.35	94.43	94.43	5.02	306	51
EfficientNetB0	91.67	92.04	92.04	91.67	91.67	91.60	91.60	2.25	187	73
ConvNeXt	93.01	93.33	93.33	93.01	93.01	92.99	92.99	3.50	203	48
Vision Transformer	**94.62**	94.85	94.85	94.62	94.62	94.56	94.56	3.71	126	24
MLP Mixer	92.74	93.17	93.17	92.74	92.74	92.74	92.74	2.82	141	40

Table C.51: Detailed results for models trained from scratch on the Optimal 31 dataset.

Model \Metric	Accuracy	Macro Precision	Weighted Precision	Macro Recall	Weighted Recall	Macro F1 score	Weighted F1 score	Avg. time / epoch (sec.)	Total time (sec.)	Best epoch
AlexNet	55.11	55.61	55.61	55.11	55.11	54.24	54.24	1.23	101	67
VGG16	56.72	58.89	58.89	56.72	56.72	56.58	56.58	4.81	409	70
ResNet50	67.20	69.56	69.56	67.20	67.20	67.17	67.17	2.60	161	47
RestNet152	62.90	64.95	64.95	62.90	62.90	62.78	62.78	5.92	314	38
DenseNet161	**71.24**	72.01	72.01	71.24	71.24	70.65	70.65	5.16	330	49
EfficientNetB0	68.55	70.59	70.59	68.55	68.55	68.70	68.70	2.36	156	51
ConvNeXt	58.87	60.69	60.69	58.87	58.87	58.92	58.92	3.59	330	77
Vision Transformer	62.63	63.89	63.89	62.63	62.63	62.32	62.32	3.79	235	47
MLP Mixer	59.14	60.36	60.36	59.14	59.14	58.47	58.47	3.26	326	98

Table C.52: Per class results for the pre-trained Vision Transformer model on the Optimal 31 dataset.

Label	Precision	Recall	F1 score
airplane	100.00	100.00	100.00
airport	100.00	100.00	100.00
baseball_diamond	92.31	100.00	96.00
basketball_court	100.00	100.00	100.00
beach	100.00	100.00	100.00
bridge	100.00	91.67	95.65
chaparral	100.00	100.00	100.00
church	100.00	91.67	95.65
circular_farmland	92.31	100.00	96.00
commercial_area	85.71	100.00	92.31
dense_residential	84.62	91.67	88.00
desert	100.00	91.67	95.65
forest	91.67	91.67	91.67
freeway	100.00	91.67	95.65
golf_course	91.67	91.67	91.67
ground_track_field	92.31	100.00	96.00
harbor	85.71	100.00	92.31
industrial_area	84.62	91.67	88.00
intersection	100.00	100.00	100.00
island	100.00	100.00	100.00
lake	91.67	91.67	91.67
meadow	83.33	83.33	83.33
medium_residential	88.89	66.67	76.19
mobile_home_park	90.91	83.33	86.96
mountain	100.00	100.00	100.00
overpass	92.31	100.00	96.00
parking_lot	100.00	100.00	100.00
railway	92.31	100.00	96.00
rectangular_farmland	100.00	83.33	90.91
roundabout	100.00	100.00	100.00
runway	100.00	91.67	95.65

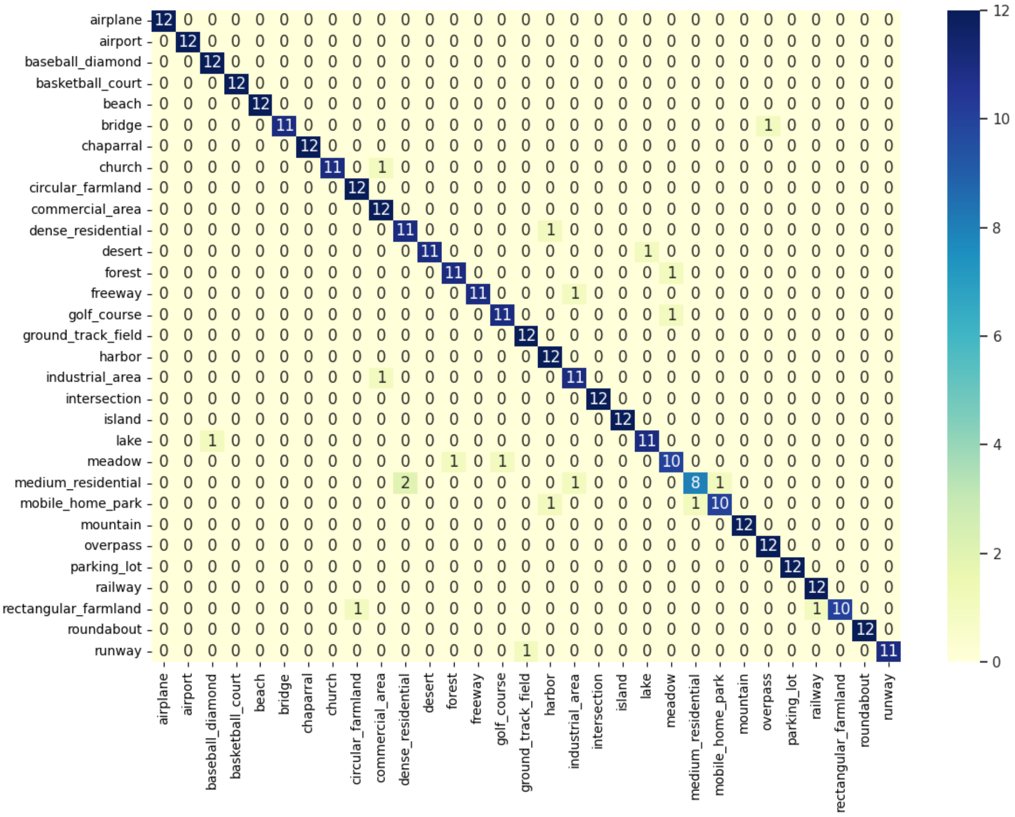

Figure C.47: Confusion matrix for the pre-trained Vision Transformer model on the Optimal 31 dataset.

C.15 So2Sat

This dataset [54] consists of co-registered synthetic aperture radar and multispectral optical image patches acquired by the Sentinel-1 and Sentinel-2 remote sensing satellites, and the corresponding local climate zones (LCZ) label. So2Sat has a total of 400673 images of size 32x32 pixels organized into 17 classes. Sample images are shown on Figure C.45.

The dataset is distributed over 42 cities across different continents and cultural regions of the world. The classes include: compact high rise, compact middle rise, compact low rise, open high rise, open middle rise, open low rise, lightweight low rise, large low rise, sparsely built, heavy industry, dense trees, scattered trees, bush scrub, low plants, bare rock or paved, bare soil or sand, and water.

The creators of So2Sat have provided different versions for train, test and validation splits for the dataset. The class distribution of the splits is depicted on Figure C.49. We are using Version 2 [4] with only Sentinel 2 data. Version 2 provides a training set covering 42 cities around the world, a validation set covering western half of 10 other cities covering 10 cultural zones and a test set containing the eastern half of the 10 other cities.

Detailed results for all pre-trained models are shown on Table C.53 and for all the models learned from scratch are presented on Table C.54. The best performing model is the pre-trained Vision Transformer model. The results on a class level are show on Table C.55 along with a confusion matrix on Figure C.50.

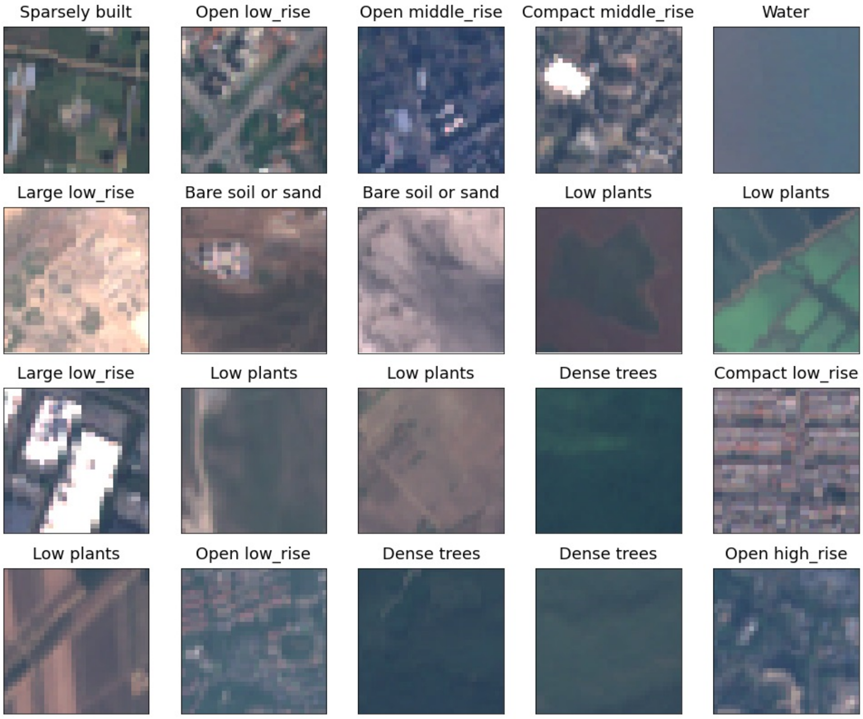

Figure C.48: Example images with labels from the So2Sat dataset.

[4] available at So2Sat-LCZ42 repo https://github.com/zhu-xlab/So2Sat-LCZ42.

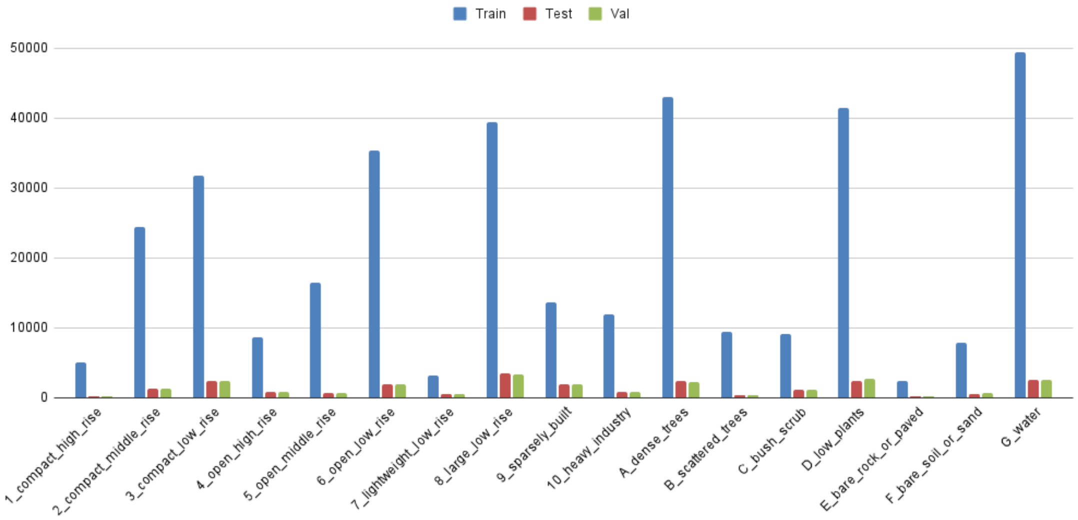

Figure C.49: Class distribution for the So2Sat dataset.

Table C.53: Detailed results for pre-trained models on the So2Sat dataset.

Model \Metric	Accuracy	Macro Precision	Weighted Precision	Macro Recall	Weighted Recall	Macro F1 score	Weighted F1 score	Avg. time / epoch (sec.)	Total time (sec.)	Best epoch
AlexNet	59.20	46.01	59.31	42.70	59.20	41.57	57.59	158.09	1790	1
VGG16	65.38	57.30	64.34	50.00	65.38	49.64	63.00	716.09	7877	1
ResNet50	61.90	51.01	60.88	48.45	61.90	48.35	60.41	565.55	6221	1
ResNet152	65.17	56.66	64.48	53.42	65.17	52.93	63.75	1,200.64	13207	1
DenseNet161	65.76	55.47	64.58	48.59	65.76	48.67	63.81	1,324.09	14784	1
EfficientNetB0	65.80	56.30	65.64	53.37	65.80	53.65	64.77	510.45	5615	1
ConvNeXt	66.17	59.11	66.87	54.87	66.17	54.71	65.56	853.91	9393	1
Vision Transformer	**68.55**	62.95	69.64	57.17	68.55	57.26	67.48	925.09	10176	1
MLP Mixer	67.07	63.74	68.25	51.34	67.07	51.94	65.66	643.91	7278	1

Table C.54: Detailed results for models trained from scratch on the So2Sat dataset.

Model \Metric	Accuracy	Macro Precision	Weighted Precision	Macro Recall	Weighted Recall	Macro F1 score	Weighted F1 score	Avg. time / epoch (sec.)	Total time (sec.)	Best epoch
AlexNet	56.51	41.86	54.97	40.70	56.51	39.72	54.65	174.74	3320	4
VGG16	62.27	51.36	61.08	45.40	62.27	45.54	59.78	723.72	13027	3
ResNet50	59.59	46.54	59.35	43.94	59.59	43.37	58.18	558.79	10617	4
ResNet152	61.48	49.43	62.30	48.71	61.48	46.98	60.22	1,198.37	22769	4
DenseNet161	55.43	48.87	60.98	42.53	55.43	40.76	54.11	1,325.67	23862	3
EfficientNetB0	**65.17**	53.75	64.00	50.34	65.17	50.36	63.88	499.21	11981	9
ConvNeXt	60.15	50.97	61.52	48.03	60.15	47.17	59.73	851.06	15319	3
Vision Transformer	55.33	43.56	55.31	37.42	55.33	37.01	52.20	926.50	14824	1
MLP Mixer	53.58	42.31	53.80	36.73	53.58	36.61	51.19	651.31	10421	1

Table C.55: Per class results for the pre-trained Vision Transformer model on the So2Sat dataset.

Label	Precision	Recall	F1 score
Compact high_rise	62.37	21.80	32.31
Compact middle_rise	70.74	61.49	65.79
Compact low_rise	68.52	75.33	71.77
Open high_rise	76.54	59.39	66.89
Open middle_rise	56.12	59.50	57.76
Open low_rise	47.29	64.36	54.52
Lightweight low_rise	57.14	39.76	46.89
Large low_rise	87.11	84.87	85.98
Sparsely built	67.30	45.80	54.51
Heavy industry	39.39	69.49	50.28
Dense trees	97.11	73.86	83.91
Scattered trees	26.16	55.89	35.64
Bush or scrub	15.22	1.80	3.22
Low plants	60.68	90.55	72.66
Bare rock or paved	79.38	37.56	50.99
Bare soil or sand	62.05	32.87	42.97
Water	97.10	97.60	97.35

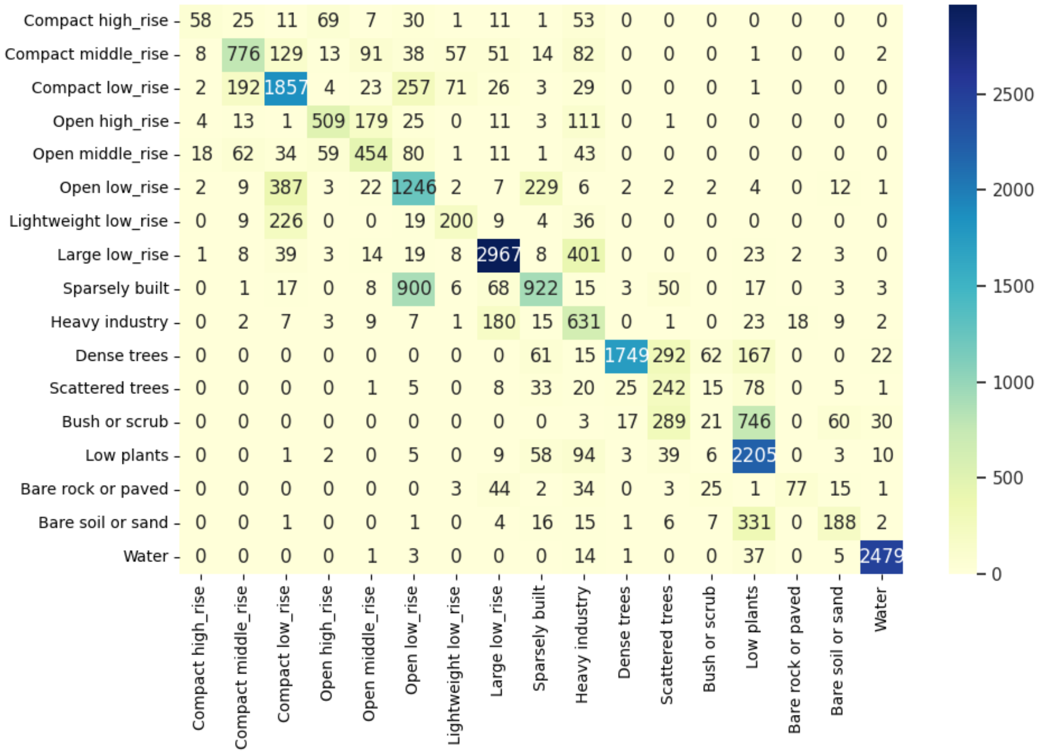

	Compact high_rise	Compact middle_rise	Compact low_rise	Open high_rise	Open middle_rise	Open low_rise	Lightweight low_rise	Large low_rise	Sparsely built	Heavy industry	Dense trees	Scattered trees	Bush or scrub	Low plants	Bare rock or paved	Bare soil or sand	Water
Compact high_rise	58	25	11	69	7	30	1	11	1	53	0	0	0	0	0	0	0
Compact middle_rise	8	776	129	13	91	38	57	51	14	82	0	0	0	1	0	0	2
Compact low_rise	2	192	1857	4	23	257	71	26	3	29	0	0	0	1	0	0	0
Open high_rise	4	13	1	509	179	25	0	11	3	111	0	1	0	0	0	0	0
Open middle_rise	18	62	34	59	454	80	1	11	1	43	0	0	0	0	0	0	0
Open low_rise	2	9	387	3	22	1246	2	7	229	6	2	2	2	4	0	12	1
Lightweight low_rise	0	9	226	0	0	19	200	9	4	36	0	0	0	0	0	0	0
Large low_rise	1	8	39	3	14	19	8	2967	8	401	0	0	0	23	2	3	0
Sparsely built	0	1	17	0	8	900	6	68	922	15	3	50	0	17	0	3	3
Heavy industry	0	2	7	3	9	7	1	180	15	631	0	1	0	23	18	9	2
Dense trees	0	0	0	0	0	0	0	0	61	15	1749	292	62	167	0	0	22
Scattered trees	0	0	0	0	1	5	0	8	33	20	25	242	15	78	0	5	1
Bush or scrub	0	0	0	0	0	0	0	0	0	3	17	289	21	746	0	60	30
Low plants	0	0	1	2	0	5	0	9	58	94	3	39	6	2205	0	3	10
Bare rock or paved	0	0	0	0	0	0	3	44	2	34	0	3	25	1	77	15	1
Bare soil or sand	0	0	1	0	0	1	0	4	16	15	1	6	7	331	0	188	2
Water	0	0	0	0	1	3	0	0	0	14	1	0	0	37	0	5	2479

Figure C.50: Confusion matrix for the pre-trained Vision Transformer model on the So2Sat dataset.

C.16 UC Merced multi-label

The UC Merced dataset was extended in [55] for multi-label classification. The dataset still has the same number of 2100 images of 256x256 pixels size (Figure C.51). The difference is in the number of classes (labels) and the number of annotations (classes) an image belongs to. Each image in the dataset has been manually labeled with one or more (maximum seven) labels based on visual inspection in order to create the ground truth data (the multilabels are available at http://bigearth.eu/datasets). The total number of distinct class labels in the dataset is 17. The labels are: airplane, bare-soil, buildings, cars, chaparral, court, dock, field, grass, mobile-home, pavement, sand, sea, ship, tanks, trees, water. The average number of labels per image is 3.3. This dataset has no predefined train-test splits by the authors. For our study, we made appropriate splits and their distribution is presented on Figure C.52.

Detailed results for all pre-trained models are shown on Table C.56 and for all the models learned from scratch are presented on Table C.57. The best performing model is the pre-trained Vision Transformer model. The results on a class level are show on Table C.58 along with a confusion matrix on Figure C.53.

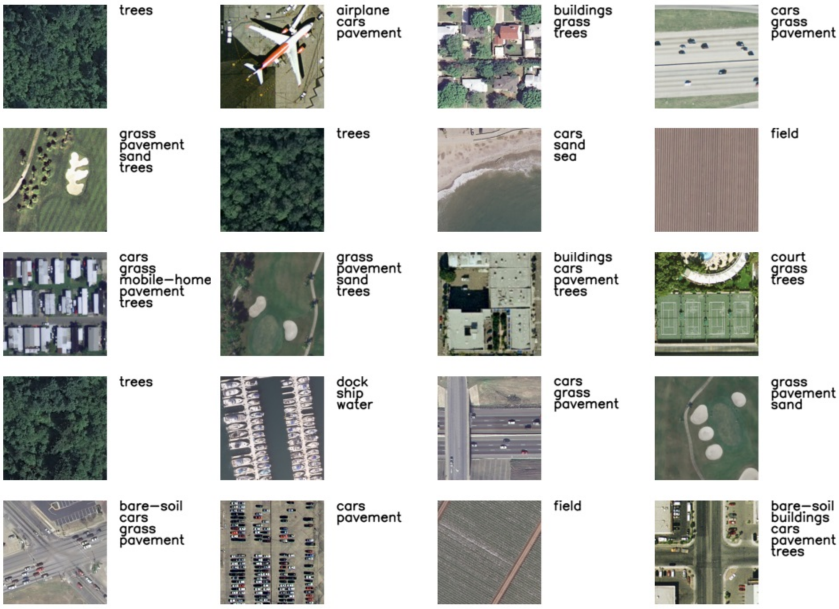
trees
airplane cars pavement
buildings grass trees
cars grass pavement
grass pavement sand trees
trees
cars sand sea
field
cars grass mobile−home pavement trees
grass pavement sand trees
buildings cars pavement trees
court grass trees
trees
dock ship water
cars grass pavement
grass pavement sand
bare−soil cars grass pavement
cars pavement
field
bare−soil buildings cars pavement trees

Figure C.51: Example images with labels from the UC Merced multi-label dataset.

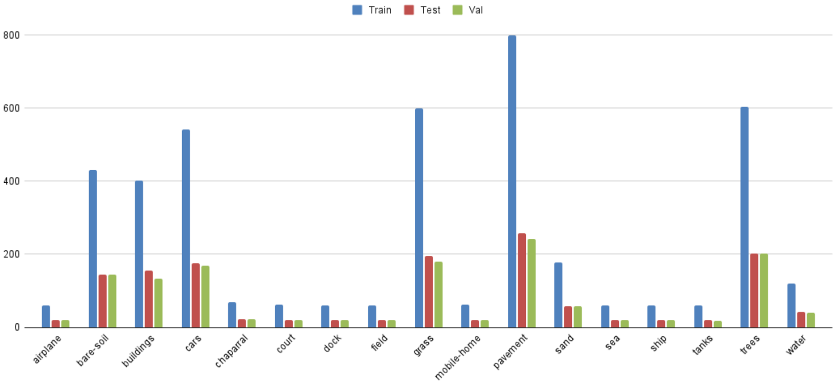

Figure C.52: Label distribution for the UC Merced multi-label dataset.

Table C.56: Detailed results for pre-trained models on the UC Merced multi-label dataset.

	mAP	Micro Precision	Macro Precision	Weighted Precision	Micro Recall	Macro Recall	Weighted Recall	Micro F1 score	Macro F1 score	Weighted F1 score	Avg. time / epoch (sec.)	Total time (sec.)	Best epoch
AlexNet	92.64	82.78	88.47	83.14	86.23	86.07	86.23	84.47	86.91	84.52	1.31	71	44
VGG16	92.85	86.43	91.38	86.61	86.37	87.84	86.37	86.40	89.33	86.39	3.30	132	30
ResNet50	95.66	86.19	92.37	86.53	87.71	88.84	87.71	86.94	90.23	86.95	2.76	124	35
ResNet152	96.01	88.10	93.19	88.33	86.23	89.45	86.23	87.15	91.07	87.13	5.04	227	35
DenseNet161	96.06	88.82	93.99	88.90	87.01	89.69	87.01	87.91	91.51	87.76	5.64	468	73
EfficientNetB0	95.38	87.98	93.22	88.23	87.36	89.19	87.36	87.67	90.92	87.65	2.54	254	98
ConvNeXt	96.43	88.80	94.30	88.91	87.92	89.92	87.92	88.36	91.84	88.32	3.92	259	56
Vision Transformer	**96.70**	88.87	94.16	89.09	89.62	90.55	89.62	89.24	92.14	89.16	4.13	132	22
MLP Mixer	96.34	88.62	94.38	88.75	87.99	88.16	87.99	88.31	90.77	88.21	3.25	182	46

Table C.57: Detailed results for models trained from scratch on the UC Merced multi-label dataset.

	mAP	Micro Precision	Macro Precision	Weighted Precision	Micro Recall	Macro Recall	Weighted Recall	Micro F1 score	Macro F1 score	Weighted F1 score	Avg. time / epoch (sec.)	Total time (sec.)	Best epoch
AlexNet	75.52	72.54	67.64	70.50	73.87	63.95	73.87	73.20	64.95	71.73	1.03	103	91
VGG16	76.80	74.33	72.59	73.65	78.53	70.75	78.53	76.37	71.14	75.77	3.24	324	99
ResNet50	79.87	76.72	77.52	76.42	78.67	71.21	78.67	77.68	72.73	76.99	2.76	276	99
ResNet152	73.66	76.89	69.85	74.78	73.80	65.05	73.80	75.32	66.81	73.92	5.06	506	86
DenseNet161	85.41	81.30	84.62	81.61	79.52	76.19	79.52	80.40	79.63	80.26	5.60	487	72
EfficientNetB0	79.87	78.45	74.10	76.91	75.85	72.13	75.85	77.13	72.89	76.25	2.23	252	99
ConvNeXt	72.27	72.40	69.27	71.19	74.65	62.31	74.65	73.50	63.50	71.89	3.81	381	100
Vision Transformer	**87.14**	81.02	85.66	81.10	79.31	75.95	79.31	80.16	79.29	79.69	4.12	412	95
MLP Mixer	75.68	75.29	73.64	74.60	73.38	64.54	73.38	74.32	67.44	73.43	3.11	311	99

Table C.58: Per label results for the pre-trained Vision Transformer model on the UC Merced multi-label dataset.

airplane	100.00	95.00	97.44
bare-soil	86.29	74.31	79.85
buildings	89.61	89.03	89.32
cars	87.36	86.86	87.11
chaparral	100.00	95.65	97.78
court	100.00	76.19	86.49
dock	100.00	100.00	100.00
field	100.00	85.71	92.31
grass	87.96	85.71	86.82
mobile-home	90.00	90.00	90.00
pavement	83.39	97.29	89.80
sand	91.38	91.38	91.38
sea	100.00	100.00	100.00
ship	100.00	95.24	97.56
tanks	100.00	90.00	94.74
trees	89.62	94.06	91.79
water	95.12	92.86	93.98

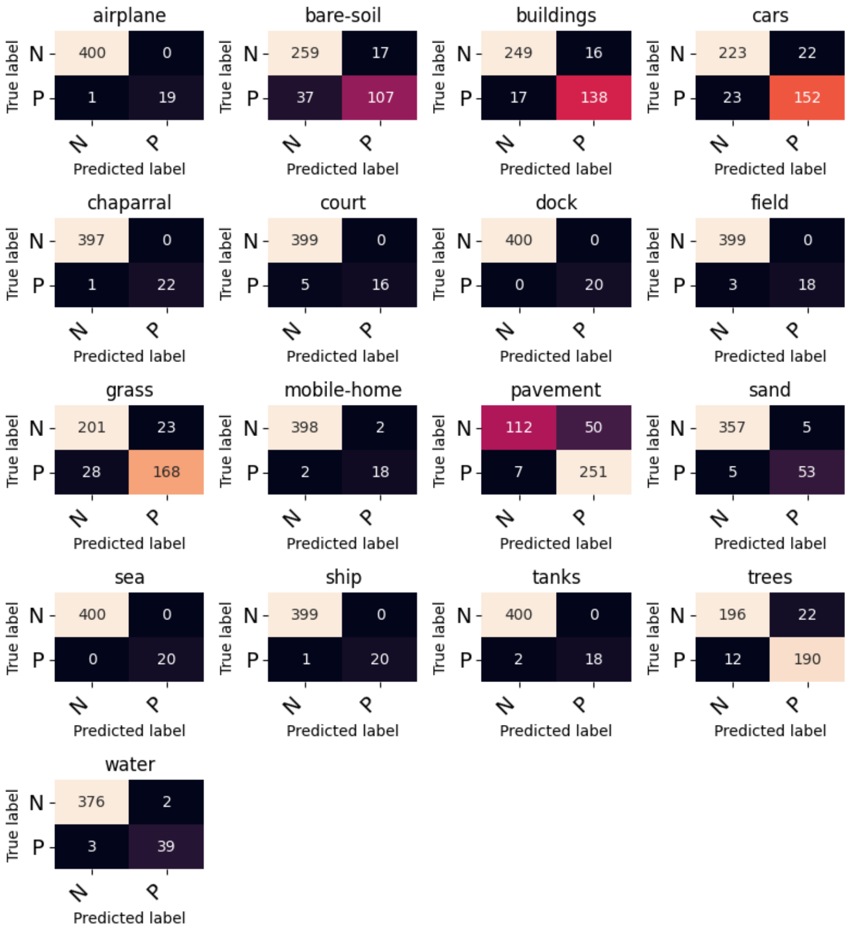

Figure C.53: Confusion matrix for the pre-trained Vision Transformer model on the UC Merced multi-label dataset.

C.17 BigEarthNet

BigEarthNet is a new large-scale multi-label Sentinel-2 benchmark archive [58] [36] . The BigEarthNet consists of 590326 Sentinel-2 image patches, each of which is a section of: 120x120 pixels for 10m bands; 60x60 pixels for 20m bands; and 20x20 pixels for 60m bands. Each image patch is annotated by multiple land-cover classes (i.e., multi-labels) that are provided from the CORINE Land Cover database. It was constructed by selecting 125 Sentinel-2 tiles acquired between June 2017 and May 2018. Covering different countries and seasonal period. More precisely, the number of images acquired in autumn, winter, spring and summer seasons are 154943, 117156, 189276 and 128951 respectively. The image patches are geographically distributed across 10 countries (Austria, Belgium, Finland, Ireland, Kosovo, Lithuania, Luxembourg, Portugal, Serbia, Switzerland) of Europe. The images are stored in tiff format and accompanied with additional metadata in JSON format.

The authors provide a predefined set of train-validation-test splits. Additionally, they proposed 2 versions of the labels in the dataset.

The first version of the dataset contains 43 labels with an 3.0 labels per image (Figure C.55). The labels in this version are: Continuous urban fabric, Discontinuous urban fabric, Industrial or commercial units, Road and rail networks and associated land, Port areas, Airports, Mineral extraction sites, Dump sites, Construction sites, Green urban areas, Sport and leisure facilities, Non-irrigated arable land, Permanently irrigated land, Rice fields, Vineyards, Fruit trees and berry plantations, Olive groves, Pastures, Annual crops associated with permanent crops, Complex cultivation patterns, Land principally occupied by agriculture, with significant areas of natural vegetation, Agro-forestry areas, Broad-leaved forest, Coniferous forest, Mixed forest, Natural grassland, Moors and heathland, Sclerophyllous vegetation, Transitional woodland/shrub, Beaches, dunes, sands, Bare rock, Sparsely vegetated areas, Burnt areas, Inland marshes, Peatbogs, Salt marshes, Salines, Intertidal flats, Water courses, Water bodies, Coastal lagoons, Estuaries, Sea and ocean. The largest class (label), Mixed forest, appeared in 217119 image, whereas the label with fewest appearances, Burnt areas, appeared in 328 images. This high imbalance should make the dataset more challenging.

Detailed results for all pre-trained models are shown on Table C.59 and for all the models learned from scratch are presented on Table C.60. The best performing model is the pre-trained ResNet50 model. The results on a class level are show on Table C.61 along with a confusion matrix on Figure C.56.

The second version of the dataset contains 19 labels with 2.9 labels per image on average (Figure C.57). The labels contained here are: Urban fabric, Industrial or commercial units, Arable land, Permanent crops, Pastures, Complex cultivation patterns, Land principally occupied by agriculture, with significant areas of natural vegetation, Agro-forestry areas, Broad-leaved forest, Coniferous forest, Mixed forest, Natural grassland and sparsely vegetated areas, Moors, heath-land and sclerophyllous vegetation, Transitional woodland, shrub, Beaches, dunes, sands, Inland wetlands, Coastal wetlands, Inland waters, Marine waters. The label Mixed forest is most commonly found and is present in 176546 images, whereas Beaches, dunes, sands appears in 1536 images and is the least frequently used label. Sample images are shown on Figure C.54.

Detailed results for all pre-trained models are shown on Table C.62 and for all the models learned from scratch are presented on Table C.63. The best performing model is the pre-trained EfficientNetB0 model. The results on a class level are show on Table C.64 along with a confusion matrix on Figure C.58.

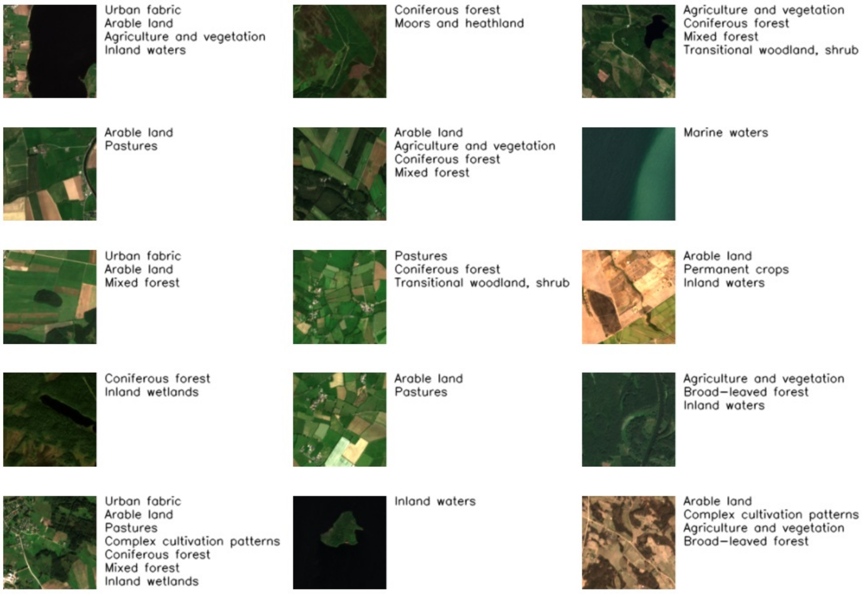

Figure C.54: Example images with labels from the BigEarthNet dataset.

C.17.1 BigEarthNet 43

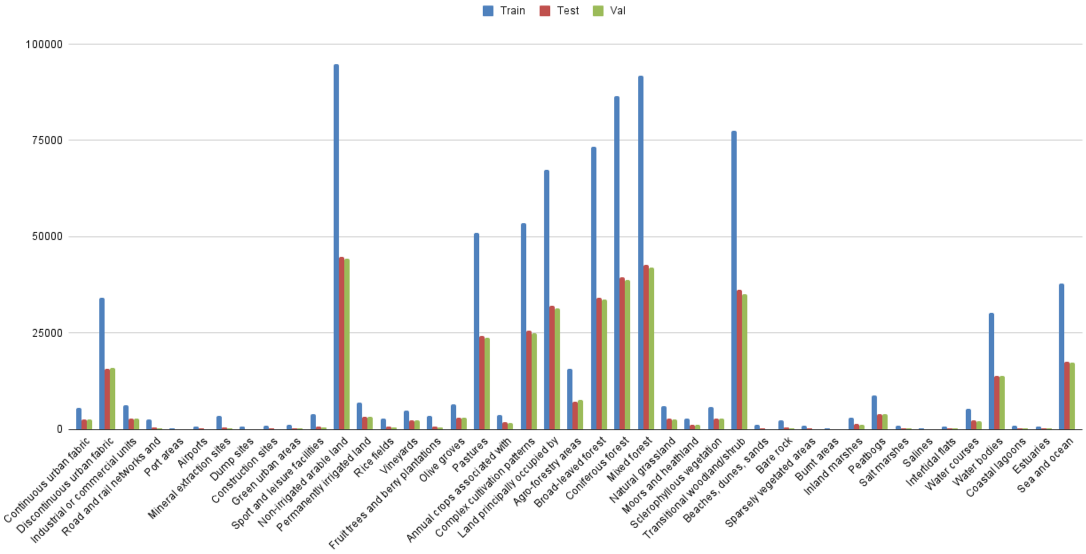

Figure C.55: Label distribution for the BigEarthNet 43 dataset.

Table C.59: Detailed results for pre-trained models on the BigEarthNet 43 dataset.

	mAP	Micro Precision	Macro Precision	Weighted Precision	Micro Recall	Macro Recall	Weighted Recall	Micro F1 score	Macro F1 score	Weighted F1 score	Avg. time / epoch (sec.)	Total time (sec.)	Best epoch
AlexNet	58.55	80.15	61.88	79.67	72.14	51.99	72.14	75.93	55.62	75.48	89.85	7188	70
VGG16	61.21	80.71	64.71	80.29	72.74	53.97	72.74	76.52	57.74	76.08	542.30	12473	13
ResNet50	**66.26**	81.99	67.47	81.64	74.14	58.15	74.14	77.87	61.87	77.54	414.18	9112	12
ResNet152	64.07	82.17	70.42	81.73	72.08	52.11	72.08	76.80	58.27	76.17	881.69	14107	6
DenseNet161	64.23	81.87	68.31	81.39	72.63	53.58	72.63	76.97	58.80	76.48	969.67	14545	5
EfficientNetB0	64.59	82.14	70.17	81.75	73.37	53.93	73.37	77.51	59.71	77.08	365.40	7308	10
ConvNeXt	66.17	81.67	69.24	81.31	73.93	56.11	73.93	77.61	61.12	77.23	642.81	10285	6
Vision Transformer	59.00	79.77	65.42	79.39	71.39	48.98	71.39	75.35	54.65	74.81	702.00	14742	11
MLP Mixer	59.65	81.18	67.47	80.55	71.30	48.85	71.30	75.92	54.95	75.28	492.84	12321	15

Table C.60: Detailed results for models trained from scratch on the BigEarthNet 43 dataset.

	mAP	Micro Precision	Macro Precision	Weighted Precision	Micro Recall	Macro Recall	Weighted Recall	Micro F1 score	Macro F1 score	Weighted F1 score	Avg. time / epoch (sec.)	Total time (sec.)	Best epoch
AlexNet	56.08	79.15	58.19	78.68	71.41	50.79	71.41	75.08	53.54	74.65	84.18	5051	45
VGG16	58.97	80.56	64.94	80.13	71.99	48.02	71.99	76.03	53.38	75.49	544.28	15784	14
ResNet50	**64.34**	82.07	67.06	81.65	73.47	55.64	73.47	77.53	60.14	77.12	409.87	18854	31
ResNet152	62.74	80.72	66.55	80.30	72.96	53.88	72.96	76.64	58.59	76.12	878.00	32486	22
DenseNet161	63.39	82.20	66.27	81.74	71.83	53.84	71.83	76.67	58.40	76.00	982.63	29479	15
EfficientNetB0	62.17	81.25	66.61	80.90	73.01	52.02	73.01	76.91	56.94	76.48	364.13	11288	16
ConvNeXt	60.47	80.71	67.02	80.19	72.40	51.09	72.40	76.33	56.51	75.81	645.51	26466	26
Vision Transformer	57.41	79.12	63.50	78.74	71.20	47.96	71.20	74.95	52.94	74.31	709.86	20586	14
MLP Mixer	58.77	80.82	65.97	80.10	71.12	48.10	71.12	75.66	53.38	74.90	500.77	15524	16

Table C.61: Per label results for the pre-trained ResNet50 model on the BigEarthNet 43 dataset.

Continuous urban fabric	86.22	80.76	83.40
Discontinuous urban fabric	82.80	68.65	75.06
Industrial or commercial units	71.73	43.73	54.34
Road and rail networks and associated land	45.51	45.69	45.60
Port areas	55.17	40.00	46.38
Airports	57.89	40.15	47.41
Mineral extraction sites	40.54	47.07	43.56
Dump sites	40.00	26.51	31.88
Construction sites	51.55	31.45	39.06
Green urban areas	46.18	39.66	42.67
Sport and leisure facilities	43.18	41.39	42.27
Non-irrigated arable land	87.42	83.84	85.59
Permanently irrigated land	78.29	55.81	65.17
Rice fields	58.83	64.98	61.75
Vineyards	68.28	50.71	58.20
Fruit trees and berry plantations	45.71	56.13	50.38
Olive groves	69.20	53.50	60.35
Pastures	82.21	71.58	76.52
Annual crops associated with permanent crops	61.07	35.87	45.20
Complex cultivation patterns	75.10	68.25	71.51
Land principally occupied by agriculture, with significant areas of natural vegetation	74.00	62.83	67.96
Agro-forestry areas	80.92	80.28	80.60
Broad-leaved forest	82.73	73.50	77.85
Coniferous forest	87.69	86.35	87.01
Mixed forest	83.26	81.99	82.62
Natural grassland	74.31	44.00	55.27
Moors and heathland	64.08	46.18	53.68
Sclerophyllous vegetation	76.07	68.70	72.20
Transitional woodland/shrub	73.78	62.74	67.81
Beaches, dunes, sands	57.50	62.44	59.87
Bare rock	54.67	73.87	62.84
Sparsely vegetated areas	45.95	41.21	43.45
Burnt areas	10.00	2.78	4.35
Inland marshes	64.39	30.62	41.50
Peatbogs	79.99	60.93	69.17
Salt marshes	61.67	54.05	57.61
Salines	73.12	64.76	68.69
Intertidal flats	61.76	62.87	62.31
Water courses	84.35	67.79	75.17
Water bodies	90.36	77.90	83.67
Coastal lagoons	91.23	80.98	85.80
Estuaries	83.25	69.32	75.65
Sea and ocean	99.39	98.53	98.96

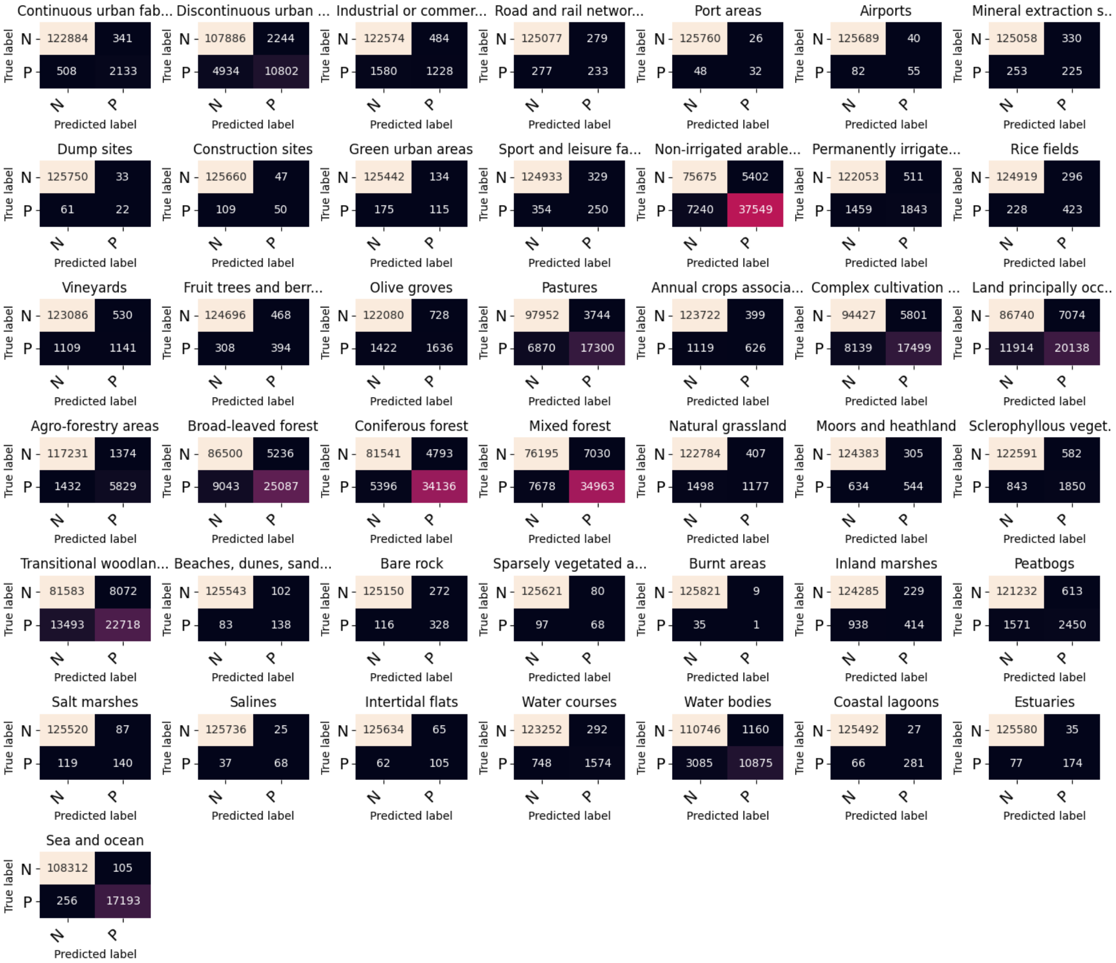

Figure C.56: Confusion matrix for the pre-trained ResNet50 model on the BigEarthNet 43 dataset.

C.17.2 BigEarthNet 19

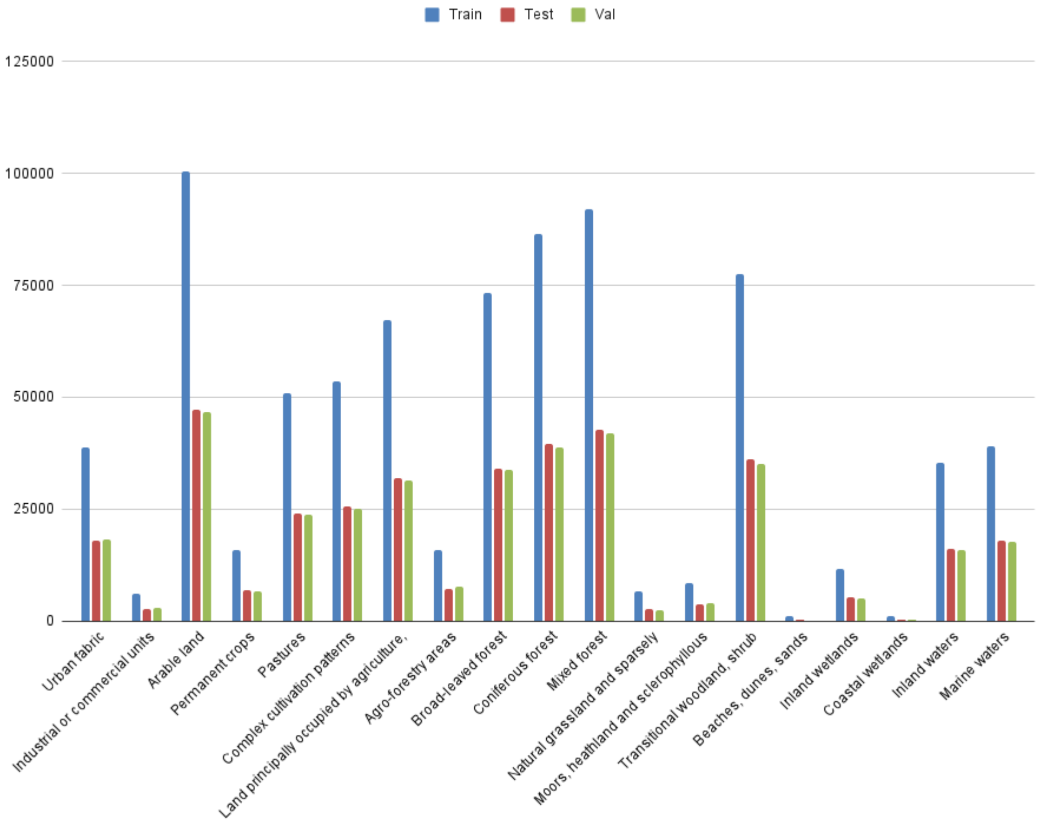

Figure C.57: Label distribution for the BigEarthNet 19 dataset.

Table C.62: Detailed results for pre-trained models on the BigEarthNet 19 dataset.

	mAP	Micro Precision	Macro Precision	Weighted Precision	Micro Recall	Macro Recall	Weighted Recall	Micro F1 score	Macro F1 score	Weighted F1 score	Avg. time / epoch (sec.)	Total time (sec.)	Best epoch
AlexNet	77.15	80.90	75.60	80.58	73.59	66.06	73.59	77.07	70.04	76.77	90.43	5245	48
VGG16	78.42	81.33	77.61	81.02	73.92	66.27	73.92	77.45	70.92	77.11	537.90	10758	10
ResNet50	79.98	82.65	78.57	82.37	73.62	67.74	73.62	77.88	72.12	77.51	413.24	7025	7
ResNet152	79.78	82.58	80.36	82.43	73.95	66.57	73.95	78.03	71.79	77.57	874.56	13993	6
DenseNet161	79.69	81.92	78.55	81.83	74.42	66.99	74.42	77.99	71.61	77.72	976.93	14654	5
EfficientNetB0	**80.22**	82.87	80.56	82.61	74.36	66.32	74.36	78.38	72.14	78.09	366.35	6228	7
ConvNeXt	77.15	80.90	75.60	80.58	73.59	66.06	73.59	77.07	70.04	76.77	631.67	9475	5
Vision Transformer	77.31	82.31	76.93	81.85	70.99	64.08	70.99	76.23	69.18	75.70	698.50	15367	12
MLP Mixer	77.29	81.41	78.12	80.97	73.20	64.33	73.20	77.09	69.68	76.62	488.68	12217	15

Table C.63: Detailed results for models trained from scratch on the BigEarthNet 19 dataset.

	mAP	Micro Precision	Macro Precision	Weighted Precision	Micro Recall	Macro Recall	Weighted Recall	Micro F1 score	Macro F1 score	Weighted F1 score	Avg. time / epoch (sec.)	Total time (sec.)	Best epoch
AlexNet	75.71	80.27	74.63	79.88	72.73	64.83	72.73	76.31	68.89	75.96	86.78	5120	44
VGG16	77.99	80.45	75.61	80.21	74.91	67.63	74.91	77.58	70.90	77.28	542.24	18436	19
ResNet50	78.73	82.94	78.20	82.44	72.61	66.15	72.61	77.44	71.28	76.99	413.89	26489	49
ResNet152	78.52	81.06	75.86	81.02	74.69	68.18	74.69	77.74	71.34	77.55	875.20	43760	35
DenseNet161	**79.73**	82.24	77.81	82.05	74.77	67.99	74.77	78.33	71.98	78.08	975.34	31211	17
EfficientNetB0	79.21	82.25	78.89	82.02	74.68	66.53	74.68	78.28	71.65	78.01	359.16	11493	17
ConvNeXt	77.91	81.39	78.16	81.18	73.57	64.64	73.57	77.29	70.08	76.95	643.66	24459	23
Vision Transformer	75.87	80.48	75.45	80.14	71.36	63.85	71.36	75.65	68.59	75.23	702.53	21076	15
MLP Mixer	77.01	81.39	77.37	81.12	72.59	64.34	72.59	76.74	69.74	76.42	495.88	15868	17

Table C.64: Per label results for the pre-trained EfficientNetB0 model on the BigEarthNet 19 dataset.

Urban fabric	83.86	72.64	77.85
Industrial or commercial units	74.70	39.85	51.97
Arable land	89.67	81.51	85.40
Permanent crops	81.17	53.17	64.25
Pastures	80.76	73.12	76.75
Complex cultivation patterns	75.31	67.58	71.23
Land principally occupied by agriculture, with significant areas of natural vegetation	73.83	61.14	66.89
Agro-forestry areas	84.68	75.80	79.99
Broad-leaved forest	81.81	74.04	77.73
Coniferous forest	88.37	84.93	86.61
Mixed forest	82.57	82.32	82.45
Natural grassland and sparsely vegetated areas	74.06	43.05	54.45
Moors, heathland and sclerophyllous vegetation	72.49	64.73	68.39
Transitional woodland, shrub	72.49	63.35	67.61
Beaches, dunes, sands	64.09	52.49	57.71
Inland wetlands	80.46	51.43	62.75
Coastal wetlands	81.07	44.19	57.20
Inland waters	90.33	76.76	83.00
Marine waters	99.01	97.96	98.48

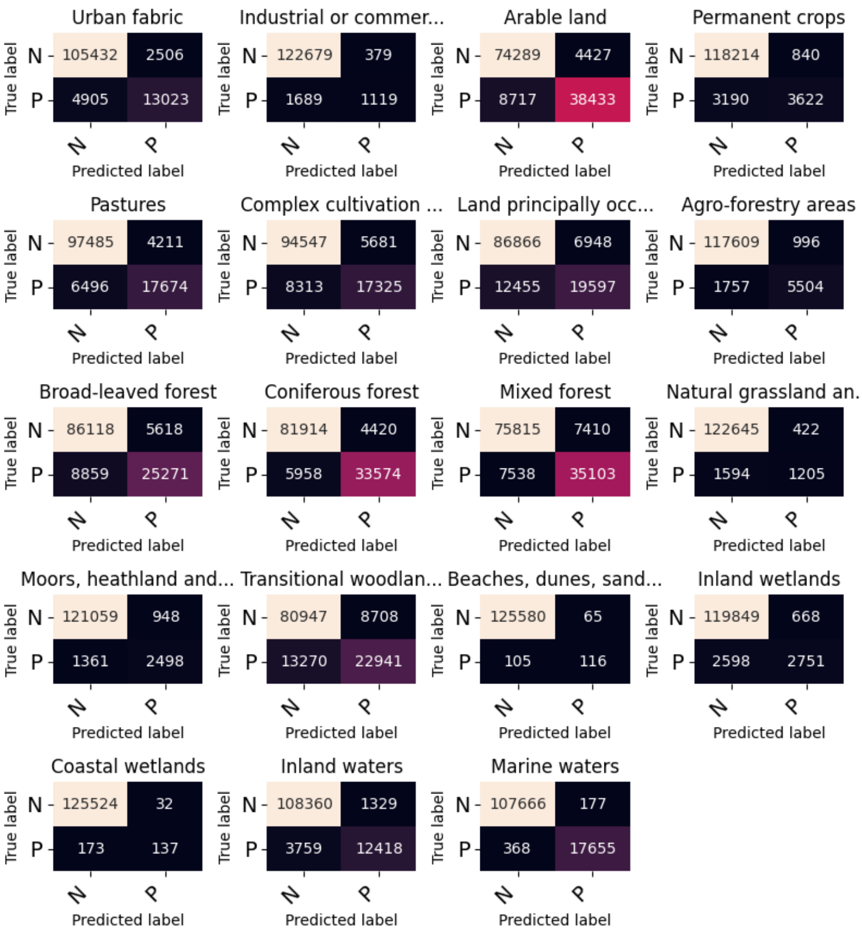

Figure C.58: Confusion matrix for the pre-trained EfficientNetB0 model on the BigEarthNet 19 dataset.

C.18 MLRSNet

MLRSNet [56] is a multi-label high spatial resolution remote sensing dataset for semantic scene understanding. It is composed of high-resolution optical satellite or aerial RGB images. MLRSNet contains a total of 109161 images (Figure C.59) within 46 scene categories, and each image has at least one of 60 predefined labels. The number of labels associated with each image varies between 1 and 13, but averages at 5.0 labels per image (Figure C.60). The labels annotating the images are: airplane, airport, bare soil, baseball diamond, basketball court, beach, bridge, buildings, cars, cloud, containers, crosswalk, dense residential area, desert, dock, factory, field, football field, forest, freeway, golf course, grass, greenhouse, gully, habor, intersection, island, lake, mobile home, mountain, overpass, park, parking lot, parkway, pavement, railway, railway station, river, road, roundabout, runway, sand, sea, ships, snow, snowberg, sparse residential area, stadium, swimming pool, tanks, tennis court, terrace, track, trail, transmission tower, trees, water, chaparral, wetland, wind turbine. The dataset does not have predefined train-tests splits.

Detailed results for all pre-trained models are shown on Table C.65 and for all the models learned from scratch are presented on Table C.66. The best performing model is the pre-trained ResNet152 model. The results on a class level are show on Table C.67 along with a confusion matrix on Figure C.61.

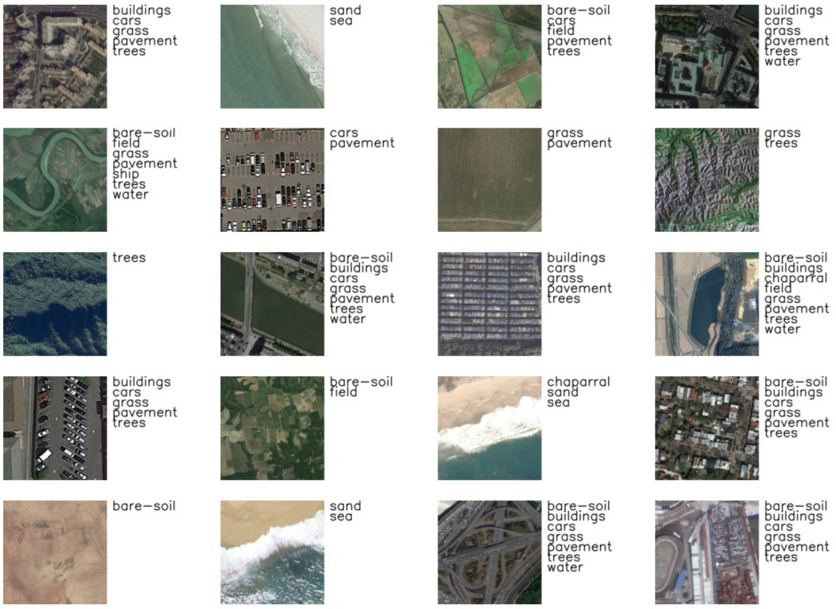

Figure C.59: Example images with labels from the MLRSNet dataset.

Table C.65: Detailed results for pre-trained models on the MLRSNet dataset.

	mAP	Micro Precision	Macro Precision	Weighted Precision	Micro Recall	Macro Recall	Weighted Recall	Micro F1 score	Macro F1 score	Weighted F1 score	Avg. time / epoch (sec.)	Total time (sec.)	Best epoch
AlexNet	93.40	87.93	87.37	88.15	88.54	88.95	88.54	88.24	87.73	88.25	34.09	1125	23
VGG16	94.63	89.56	89.05	89.73	89.39	90.06	89.39	89.48	89.18	89.48	132.24	3306	15
ResNet50	96.27	91.33	92.54	91.38	90.72	91.79	90.72	91.03	92.00	91.00	101.67	1726	16
ResNet152	**96.43**	91.83	92.51	91.84	90.74	92.27	90.74	91.28	92.26	91.25	214.11	5781	17
DenseNet161	96.31	91.61	92.35	91.63	90.85	92.18	90.85	91.23	92.07	91.21	237.35	6171	16
EfficientNetB0	95.39	91.35	91.63	91.37	90.09	90.52	90.09	90.71	90.84	90.67	86.80	2604	20
ConvNeXt	95.81	91.04	90.71	91.12	90.60	91.90	90.60	90.82	91.10	90.81	155.65	3580	13
Vision Transformer	96.41	91.81	91.89	91.84	91.75	93.16	91.75	91.78	92.33	91.77	170.90	3589	11
MLP Mixer	95.05	90.77	91.21	90.83	89.14	89.23	89.14	89.95	89.86	89.88	121.38	1942	6

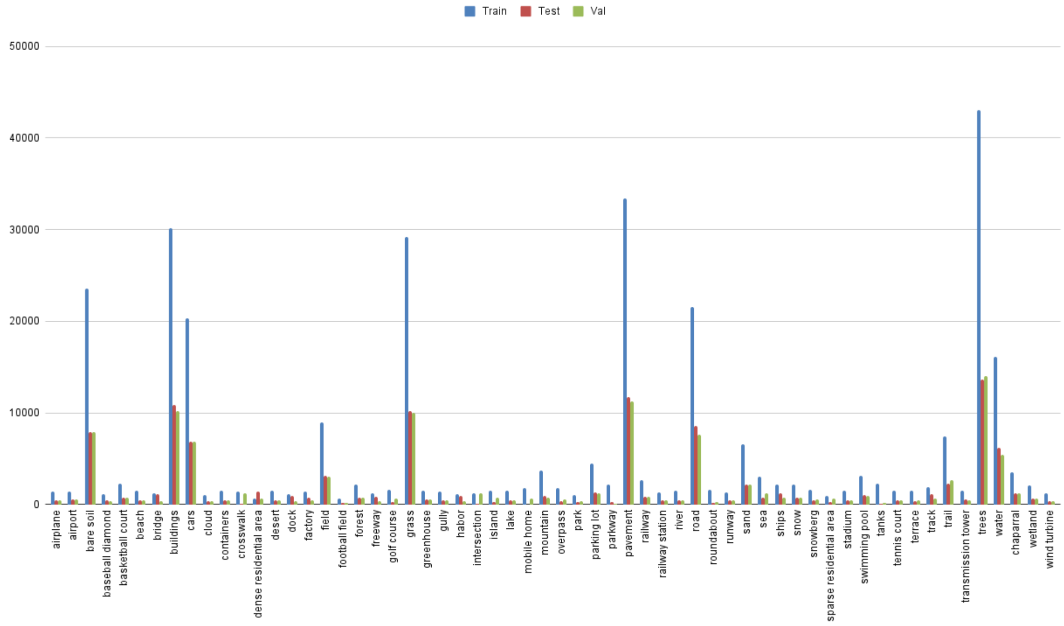

Figure C.60: Label distribution for the MLRSNet dataset.

Table C.66: Detailed results for models trained from scratch on the MLRSNet dataset.

	mAP	Micro Precision	Macro Precision	Weighted Precision	Micro Recall	Macro Recall	Weighted Recall	Micro F1 score	Macro F1 score	Weighted F1 score	Avg. time / epoch (sec.)	Total time (sec.)	Best epoch
AlexNet	90.85	86.53	83.69	86.69	86.58	86.54	86.58	86.56	84.70	86.58	34.92	2549	58
VGG16	91.52	86.63	83.24	87.00	87.98	88.23	87.98	87.30	85.33	87.41	132.22	7272	40
ResNet50	**95.26**	90.65	90.76	90.68	89.42	90.33	89.42	90.03	90.37	90.00	102.26	6238	46
ResNet152	93.98	89.47	88.92	89.54	88.45	88.55	88.45	88.96	88.51	88.92	214.47	14155	51
DenseNet161	94.74	90.23	89.59	90.23	88.13	88.86	88.13	89.17	88.87	89.08	237.96	11422	33
EfficientNetB0	94.40	89.90	89.09	89.99	89.22	90.19	89.22	89.56	89.40	89.54	89.34	8934	87
ConvNeXt	90.71	87.86	84.80	88.00	85.38	84.73	85.38	86.60	84.36	86.60	159.35	5896	22
Vision Transformer	87.25	85.78	82.28	85.81	84.64	80.90	84.64	85.20	81.06	85.03	170.71	5975	20
MLP Mixer	85.28	84.45	82.59	84.45	82.19	75.60	82.19	83.31	78.11	83.01	123.20	3080	10

Table C.67: Per label results for the pre-trained ResNet152 model on the MLRSNet dataset.

airplane	88.48	88.10	88.29
airport	86.95	79.73	83.18
bare soil	83.48	81.75	82.61
baseball diamond	98.99	99.39	99.19
basketball court	89.32	92.08	90.68
beach	99.40	99.20	99.30
bridge	95.92	92.99	94.43
buildings	93.97	89.90	91.89
cars	85.15	89.91	87.47
cloud	99.17	99.72	99.45
containers	99.80	99.80	99.80
crosswalk	82.61	73.08	77.55
dense residential area	99.70	95.90	97.76
desert	98.64	100.00	99.31
dock	99.02	98.27	98.64
factory	91.37	82.24	86.57
field	92.21	92.15	92.18
football field	67.03	85.12	75.00
forest	89.22	91.73	90.46
freeway	99.18	99.42	99.30
golf course	99.14	97.46	98.29
grass	88.68	86.83	87.75
greenhouse	98.85	99.04	98.94
gully	90.54	93.17	91.84
habor	99.02	98.27	98.64
intersection	75.81	94.00	83.93
island	99.60	98.82	99.21
lake	97.44	98.80	98.11
mobile home	64.29	87.10	73.97
mountain	97.99	95.37	96.66
overpass	94.10	93.52	93.81
park	90.70	91.05	90.87
parking lot	74.81	57.65	65.12
parkway	90.32	90.69	90.51
pavement	96.36	96.28	96.32
railway	90.69	94.09	92.36
railway station	88.32	83.07	85.61
river	98.80	99.20	99.00
road	91.85	91.41	91.63
roundabout	97.54	97.54	97.54
runway	99.24	86.95	92.69
sand	98.37	98.68	98.53
sea	99.06	98.80	98.93
ships	89.98	87.59	88.77
snow	96.39	89.90	93.03
snowberg	87.18	98.88	92.66
sparse residential area	98.26	96.58	97.41
stadium	92.37	95.74	94.02
swimming pool	93.53	79.49	85.94
tanks	95.10	100.00	97.49
tennis court	98.54	94.60	96.53
terrace	91.38	97.89	94.52
track	93.88	94.39	94.13
trail	79.91	78.92	79.41
transmission tower	99.42	98.65	99.03
trees	91.47	93.29	92.37
water	95.85	89.58	92.61
chaparral	96.53	94.24	95.37
wetland	89.87	88.29	89.07
wind turbine	99.76	99.76	99.76

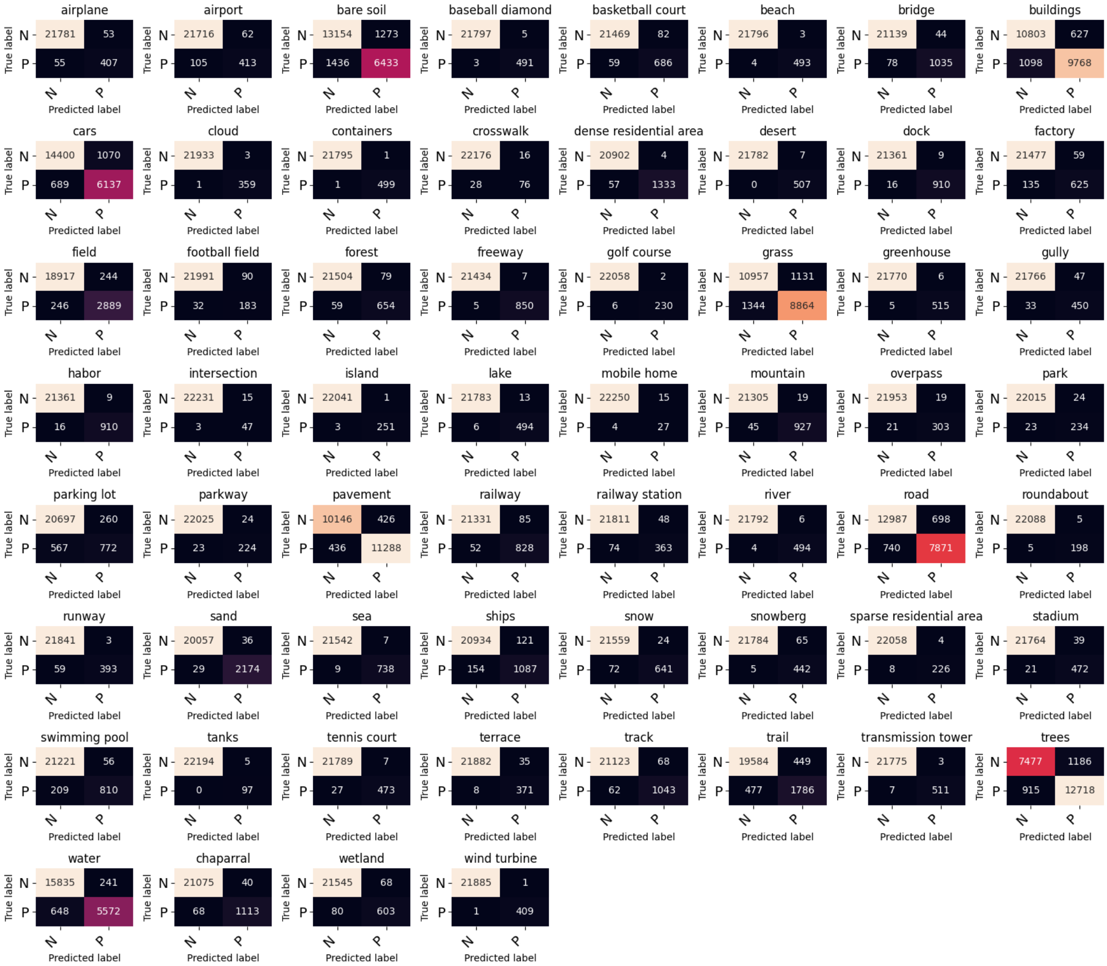

Figure C.61: Confusion matrix for the pre-trained ResNet152 model on the MLRSNet dataset.

C.19 DFC15

DFC15 [57] is a multi-label dataset created from the semantic segmentation dataset, DFC15 (IEEE GRSS data fusion contest, 2015), which was published and first used in 2015 IEEE GRSS Data Fusion Contest. The dataset is acquired over Zeebrugge with an airborne sensor, which is 300m off the ground. In total, 7 tiles are collected in DFC dataset, and each of them is pixels with a spatial resolution of 5cm. All tiles in DFC15 dataset are labeled in pixel-level, and each pixel is categorized into 8 distinct object classes: impervious, water, clutter, vegetation, building, tree, boat, and car. As a result of this process, the dataset contains 3342 images with a size of 600x600 pixels (Figure C.62). The images are annotated with one or more of the 8 labels in the dataset, with an average of 2.8 labels per image (Figure C.63). The most frequent labels is *impervious* and it appears in 3133 image. The label *tree* is least frequent and it appears in 258 images.

Detailed results for all pre-trained models are shown on Table C.68 and for all the models learned from scratch are presented on Table C.69. The best performing model is the pre-trained ConvNeXt model. The results on a class level are show on Table C.70 along with a confusion matrix on Figure C.64.

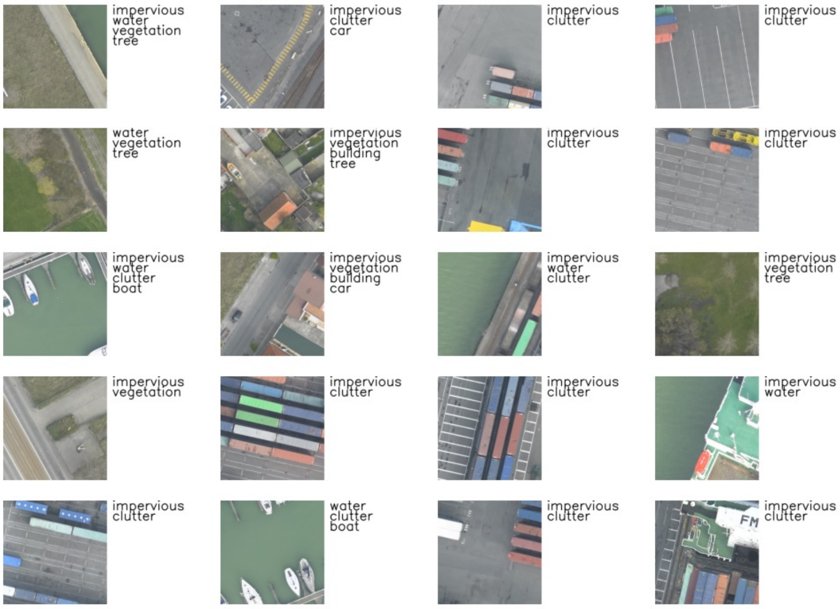

Figure C.62: Example images with labels from the DFC15 dataset.

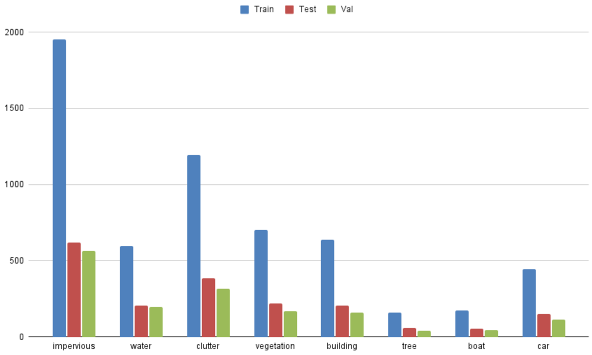

Figure C.63: Label distribution for the DFC15 dataset.

Table C.68: Detailed results for pre-trained models on the DFC15 dataset.

	mAP	Micro Precision	Macro Precision	Weighted Precision	Micro Recall	Macro Recall	Weighted Recall	Micro F1 score	Macro F1 score	Weighted F1 score	Avg. time / epoch (sec.)	Total time (sec.)	Best epoch
AlexNet	94.06	92.33	89.03	92.32	91.01	86.21	91.01	91.67	87.52	91.60	7.74	325	32
VGG16	96.57	94.09	91.75	94.30	92.60	88.57	92.60	93.34	89.79	93.30	8.94	286	22
ResNet50	97.66	95.21	94.19	95.19	93.50	91.54	93.50	94.35	92.81	94.31	8.49	331	29
ResNet152	97.60	95.08	93.78	95.04	93.97	90.88	93.97	94.52	92.25	94.46	9.45	444	37
DenseNet161	97.53	95.07	93.52	95.03	94.71	91.43	94.71	94.89	92.43	94.85	9.54	544	47
EfficientNetB0	96.79	95.54	94.09	95.51	94.08	90.97	94.08	94.81	92.48	94.77	8.33	583	60
ConvNeXt	**97.99**	94.99	93.84	94.98	94.24	91.39	94.24	94.61	92.55	94.58	8.72	471	44
Vision Transformer	97.62	96.40	94.75	96.33	93.34	89.45	93.34	94.84	91.96	94.77	8.76	219	15
MLP Mixer	97.94	95.23	94.29	95.20	93.92	90.82	93.92	94.57	92.48	94.53	8.18	229	18

Table C.69: Detailed results for models trained from scratch on the DFC15 dataset.

	mAP	Micro Precision	Macro Precision	Weighted Precision	Micro Recall	Macro Recall	Weighted Recall	Micro F1 score	Macro F1 score	Weighted F1 score	Avg. time / epoch (sec.)	Total time (sec.)	Best epoch
AlexNet	88.10	90.40	84.01	90.16	85.57	76.29	85.57	87.92	79.75	87.69	7.83	783	99
VGG16	89.87	91.07	86.30	91.03	87.37	79.82	87.37	89.18	82.38	88.98	8.50	799	79
ResNet50	94.67	92.88	89.33	92.84	91.75	87.01	91.75	92.32	88.11	92.26	8.92	464	37
ResNet152	94.19	92.05	89.36	91.91	89.96	83.80	89.96	90.99	86.36	90.82	9.66	647	52
DenseNet161	**95.85**	94.23	92.10	94.19	92.28	87.62	92.28	93.24	89.65	93.15	9.89	613	47
EfficientNetB0	93.97	93.90	91.67	93.77	91.91	85.64	91.91	92.90	88.40	92.75	8.47	686	66
ConvNeXt	89.56	91.08	87.12	90.85	87.47	79.56	87.47	89.24	82.99	89.03	8.80	880	91
Vision Transformer	94.16	92.45	89.36	92.34	89.96	84.84	89.96	91.19	87.00	91.10	8.85	743	69
MLP Mixer	91.66	90.43	86.00	90.27	88.90	82.91	88.90	89.66	84.40	89.56	8.31	831	100

Table C.70: Per label results for the pre-trained ConvNeXt model on the DFC15 dataset.

impervious	96.67	98.87	97.76
water	95.12	94.20	94.66
clutter	96.01	94.26	95.13
vegetation	93.27	94.98	94.12
building	92.89	89.71	91.27
tree	85.96	85.96	85.96
boat	97.92	87.04	92.16
car	92.86	86.09	89.35

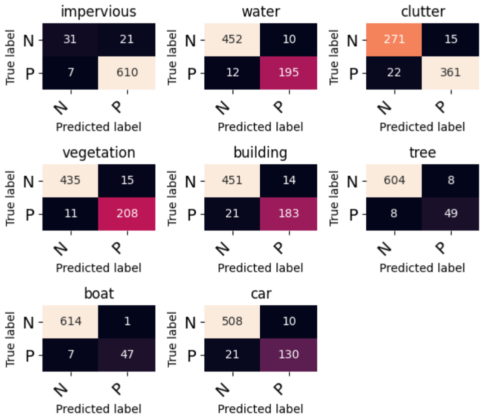

Figure C.64: Confusion matrix for the pre-trained ConvNeXt model on the DFC15 dataset.

C.20 Planet UAS

The Planet UAS dataset [60] was created by the company, Planet - designer and builder of the world's largest constellation of Earth-imaging satellites. The aim is to label satellite image chips with atmospheric conditions and various classes of land cover/land use. The dataset is available on Kaggle and is approximately 32 GB worth of data. The data contains 40479 satellite images organized in tiff and jpg files (Figure C.65). The jpg file show the natural light spectrum of the image, whereas the tiff files provide extra information about the infrared features of the satellite image, both with 256x256 pixels resolution. There are a total of 17 different labels with an average of 2.9 labels per image.

The imagery has a ground-sample distance (GSD) of 3.7m and an orthorectified pixel size of 3m. The data comes from Planet's Flock 2 satellites in both sun-synchronous and ISS orbits and was collected between January 1, 2016 and February 1, 2017. All of the scenes come from the Amazon basin which includes Brazil, Peru, Uruguay, Colombia, Venezuela, Guyana, Bolivia, and Ecuador. There are a total of 17 different labels. Out of those, 4 labels correspond to weather: Clear, Cloudy, Partly Cloudy, Haze. The rest of the (13) labels correspond to land: Habitation, Bare Ground, Cultivation, Agriculture, Blow Down, Conventional Mine, Selective Logging, Slash Burn, Artisanal Mine, Blooming, Primary, Water, and None.

The dataset only has the train set publicly available and we use that to generate train, test and validation splits (Figure C.66).

Detailed results for all pre-trained models are shown on Table C.71 and for all the models learned from scratch are presented on Table C.72. The best performing model is the pre-trained MLPMixer model. The results on a class level are show on Table C.73 along with a confusion matrix on Figure C.67.

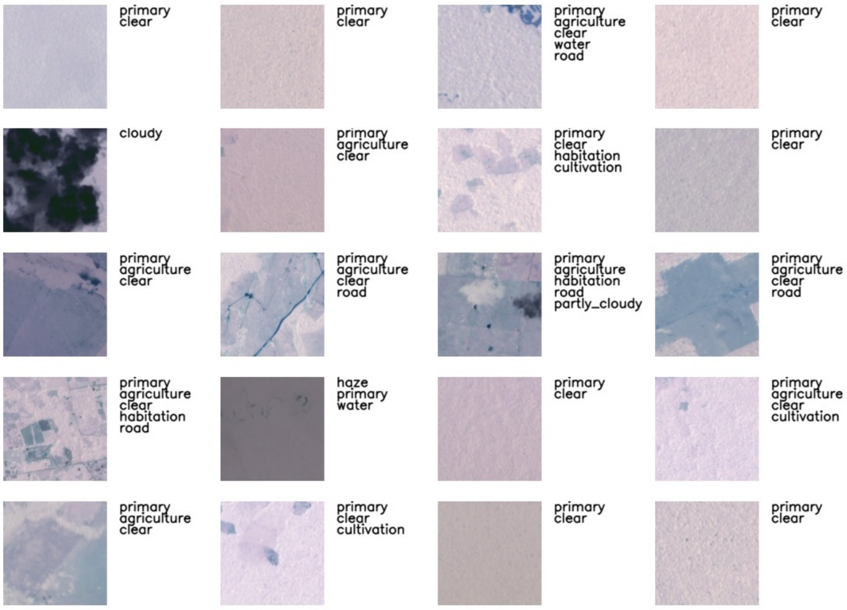
primary clear
primary clear
primary agriculture clear water road
primary clear
cloudy
primary agriculture clear
primary clear habitation cultivation
primary clear
primary agriculture clear
primary agriculture clear road
primary agriculture habitation road partly_cloudy
primary agriculture clear road
primary agriculture clear habitation road
haze primary water
primary clear
primary agriculture clear cultivation
primary agriculture clear
primary clear cultivation
primary clear
primary clear

Figure C.65: Example images with labels from the Planet UAS dataset.

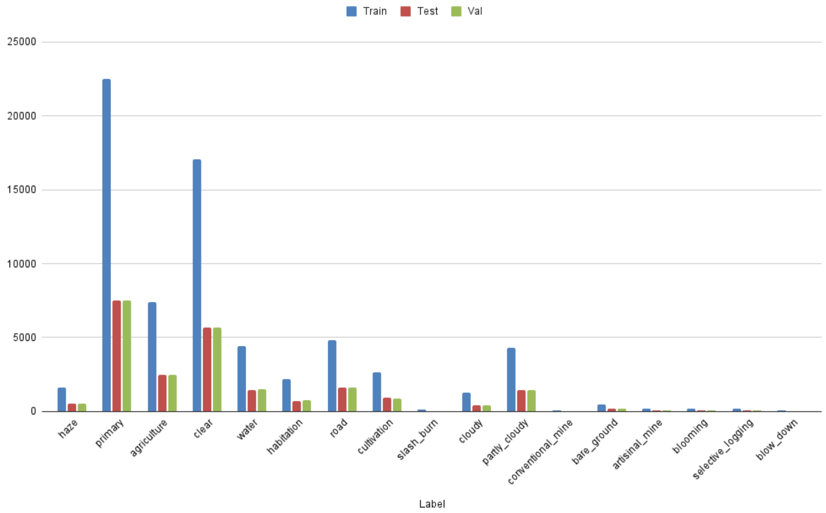

Figure C.66: Label distribution for the PlanetUAS dataset.

Table C.71: Detailed results for pre-trained models on the PlanetUAS dataset.

	mAP	Micro Precision	Macro Precision	Weighted Precision	Micro Recall	Macro Recall	Weighted Recall	Micro F1 score	Macro F1 score	Weighted F1 score	Avg. time / epoch (sec.)	Total time (sec.)	Best epoch
AlexNet	64.05	90.71	66.56	89.39	86.29	54.39	86.29	88.44	57.73	87.49	17.45	576	23
VGG16	65.58	92.09	64.14	90.90	86.88	55.99	86.88	89.41	59.19	88.58	50.38	1058	11
ResNet50	65.53	92.17	67.64	90.91	86.07	54.98	86.07	89.02	58.72	87.91	37.00	740	10
ResNet152	64.82	91.66	66.67	90.52	87.23	56.03	87.23	89.39	59.47	88.60	81.83	1964	14
DenseNet161	66.34	91.75	73.56	90.77	87.42	55.29	87.42	89.53	59.16	88.50	90.40	1808	10
EfficientNetB0	64.16	92.18	69.45	90.98	87.18	52.66	87.18	89.61	56.02	88.62	33.52	771	13
ConvNeXt	66.45	91.52	70.00	90.47	87.95	56.06	87.95	89.70	59.95	88.92	59.63	1431	14
Vision Transformer	66.80	91.31	69.63	90.18	87.79	56.11	87.79	89.52	59.95	88.56	65.71	920	4
MLP Mixer	**67.33**	92.18	74.70	91.30	86.68	56.56	86.68	89.35	60.79	88.59	45.94	735	6

Table C.72: Detailed results for models trained from scratch on the PlanetUAS dataset.

	mAP	Micro Precision	Macro Precision	Weighted Precision	Micro Recall	Macro Recall	Weighted Recall	Micro F1 score	Macro F1 score	Weighted F1 score	Avg. time / epoch (sec.)	Total time (sec.)	Best epoch
AlexNet	60.28	90.32	67.35	88.88	84.81	51.24	84.81	87.48	54.52	86.25	18.65	1865	87
VGG16	60.68	90.39	60.11	88.74	84.97	50.56	84.97	87.60	53.21	86.44	50.68	2889	42
ResNet50	64.19	92.16	67.02	90.84	86.52	54.31	86.52	89.25	58.47	88.24	37.57	2592	54
ResNet152	**64.96**	91.57	69.94	90.42	86.97	55.02	86.97	89.21	59.06	88.28	80.86	6792	69
DenseNet161	64.74	91.79	69.52	90.53	87.01	55.20	87.01	89.34	59.12	88.37	90.11	4866	39
EfficientNetB0	63.87	91.70	65.64	90.55	87.03	53.86	87.03	89.30	57.21	88.40	33.47	2711	66
ConvNeXt	61.28	90.92	64.25	89.39	84.29	51.55	84.29	87.48	54.68	86.19	59.35	5935	90
Vision Transformer	59.41	90.35	60.32	88.16	83.12	47.68	83.12	86.58	51.94	84.94	65.52	4128	48
MLP Mixer	58.55	89.67	62.22	87.58	82.21	48.88	82.21	85.78	51.46	84.06	45.93	2572	41

Table C.73: Per label results for the pre-trained MLPMixer model on the PlanetUAS dataset.

haze	71.67	71.80	71.73
primary	97.52	98.87	98.19
agriculture	88.07	76.54	81.90
clear	96.97	95.37	96.16
water	87.88	70.59	78.29
habitation	78.66	70.14	74.16
road	88.23	79.03	83.38
cultivation	67.71	44.97	54.04
slash_burn	0.00	0.00	0.00
cloudy	83.25	83.25	83.25
partly_cloudy	90.87	91.85	91.36
conventional_mine	75.00	52.17	61.54
bare_ground	45.95	27.57	34.46
artisinal_mine	86.00	65.15	74.14
blooming	100.00	1.56	3.08
selective_logging	45.45	22.73	30.30
blow_down	66.67	10.00	17.39

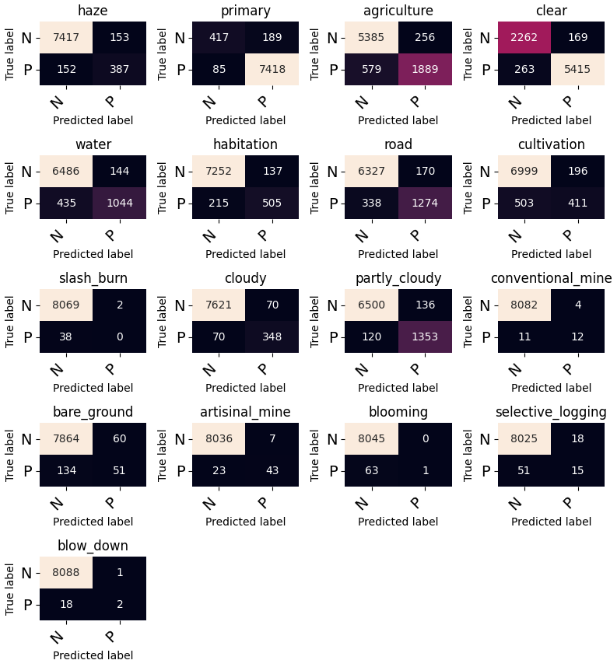

Figure C.67: Confusion matrix for the pre-trained MLPMixer model on the PlanetUAS dataset.

C.21 AID multi-label

Hua et al. [59] extend the AID dataset for multi-label classification. They manually relabeled some images in the AID dataset. With extensive human visual inspections, 3000 aerial images from 30 scenes in the AID dataset were selected and assigned with multiple object labels. The dataset has 17 labels with 5.2 labels per image on average. The labels are: bare soil, airplane, building, car, charparral, court, dock, field, grass, mobile home, pavement, sand, sea, ship, tank, tree and water. The authors provide a proposed train-test split. Figure C.68 show some example images from the AID multi-label dataset. The distribution of the labels for the train, validation and test splits is shown in Figure C.69 from which we can observe an imbalanced distribution, some of the labels are heavily populated with images/samples, and some of the labels are with only few images/samples (for example the label mobile-home has only one image in the respective train, validation and test splits).

Detailed results for all pre-trained models are shown on Table C.74 and for all the models learned from scratch are presented on Table C.75. The best performing model is the pre-trained ResNet152 model. The results on a class level are show on Table C.76 along with a confusion matrix on Figure C.70.

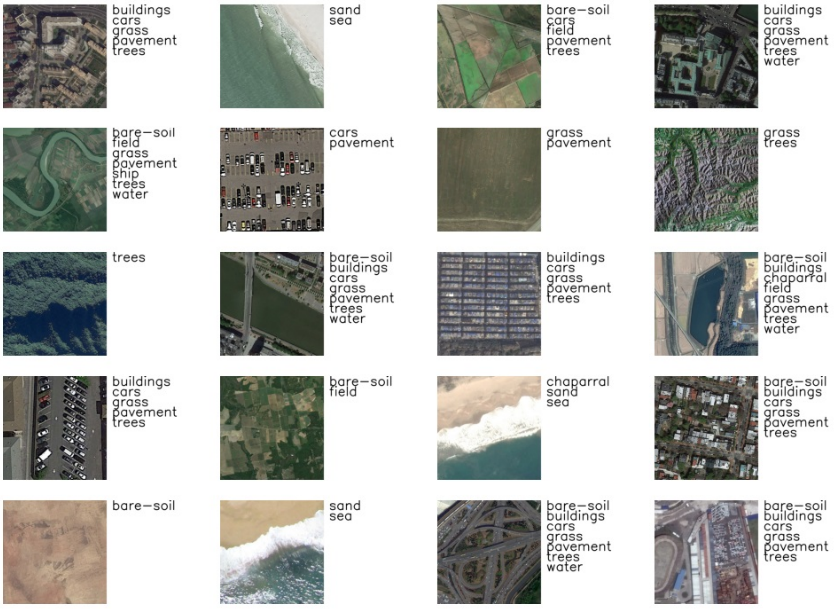
buildings cars grass pavement trees
sand sea
bare−soil cars field pavement trees
buildings cars grass pavement trees water
bare−soil field grass pavement ship trees water
cars pavement
grass pavement
grass trees
trees
bare−soil buildings cars grass pavement trees water
buildings cars grass pavement trees
bare−soil buildings chaparral field grass pavement trees water
buildings cars grass pavement trees
bare−soil field
chaparral sand sea
bare−soil buildings cars grass pavement trees
bare−soil
sand sea
bare−soil buildings cars grass pavement trees water
bare−soil buildings cars grass pavement trees

Figure C.68: Example images with labels from the AID multilabel dataset.

Table C.74: Detailed results for pre-trained models on AID multi-label

	mAP	Micro Precision	Macro Precision	Weighted Precision	Micro Recall	Macro Recall	Weighted Recall	Micro F1 score	Macro F1 score	Weighted F1 score	Avg. time / epoch (sec.)	Total time (sec.)	Best epoch
AlexNet	75.91	88.34	75.10	87.33	86.04	66.15	86.04	87.18	68.61	86.19	5.55	172	21
VGG16	79.89	90.12	76.29	88.58	87.62	67.13	87.62	88.85	70.03	87.74	6.33	190	20
ResNet50	80.76	91.36	79.13	89.72	87.68	68.37	87.68	89.48	72.34	88.34	5.94	190	22
ResNet152	80.94	91.92	80.10	90.46	86.62	64.52	86.62	89.19	69.53	87.98	7.97	239	20
DenseNet161	81.71	90.77	80.12	89.54	88.84	68.22	88.84	89.80	71.80	88.76	8.71	366	32
EfficientNetB0	78.00	91.38	78.79	89.79	86.81	64.22	86.81	89.04	69.40	87.76	6.15	381	52
ConvNeXt	**82.30**	92.23	86.10	92.06	88.07	68.96	88.07	90.10	73.01	89.17	6.63	345	42
Vision Transformer	81.54	93.33	81.54	91.76	87.10	67.84	87.10	90.11	73.15	88.96	6.95	146	11
MLP Mixer	80.88	93.09	85.44	92.78	86.88	64.11	86.88	89.87	69.48	88.53	6.35	165	16

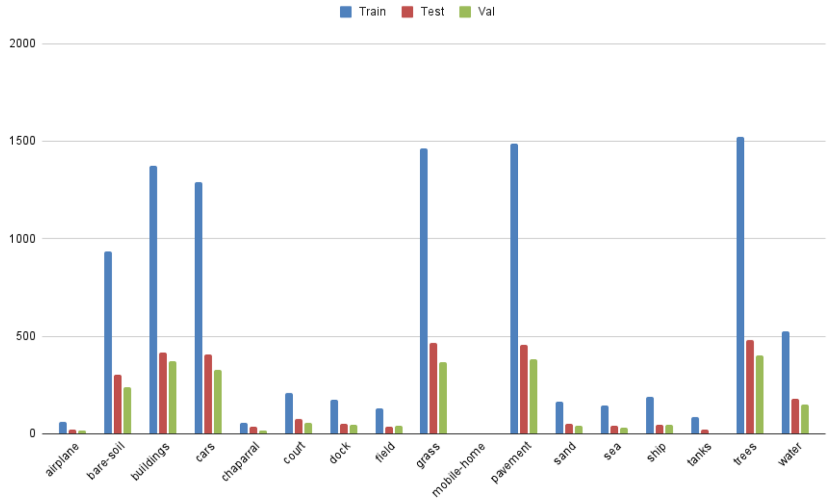

Figure C.69: Label distribution for the AID multilabel dataset.

Table C.75: Detailed results for models trained from scratch on the AID multi-label dataset.

	mAP	Micro Precision	Macro Precision	Weighted Precision	Micro Recall	Macro Recall	Weighted Recall	Micro F1 score	Macro F1 score	Weighted F1 score	Avg. time / epoch (sec.)	Total time (sec.)	Best epoch
AlexNet	68.78	86.93	69.98	85.45	84.33	60.45	84.33	85.61	63.48	84.42	5.82	524	75
VGG16	69.21	87.03	66.46	85.22	84.42	62.06	84.42	85.71	63.75	84.60	6.28	490	63
ResNet50	70.87	89.52	74.76	87.95	84.04	59.51	84.04	86.69	64.46	85.27	5.74	379	51
ResNet152	69.65	87.95	76.32	87.11	84.49	58.55	84.49	86.18	62.72	84.76	8.08	477	44
DenseNet161	71.22	88.57	76.27	87.52	85.23	60.19	85.23	86.87	64.09	85.33	8.47	449	38
EfficientNetB0	**72.89**	88.51	71.56	86.66	86.42	64.45	86.42	87.45	67.01	86.22	5.94	398	52
ConvNeXt	65.59	87.00	67.56	85.16	83.75	56.43	83.75	85.34	59.44	83.75	6.40	576	75
Vision Transformer	65.58	85.82	63.05	83.61	83.94	56.33	83.94	84.87	58.63	83.37	6.82	627	77
MLP Mixer	64.24	85.72	66.07	83.70	83.46	56.52	83.46	84.58	59.30	83.02	6.41	506	64

Table C.76: Per label results for the pre-trained ResNet152 model on the AID multi-label dataset.

airplane	100.00	25.00	40.00
bare-soil	77.30	77.30	77.30
buildings	93.72	96.64	95.16
cars	94.13	94.13	94.13
chaparral	100.00	2.70	5.26
court	80.43	49.33	61.16
dock	82.93	68.00	74.73
field	85.71	61.54	71.64
grass	95.30	95.71	95.50
mobile-home	0.00	0.00	0.00
pavement	97.82	97.82	97.82
sand	97.78	84.62	90.72
sea	100.00	90.91	95.24
ship	82.22	78.72	80.43
tanks	100.00	90.48	95.00
trees	95.42	94.82	95.12
water	80.99	64.61	71.88

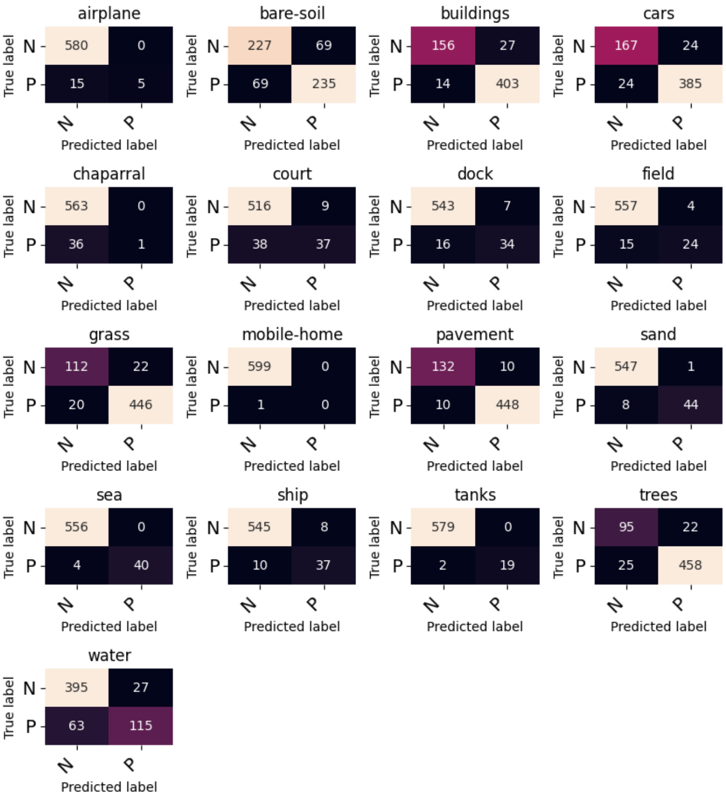

Figure C.70: Confusion matrix for the pre-trained ResNet152 model on the AID multi-label dataset.